

LEA FEODORA LENZ

STAR-PLANET INTERACTIONS:
EMISSION SPECTROSCOPY OF H_3^+ IN
EXTRASOLAR GIANT PLANET
ATMOSPHERES

DISSERTATION

Star-Planet Interactions: Emission Spectroscopy of H_3^+ in Extrasolar Giant Planet Atmospheres

Dissertation

zur Erlangung des mathematisch-naturwissenschaftlichen Doktorgrades

”Doctor rerum naturalium”

der Georg-August-Universität Göttingen

im Promotionsprogramm GAUSS

der Georg-August University School of Science (GAUSS)

vorgelegt von

Lea Feodora Lenz

aus

Lübeck

Göttingen, 2019

Betreuungsausschuss

Prof. Dr. Ansgar Reiners, Sonnenphysik und Stellare Astrophysik, Institut für Astrophysik

Prof. Dr. Stefan Dreizler, Sonnenphysik und Stellare Astrophysik, Institut für Astrophysik

Mitglieder der Prüfungskommission

Referent/in: Prof. Dr. Ansgar Reiners, Sonnenphysik und Stellare Astrophysik, Institut für Astrophysik

Korreferent/in: Prof. Dr. Stefan Dreizler, Sonnenphysik und Stellare Astrophysik, Institut für Astrophysik

Weitere Mitglieder der Prüfungskommission:

Prof. Dr. Wolfgang Glatzel, Theoretische und Numerische Astrophysik, Institut für Astrophysik

Prof. Dr. Wolfram Kollatschny, Extragalaktische Astrophysik und Kosmologie, Institut für Astrophysik

Dr. Miriam Rengel, Planeten und Kometen, Max-Planck-Institut für Sonnensystemforschung

Prof. Dr. Andras Tilgner, Geophysikalische Fluidodynamik, Institut für Geophysik

Tag der mündlichen Prüfung:

Abstract

Extrasolar giant planets (EGP) in a close-in orbit undergo extreme irradiation by their host star. Emission of H_3^+ is expected to support the stabilization of the planetary atmosphere, since the ion radiates in the near-infrared (NIR) and thereby cools the upper layers of the atmosphere.

The simulations of H_3^+ emission from hot Jupiter planets differ in their predicted strengths by several orders of magnitude. H_3^+ emissions from EGP atmospheres have not been detected yet. Previous to this study, only a few other attempts for the observation of H_3^+ from hot Jupiter atmospheres have been made and did not reach the emission limits of the theoretical predictions.

We obtained ground based spectroscopy with CRIRES at the Very Large Telescope (VLT) for the three hot Jupiter systems HD 209458, HD 217107 and GJ 86, and search for signatures of H_3^+ emission in the L' band. CRIRES is a NIR high resolution spectrograph and provides adequate resolution to observe atmospheric emission lines from exoplanet atmospheres.

For the transiting hot Jupiter HD 209458 b, we obtained spectra during and after secondary eclipse. We use the information on the ephemeris of the planet to search for H_3^+ emission lines directly in the spectra after correcting for the planetary radial velocity. We apply a cross-correlation approach, subtracting the stellar signal with the secondary eclipse spectra. We also apply a ‘shift-and-add’ technique, combining all non-eclipse spectra in order to detect possibly hidden H_3^+ emission. We do not find any signs of H_3^+ emission from the atmosphere of the hot Jupiter HD 209458 b in the obtained spectra. We derive the emission limits for the H_3^+ line at 3953.0 nm [$Q(1,0)$] to be $8.32 \cdot 10^{18}$ W and $5.34 \cdot 10^{18}$ W for the line at 3985.5 nm [$Q(3,0)$]. These emission limits are in good agreement to other ground based measurements of H_3^+ emission limits in hot Jupiter atmospheres. However, comparing our emission limits to the theoretical predictions, there is a deficiency of up to three magnitudes of sensitivity in order to measure H_3^+ emission in our data.

From our detection limits we derived the constraints for pushing the H_3^+ emission limit down to $5 \cdot 10^{16}$ W with new CRIRES observations and successfully obtained spectra of the two non-transiting systems HD 217107 and GJ 86. We searched for H_3^+ directly and also tested the cross-correlation approach, similar to the first attempt. The analysis of the spectra from both hot Jupiter systems did not reveal signatures of atmospheric H_3^+ emission. We derive our best result for HD 217107 b with an emission limit of $2.88 \cdot 10^{16}$ W for the emission line at 3985.5 nm. This limit is below the estimations by Miller et al. (2000) and in range of the limit derived by Yelle (2004). Future observational attempts of atmospheric H_3^+ of hot Jupiters with ground based instruments, aiming at even lower emission limits preferably would be carried out with high resolution spectroscopy at future giant telescopes, such as the E-ELT.

Contents

1	Introduction	1
1.1	Extrasolar Giant Planets	1
1.2	Detecting Exoplanets	2
1.2.1	Radial Velocity	4
1.2.2	Transit Photometry	4
1.3	Characterizing Exoplanets	5
1.4	Star-Planet Interaction	8
1.4.1	Stellar Activity	8
1.4.2	Planet-induced Stellar Activity	8
1.4.3	Planetary Emission Induced by Stellar Activity	9
1.5	The H_3^+ Diagnostic	10
1.5.1	Theoretical Spectra of H_3^+	11
1.5.2	H_3^+ in the Interstellar Medium	11
1.5.3	H_3^+ in the solar system	13
1.5.4	H_3^+ in Extrasolar Giant Planet Atmospheres	14
1.6	Methods and Motivation	15
2	The Star-Planet Systems	17
2.1	HD 209458	17
2.2	GJ 86	17
2.3	HD 217107	17
3	Observations	19
3.1	The CRIRES Spectrograph	19
3.2	Observing Runs	20
3.3	Preparation of the Raw Data	20
3.4	Telluric Absorption Correction	22
3.4.1	Telluric Correction for the Spectra of HD 209458	23
3.4.2	Correction of Telluric Spectral Features with <code>molecfit</code>	23
4	Data Analysis	29
4.1	Analysis of the CRIRES Spectra of HD 209458	29
4.1.1	Radial Velocities of HD 209458 b	29
4.1.2	Direct Search	29
4.1.3	Cross-correlation Approach	29
4.1.4	Search for Emission with Shift and Add	31
4.2	Analysis of the spectra of HD 217107 and GJ 86 for H_3^+ Emission Features	34

4.2.1	Radial-velocity Detected Planets and Possible Inclination Values	34
4.2.2	Intranight Radial Velocities Shifts of the Planets Versus H_3^+ Line Width . .	35
4.2.3	Residual Telluric Features	36
4.2.4	Direct Search for H_3^+ in the Spectra of HD 217107 and GJ 86	39
4.2.5	A Cross-Correlation Approach for the Search for H_3^+ Emission	42
5	Results	47
5.1	Results for HD 209458	47
5.1.1	Emission limits from the Shift and Add Results	47
5.2	Results for the Spectra of GJ 86 and HD 217107	48
5.2.1	Emission Limits	49
5.3	Prospects for H_3^+ Observations in the Future	52
5.3.1	Ground Based Instrumentation	52
5.3.2	Space Based Instrumentation	53
6	Summary	55
	Bibliography	57

List of Figures

1.1	Mass vs. semi-major axis in logarithmic scaling for all confirmed exoplanets from the exoplanet.eu plotting tool. Earth and Jupiter are added for comparison and orientation. The central-to-left cloud of exoplanets with high masses in short orbital distances comprises the hot Jupiter planets.	3
1.2	Illustration of the radial velocity method. The exoplanet and its host star orbit around their common center of mass. The light that is emitted towards the observer on Earth is red- or blue shifted due to the Doppler effect, depending on the motion of the host star. Image credit: ESO	5
1.3	Transiting Exoplanet: the orbiting planet is shown at the beginning of the primary eclipse when the planet crosses the disk of its host star. The light blue ring indicates the planet's atmosphere which is filtering a small fraction of the stellar light. The secondary eclipse describes the phase of the orbit, where the planet is occulted by the star.	7
1.4	Zoom-in of a UVES spectrum of HD 149961 from the UVES-pop atlas. The chromospheric activity is visible as emission in the line cores of the Ca II H & K lines (highlighted by the orange ovals).	8
1.5	Image of Earths Aurora borealis. Image credit: Anders Jilden / CC0.	10
1.6	H3+ model spectrum calculated for the wavelength ranges that we observed with CRIRES at the VLT. The intensities are calculated with the intensity line calculator from the 'H ₃ ⁺ Ressource Center' (http://h3plus.uiuc.edu/).	12
1.7	Infrared view of the aurora over Jupiter's south pole, taken with the Juno spacecraft. Image credit: NASA, JPL-Caltech, SwRI, ASI, INAF, JIRAM	13
3.1	CRIRES on the Nasmyth platform in front of the telescope mounting structure of UT1. The vacuum vessel hosting the optical bench and the detector array is on the right side of the image. The framework of the 8 m telescope can be seen in the background. Image credit: ESO	19
3.2	Optical layout of the CRIRES spectrograph from Kaeufl et al. (2004)	21
3.3	LBLRTM atmospheric modeling results for one spectrum of HD 209458 for all four CRIRES detectors. Upper panels: CRIRES spectrum (black) with its corresponding telluric model spectrum (green). Lower panels: Observed-Computed (O-C) and Observed/Computed (O/C) residuals. The O/C residual spectra were used in the analysis.	24

3.4	GJ 86: atmospheric modeling results for the correction of telluric absorption with <code>molecfit</code> . The figure shows one of the GJ 86 spectra for all four CRIRES detectors. Upper panels: CRIRES spectrum (black) with the corresponding telluric model spectrum (green). Lower panels: Observed-Computed (O-C) and Observed/Computed (O/C) residuals. The O/C residual spectra were used in the analysis.	25
3.5	HD 217107: atmospheric modeling results for the correction of telluric absorption with <code>molecfit</code> . For detailed description see Fig. 3.4	26
4.1	HD 209458: radial velocities (km/s) over time in days. The time span of the observations is marked by the purple shaded area in the large plot. In the inset, the crosses indicate the separate observations. The vertical line highlights the end of the secondary eclipse, calculated from the ephemeris value from Knutson et al. (2007). All spectra left of the vertical line were recorded during secondary eclipse. Hence, four spectra contain the combined light of the star and its orbiting planet.	30
4.2	Cross-correlation results. Upper to lower panels show the four CRIRES detectors. The spectrum that was observed last during secondary eclipse is subtracted from each combined light spectrum. The resulting spectra are cross-correlated and the main peak is fitted with a Gaussian. We derive the radial velocity value from the maximum of the fit and expect a planetary signal to shift the Gaussian fit sideways, producing a signal between 0 km s^{-1} and the differential radial velocity in case of a detection. The squares indicate the calculated differential radial velocity values from the time of observation and ephemeris and the crosses show the measured radial velocity from the cross-correlation. The error bars lie within the symbol size. Image credit: Lenz, A&A, 589, A99, 2016, reproduced with permission ©ESO	32
4.3	Spectra of HD 209458, a zoom-in for all four detectors is shown. All observed combined light spectra, were shifted to their apparent radial velocity at the time of observation and then added up binwise. The dashed lines indicate the positions where the H_3^+ emission lines are expected. Image credit: Lenz, A&A, 589, A99, 2016, reproduced with permission ©ESO	33
4.4	HD 217107: radial velocity of planet b for $i = \{30; 40; 50; 60; 70; 89; 90\}$ degrees. The vertical bars indicate the time of the observations translated to the phase in the orbit (grey) and the corresponding errors (light pink).	34
4.5	Radial velocity curves for GJ 86 b, see caption of Fig. 4.4 for a detailed description.	34
4.6	HD 217107 b: maximum of the intranight radial velocity shift over inclination for night 1.	35
4.7	HD 217107 b: maximum of the intranight radial velocity shift over inclination for night 2.	36
4.8	GJ 86 b: maximum intranight radial velocity shift over inclination for night 1. . .	36
4.9	GJ 86 b: maximum intranight radial velocity shift over inclination for night 2. . .	36
4.10	HD 217107: Overview of the telluric correction results. Top to bottom are all four CRIRES detectors. Mean telluric model (blue), one single observed spectrum (green), the mean spectrum after telluric correction (black), a single spectrum after telluric correction (red). All spectra were shifted to the same topocentric velocity frame and shifted on the y-axis for better visibility.	37
4.11	Same as Fig. 4.10 , but for GJ 86	38

4.12	Top to bottom: CRIRES detector No. 1, No. 2 and No. 3. The panels show the mean spectrum of HD 217107 (black), computed from the first half night of observations from night 1 (night 1a). The estimate of the FWHM for the H_3^+ emission lines is shown in red at the rest wavelength positions. The range of the line shift due to the planetary radial velocity is represented by the blue markers.	39
4.13	HD 217107: same as Fig. 4.12 but for the second half night of observations (night 1b).	40
4.14	HD 217107: same as Fig. 4.12 but for observing night 2.	40
4.15	Same as Fig. 4.12 but for GJ 86, observing night 1.	41
4.16	GJ 86: same as Fig. 4.12 but for GJ 86, observing night 2. Note, that the x-axis is shifted 1 nm towards smaller wavelengths, compared to the other figures for better visibility of the wavelength regime where H_3^+ emission lines are expected due to the rv shift.	41
4.17	HD 217107: Input spectra for the cross-correlation results which are shown in Fig. 4.18. Detectors No. 1-3 are shown from top to bottom. The normalized mean spectrum for night 1a is shown in black, the normalized mean spectrum for night 2 in red. The shift of the spectra due to the correction for the topocentric velocity is visible in the line cores of the absorption lines.	43
4.18	Cross-correlation results for HD 217107, using night 1a and night 2 as input. Detectors No. 1-3 are shown. The plot shows the radial-velocity range where the planetary signal would occur. This curve is corresponding to the red box in the inset image, which gives an overview on the cross-correlation result. Atmospheric emission of H_3^+ would be expected to cause signals in each of the Detectors at the same planetary radial velocity.	44
4.19	Cross-correlation results for HD 217107. Using night 1b with night 2 as input, detectors No. 1-3 are shown. For detailed description, see Fig. 4.18.	44
4.20	Input spectra from GJ 86 for the cross-correlation in Fig. 4.21. For a detailed description, see Fig. 4.17.	45
4.21	Same as Fig. 4.18 but for GJ 86.	45

Chapter 1

Introduction

1.1 Extrasolar Giant Planets

The planets of our own solar system are typically classified by astronomers into the following categories: rocky planets, gas giants and ice giants. The category of the rocky planets includes Mercury, Venus, Earth and Mars. These planets are called ‘rocky’ since they have a definite solid core where one would, in principle, be able to stand on the surface, without being crushed by gravity. Three of them, Venus, Earth and Mars have a relatively thin, but still prominent atmosphere, while Mercury, the innermost planet, has almost none. Jupiter and Saturn are gas planets, or gas giants, as they are much larger than Earth and have atmospheres that consist mostly of hydrogen and helium. The overall density of these planets is much lower than those of the rocky planets. The ice giants are Uranus and Neptune, these planets consist mostly of elements that are heavier than hydrogen and helium.

In the solar system, the rocky planets are located as the ‘inner planets’ that are orbiting closer around the Sun, while the outer four planets fall into the gas giant and ice giant categories. The exploration and observation of the solar system was the basis from which planet formation theories were developed, until the first detection of an exoplanet around a Sun-like star (Mayor and Queloz, 1995) questioned the previously defined categories. The detected planet 51 Peg b is very close to its host star and has an orbital period of only 4.2 days. Its mass was derived to be 0.47 Jupiter masses. The existence of this close-in gas giant planet could not

be explained by the existing planet formation theories at this time. But due to the subsequent discoveries of more and more close-in extra-solar giant planets (EGP), a new category called ‘hot Jupiter’ was added to the list of planet categories. The existence of hot Jupiter planets suggested that these giant planets migrated over time from a wider orbit around their host star into the orbit that they were now detected in and planet formation theories were adopted to these new findings.

Current theories explain the existence of hot Jupiter planets by two types of migration, the first being migration from a much more outward orbit due to gravitational disturbances caused by the nearby passing of a star or other planet. This disturbances yield to an eccentric orbit that is assumed to settle down to a close-in circular orbit over time. The second formation theory is called disk migration and describes the inwards migration of the young gas planet due to gravitational interaction with the gaseous disk (the so called protoplanetary disk) from which it forms.

It is expected that the most common type of exoplanet have radii in between the radii of Earth and Neptune (Batalha et al., 2013) and short orbital periods. These mini-Neptunes are assumed to have a solid core and a gaseous envelope, consisting mostly of hydrogen and helium. Another significant fraction of discovered planets are close-in hot Jupiters, while planets with longer periods are found much less often. This can be explained by the fact, that the two most successful detection methods for exoplanets, namely the transit method and the

radial velocity method (see Sec. 1.2), both have a detection bias towards short period planets and larger masses.

Figure 1.1 gives an overview over the confirmed exoplanets that are within an semi-major axis of 5 AU (up to April 2019). The figure shows the planetary mass (on a logarithmic scale and in units of Jupiter masses M_{Jup}) as a function of the orbital distance of the planet to its host star, also on a logarithmic scale.

The progress in instrumentation that followed the first discovered exoplanets led to more and more confirmed detections. To this day the most successful mission for exoplanet detection is the Kepler mission: according to the NASA exoplanet archive, over 60% of all confirmed exoplanets today have been discovered with Kepler lightcurves (2327 out of 3735 confirmed exoplanets). This was achieved by looking at a huge number of stars, since the chances for any of those stars to undergo a transit is very small. But, due to the large number of stars observed, transiting exoplanets can be observed nonetheless.

The characterization of exoplanet atmospheres requires observations at the frontier of instrumentation. The first measurement of any atom of an exoplanet's atmosphere was the detection of sodium in the atmosphere of HD 209458 b by Charbonneau et al. (2002). Several detections of atmospheric components followed, the majority being detected in the atmospheres of hot Jupiters, which provide relatively strong signals compared to smaller planets. Despite the challenges that arise from attempting to access the atmospheres of exoplanets, for hot Jupiter planets it is even possible to gain information about the dynamics of the atmosphere, e.g. the loss of the atmosphere due to the stellar irradiation (e.g. Vidal-Madjar et al. (2004)), or the existence of clouds in exoplanet atmospheres (Iyer et al., 2016). However, these observations remain difficult and the observed data need to be supplemented by theoretical models.

One of the still unsolved mysteries is, whether hot Jupiters have a magnetic field or not. Jupiter's

magnetic field interacts with the solar wind, causing bright auroral features from the poles up to mid-latitudes, which can be observed in the infrared, as well as in ultraviolet wavelengths (Drossart et al., 1989; Ballester et al., 1996). Theories about the observability of auroral emission lines from hot Jupiters have been discussed in literature for almost 20 years (Miller et al., 2000) and there is still excitement about the possible advances in formation theory and atmospheric behavior of hot Jupiter planets that these detections could deliver.

H_3^+ is the best candidate molecule for the detection of auroral features in a hot Jupiter atmosphere. The molecule emits in infrared wavelengths, mainly in two bands around $2\,\mu\text{m}$ and $4\,\mu\text{m}$.

Even though theoretical predictions for the emission strengths differ by several orders of magnitudes, depending on the model, H_3^+ emission of hot Jupiter atmospheres could be detectable with ground-based instrumentation. The goal of this thesis is to find H_3^+ emission of hot Jupiters, defining the detection limits of these observation and comparing them to the theoretical model predictions.

1.2 Detecting Exoplanets

The two most successful methods for exoplanet detections are the radial velocity (RV) and the transit method and will be introduced in more detail in the following subsections. Both methods detect exoplanets in an indirect way and combined detections comprise 93% (72% transit detections + 20% RV detections) of all confirmed detected exoplanets so far¹. Further detection methods include e.g. directly imaging the light of exoplanets, which is very challenging due to the low brightness contrast between the planet and the star. Therefore the planet has to be very bright and in a large orbit around its host star (Kalas et al., 2008; Chauvin et al., 2017). The orbits of planets detected with direct imaging reach from 10 to 100 AU

¹ exoplanet.eu on April 30th 2019

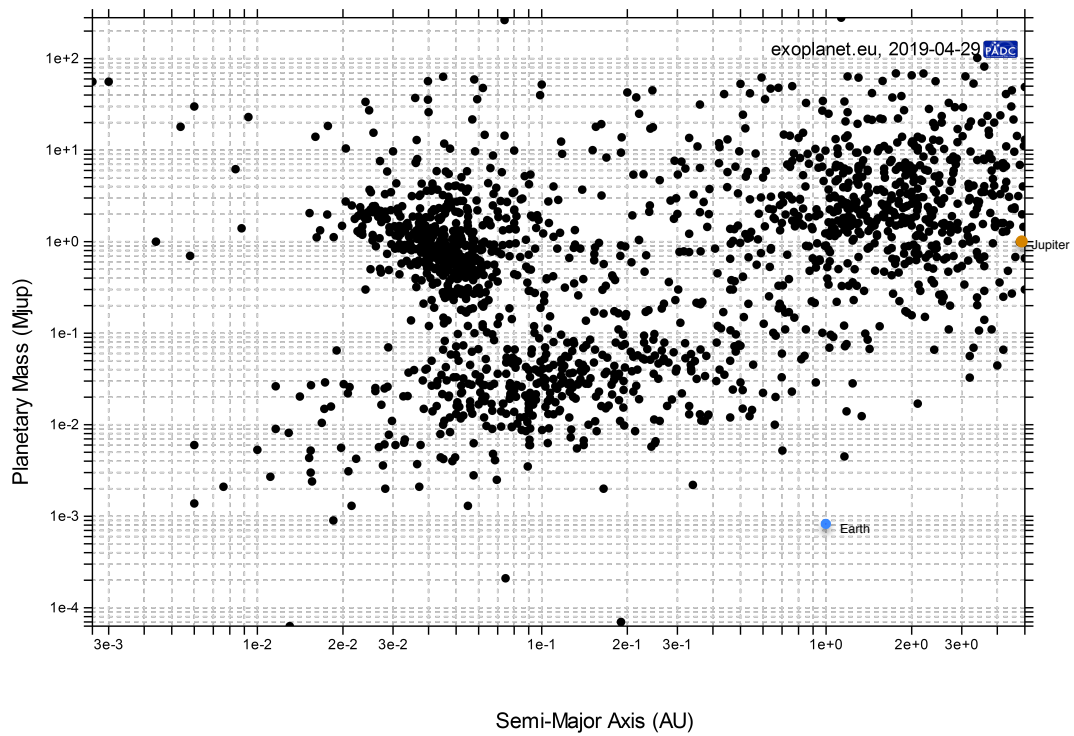


Figure 1.1: Mass vs. semi-major axis in logarithmic scaling for all confirmed exoplanets from the exoplanet.eu plotting tool. Earth and Jupiter are added for comparison and orientation. The central-to-left cloud of exoplanets with high masses in short orbital distances comprises the hot Jupiter planets.

wide orbits. Current instrumentation for these observations are e.g. the Gemini Planet Imager (Macintosh et al., 2006) and SPHERE at the Very Large Telescope (VLT) (Beuzit et al., 2006).

1.2.1 Radial Velocity

The RV method is based on measuring the Doppler effect for planet hosting stars. A planet and its host star orbit their common center of gravity. For most star-planet systems this is inside the host star due to its much higher mass compared to the planet. Depending on the orientation of the orbit this can lead to a velocity component of the star towards or away from the observer. Due to the Doppler effect this movement shifts the frequency of the light observed from the star which can be described by

$$f = \left(1 + \frac{v_{obs} - v_s}{c}\right) f_0 \quad (1.1)$$

where f is the observed frequency of the light, $v_{obs} - v_s$ is the velocity of the light source relative to the observer, c is the speed of light and f_0 is the rest frequency of the light emitted by the star.

Fig. 1.2 illustrates the principle of this effect. The periodic shift of the stellar spectra lines can be measured with a high resolution spectrograph which has to be calibrated against spectral lines from a light source that is moving with the observer (e.g. hollow cathode lamps, telluric atmospheric lines or gas cells).

The semi-amplitude K of the Doppler signal is described as:

$$K = \left[\frac{2\pi G}{P} \right]^{1/3} \frac{M_P \sin i}{(M_S + M_P)^{2/3}} (1 - e^2)^{-1/2} \quad (1.2)$$

with P being the orbital period, M_S the mass of the host star, M_P the mass of the planet, e the excentricity of the orbit, G the gravitational constant and the inclination i , which describes the angle between the normal

to the orbital plane and the line of sight. The observer measures the projected movement of the star in the line of sight. The inclination angle cannot be measured by this method, hence, if i is unknown, only the lower limit of the planetary mass M_P can be determined.

The method is biased towards large and close-in planets, since these objects have larger gravitational impact on their host star and produce a larger semi-amplitude, which makes them easier to be detected. The host star itself also has an impact on the detectability of potential exoplanets: Stellar activity induces signals on its own which look similar to RV-signals of planets. These signals are essentially creating a noise floor which makes detecting planets with smaller RV-signals much more difficult. Hence, the activity of the star influences the minimum mass that can be detected over this stellar RV jitter.

1.2.2 Transit Photometry

If the orbit of an exoplanet is almost perpendicular to the plane of the sky (which is commonly called ‘edge-on’), the planet crosses (transits) the stellar disk periodically within every orbit. The occultation of the stellar disk by the planet can be measured by photometric observations as a dimming of the stellar light. The drop in the stellar flux can be described with the following equation:

$$\Delta F = \left(\frac{R_P}{R_S} \right)^2. \quad (1.3)$$

ΔF is the observed change of flux during the transit (transit depth), R_P the radius of the planet and R_S the stellar radius. When observing several transits of an exoplanet it is possible to determine the period P of the orbit. The information from the transit light curve can be used to determine the orbital period, orbital inclination, planet radius and the semi-major axis; the approach is described in detail in Seager and Mallén-Ornelas (2003). The transit light curve can also deliver information about star spots or even allow the detection of other

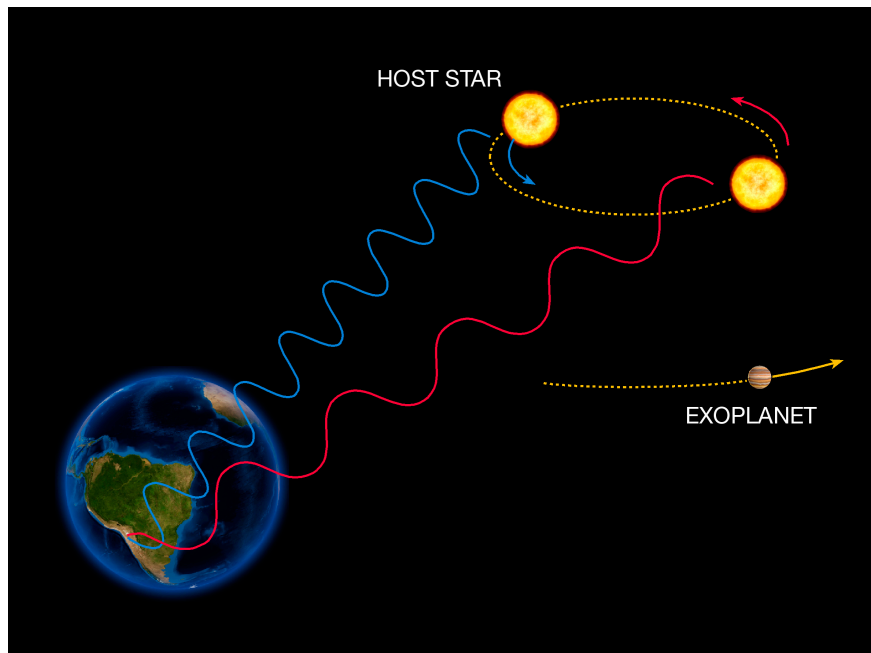


Figure 1.2: Illustration of the radial velocity method. The exoplanet and its host star orbit around their common center of mass. The light that is emitted towards the observer on Earth is red- or blue shifted due to the Doppler effect, depending on the motion of the host star. Image credit: ESO

non-transiting planets in the system by measuring variations in the transit timing (TTV). The dimming of the stellar light caused by a transiting exoplanet is small, even for close-in hot Jupiter planets the signal strengths reach only around 1% of the total flux. Hence, large planets with short periods are easier to detect than planets with larger periods and/or small planets, that cause only very small transit signals. A detection of a transiting exoplanet candidate is usually confirmed by RV observations in order to rule out a false detection that might be caused by, e.g., a blend from a background binary system.

1.3 Characterizing Exoplanets

All of the planets of the solar systems have been studied in great detail from the ground and with spacecraft missions and are still subject of missions today. Space probes were landed on the surface of Venus, Mars and even the Jupiter moon Titan and were operated there

successfully for exploration. Also, all of the solar system planets were visited by spacecrafts with fly-byes or even dedicated orbiting missions. One of the current missions that is orbiting a solar system planet is Juno, which was launched in 2011, reached Jupiter after five years and is equipped with instrument to explore the planets origin, interior structure, atmospheric composition and dynamics as well as the polar magnetosphere and aurora (Bolton et al., 2017).

While the characterization of the solar system planets is possible by direct observations, the available techniques for the characterization of exoplanets are mostly indirect and require the exoplanet to be transiting its host star. If a planet is observed with both, the radial velocity and the transit method, the mean density of the planet can be derived. The most reliable conclusions from these bulk densities can be drawn, when the computed value is considerably low and thus requires the planet to own a gaseous envelope. The bulk density cannot

determine the internal structure of planets with small radii (Adams et al., 2008), e.g. it can be the same for a small rocky planet with a thin and light atmosphere and a small water-dominated planet.

This degeneracy can be broken when accessing the atmosphere of the planet. The atmospheric composition and temperature characterizes the nature of a planet and from these parameters the habitability of an exoplanet can be determined. Determining the atmospheric composition of an exoplanet is very challenging and therefore most observations are focused on analyzing and understanding the composition of the atmospheres of giant planets, since those produce larger signals compared to those of smaller exoplanets (e.g. Swain et al., 2008; Stevenson et al., 2010).

One of the common techniques applied for the characterization of exoplanet atmospheres is transmission-spectroscopy, where spectra of the host star are being taken while the planet is transiting in front of the star. Figure 1.3 illustrates the geometry of a transiting planet, the planet is shown at the beginning of the transit, which is also called primary eclipse, and shortly before being occulted by the star, which is called secondary eclipse. During primary eclipse the solid part of the planet is simply blocking the light while the planet's atmosphere filters a small fraction of the stellar light. In the figure, the planet's atmosphere is indicated by the light blue ring around the planet. The stellar light shining through the atmosphere will get additional spectral lines due to absorption by the atoms or molecules and therefore receives an imprint of the atmosphere. Additionally, the stellar light is blocked by optically thick atoms or molecules in the atmosphere, which causes the transit time, observed in these particular wavelengths to vary. Therefore, observing a wavelength dependent transit also allows to analyze the planet's atmosphere. These measurements are extremely difficult as the signal strength, the fraction of the light that is blocked by the atmosphere of the planet, is only up to 1000 ppm for giant

planets in close orbits around Sun-like stars. Hence, for the even smaller signals from planets in the habitable zone, current instrumentation is not sensitive enough.

Transit spectroscopy was used successfully to detect atomic sodium (Charbonneau et al., 2002), hydrogen, carbon and oxygen (Vidal-Madjar et al., 2003, 2004). These observations were carried out with space based instruments, namely the Space Telescope Imaging Spectrograph (STIS) at the Hubble Space Telescope (HST).

If an exoplanet is transiting its host star, the planet can be observed during transit, as described above, or shortly before and after secondary eclipse (when the planet is behind the star). The secondary eclipse allows to observe the host star without the planet. These observation can then be subtracted from the observations where the planet is present. Hence, one can disentangle the stellar from the planetary signal.

Direct detection of non-transiting exoplanets is possible by detecting the emission signals of the exoplanet's atmosphere. This method was successful using medium-resolution spectroscopy for bright exoplanets in a wide orbit, e.g. to characterize the system HR 8799 (see Barman et al. (2015) for an overview). Planets in a close orbit around their host star are presumed to be tidally locked. Hence, emission lines are not broadened by rotation of the planet. These narrow lines can be detected with high resolution spectroscopy, when accounting for the Doppler shift due to the planets motion around its host star.

Ground-based observations offer much higher photon collecting areas compared to space based instrumentation. Also, the available spectral resolution can be extremely high, reaching up to a spectra resolving power of $R \sim 100,000$.

One of the main challenges in the data of ground-based high resolution spectroscopy lies in the correction of the telluric contamination. These systematic effects are caused by absorption and/or scattering of the light by Earth's atmosphere. These telluric features can be

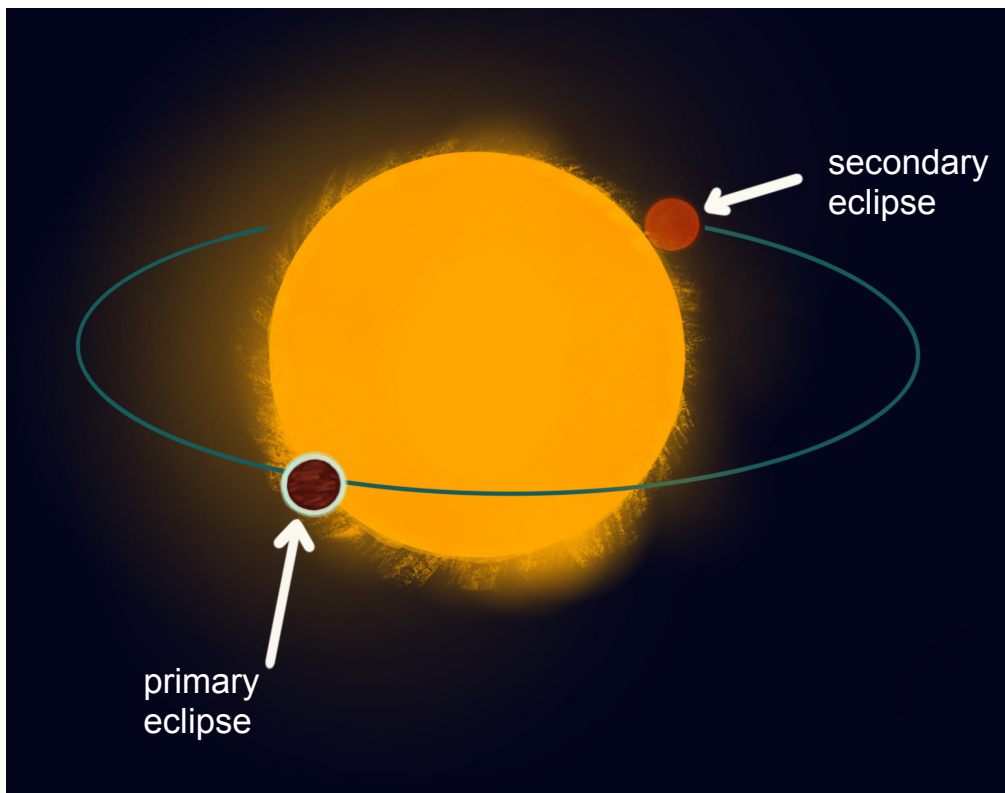


Figure 1.3: Transiting Exoplanet: the orbiting planet is shown at the beginning of the primary eclipse when the planet crosses the disk of its host star. The light blue ring indicates the planet's atmosphere which is filtering a small fraction of the stellar light. The secondary eclipse describes the phase of the orbit, where the planet is occulted by the star.

very prominent in distinct wavelength regions and require a very careful correction in order to retrieve the stellar signal, or even planetary emission and/or absorption lines. Snellen et al. (2010) successfully applied high-resolution spectroscopy to detect absorption lines in exoplanet atmospheres. They measured the imprint of the exoplanet's Doppler-shifted lines in the stellar spectra through cross-correlation techniques and detected CO in the atmosphere of HD 209458 b. The technique was successfully repeated for other stars and molecules, even for non-transiting planets (Brogi et al., 2014). These observations were carried out with the ground-based high resolution spectrograph CRIRES at the VLT. A direct detection of planetary atmospheric lines allows the determination of the planetary radial velocity and from this, the calculation of the true mass of the planet.

1.4 Star-Planet Interaction

1.4.1 Stellar Activity

The term stellar activity comprises all phenomena that are related to the dynamic magnetic field of a star and is observable as sun spots, activity cycles, chromospheric plagues, coronal loops, emissions in various wavelength ranges and other features. These phenomena observed in stars with spectral types from late A to late M, are linked directly to magnetic dynamo processes in the interior of a star. The internal structure of the star and the stellar (differential) rotation are responsible for the strength of the dynamo and the magnetic field configurations of the star. For the sun, it is possible to observe spatially resolved activity features, such as Sunspots, flares or direct observation of the corona. The magnetic activity of stars however, can only be observed disk-integrated. Activity of the chromosphere is usually measured from the Ca II H & K line profiles, or the H α line for late type stars. Coronal activity is measured in X-rays. There are also approaches to directly measure magnetic fields in stars or

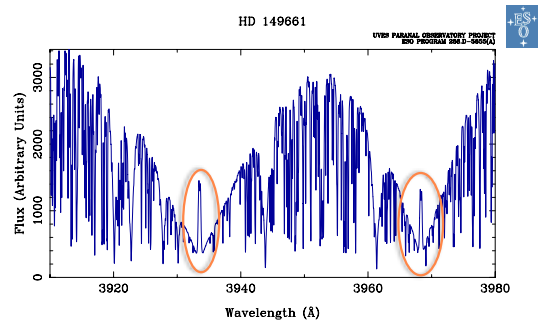


Figure 1.4: Zoom-in of a UVES spectrum of HD 149661 from the UVES-pop atlas. The chromospheric activity is visible as emission in the line cores of the Ca II H & K lines (highlighted by the orange ovals).

to reconstruct spot patterns over time in order to derive the dynamical behaviour of magnetic fields in stars. In Fig. 1.4 the Ca II H & K line profiles of HD 149661, a K2V star, from the UVES-pop Atlas² are shown. The Ca emission is visible in the line cores of the Ca II H & K (highlighted by the orange ovals).

1.4.2 Planet-induced Stellar Activity

Close binary stars show enhanced activity levels compared to single stars of the same age and type due to tidal interaction of the bodies (Schrijver and Zwaan, 1991). The modulation of activity level due to an accompanying body is also expected to translate to stars with close-in giant planets. Cuntz et al. (2000) were the first to suggest two scenarios for star-planet interactions (SPI): A periodic change of the stellar activity levels could be caused due to tidal or magnetic interactions between the planet and its host star. Gravitational interaction of the two bodies induces tidal bulges on the star that can increase the turbulence in the photosphere and amplify stellar activity in these regions. Reconnection of planetary and stellar magnetic field lines could increase stellar activity in the

² http://www.eso.org/sci/observing/tools/uvespop/field_stars_uptonow.html

distinct region of the reconnection. Hence, signatures of magnetic SPI would be an indirect method to prove the magnetic field of an exoplanet. Magnetic interaction is also known from Jupiter and its moons, i.e. Jupiter and Io are connected via magnetic flux tubes which causes an active footpoint, visible in Jupiter's Aurora (Clarke et al., 2002).

There have been dedicated searches for SPI signatures in stellar atmospheres in the chromosphere, as well as in the corona. Attempts to observe SPI-induced coronal activity with X-ray measurements were carried out, e.g., by Poppenhaeger et al. (2010) and Saar et al. (2008). However, the detected activity signatures could not be assigned unambiguously to a planet-induced effect. Shkolnik et al. (2003) observed a sample of five hot Jupiter systems and searched for chromospheric variability in the Ca II H & K line cores, including HD 179949 and ν And. They reported the variability of the Ca II K line cores of HD 179949 to be in phase with the orbital period of the planet. Also, the Ca II K line flux in ν And was observed to vary with the planet's rotation period (Shkolnik et al., 2005). However, these findings could not be observed in further observations.

In Poppenhaeger et al. (2011) we aimed to measure the previously reported SPI signatures in ν And's corona and chromosphere, and conclude from our measurements that SPI effects might only be observable in certain time intervals, depending on the magnetic configuration of the system. Our observations showed only variability in phase with the stellar rotation period. A long-term observation of the chromospheric activity of stars that are hosting short-period planets would be very beneficial for generating improved statistics on the behavior of stellar variability and planet induced activity.

1.4.3 Planetary Emission Induced by Stellar Activity

Atmospheric Evaporation

An exoplanet can undergo extreme irradiation of its host star, if it is orbiting in a very close-in orbit. The high level of stellar irradiation cannot only inflate the planets atmosphere, but close-in giant exoplanets can also undergo atmospheric evaporation. The star irradiates the upper layers of the exoplanet's atmosphere intensely by X-ray and EUV- emission, which leads to a loss of fractions of the atmosphere. Atmospheric evaporation can be detected with transit observations. One of the main characteristics of atmospheric escape of EGPs are escaping ions and atoms which extend the transit duration in certain wavelengths. Neutral atomic hydrogen escaping from the atmosphere was measured in Lyman- α in space-based observations with the Hubble Space Telescope for HD 209458 b and HD 189733 b (Vidal-Madjar et al., 2003; Lecavelier Des Etangs et al., 2010). Both planets are hot Jupiter planets in very short orbits around their host stars. Several models have been derived in order to describe evaporation rates of EGP's (Lammer et al., 2003, e.g.). In principle, a planet undergoing atmospheric evaporation could have its whole atmosphere stripped during the lifetime of it host star on the main sequence. The remnant core of a hot Jupiter planet that lost its whole gaseous envelope would fall into the hypothetical class of *chthonian planets* (Hébrard et al., 2004).

Aurorae in the Solar System

An Aurora forms when energetic particles precipitate the upper atmosphere of a planet, while streaming downwards along the magnetic field lines of the planet. In the case of the gas giants in the solar system, aurorae can be observed almost over the whole electromagnetic spectrum, from radio- to the infrared, optical, ultraviolet to X-ray emissions and have been studied in great detail (see e.g. Maillard and Miller



Figure 1.5: Image of Earth's Aurora borealis. Image credit: Anders Jilden / CC0.

(2011); Stallard et al. (2008b)).

The main formation process for aurorae on Earth is the interaction of the solar wind with the magnetosphere of the planet. On Earth, aurorae have been detected in the visible, as X-ray emission (Anderson, 1960) and radio emission (Lovell et al., 1947).

The colors of the visible aurora on Earth result from the emission of photons from excited oxygen (green, orange-red light) and nitrogen molecules (red light), returning to their ground state, as well as ionized nitrogen atoms, when regaining an electron (blue light). On Earth the northern aurora is called Aurora Borealis (see Fig. 1.5), whereas the southern aurora is called Aurora Australis.

Aurorae in Exoplanets

The findings from the observations of the planets in the solar system serve as ‘prototypes’ for the translation to models for atmospheres of exoplanet. For example, energetic electrons, which are precipitating downwards along high-latitude field lines on Jupiter, emit radio waves at the local cyclotron frequency (e.g. Zarka, 2007).

Exoplanets are expected to do the same and a radio quiet host star might allow the direct detection of such an exoplanet in radio emission (Gri  meier et al., 2011). Until now, there are

no radio detections of exoplanets reported in the literature, current campaigns are ongoing with the Low Band of the Low-Frequency Array (LOFAR) (Turner et al., 2018).

In principle, the observation of a planet’s aurora offers insights on the atmospheric and magnetospheric behavior of a planet. Because the observations of exoplanet atmospheres are currently at the instrumental frontiers of observability, favourable candidates for observational attempts for exoplanet aurorae are mostly giant planets in close orbits that are expected to undergo intense interactions with their host stars.

However, the detection of Proxima Cen b by Anglada-Escud   et al. (2016), a terrestrial planet around the Sun’s closest neighbouring star, brought up the suggestion by Luger et al. (2017) to gain access to the atmospheres of exoearths via their aurorae. Their candidate emission line for the observation of an earth-like aurora would be the O I line at 5777   , which is responsible for the green airglow in Earth’s Aurora borealis, as well as Aurora australis. Luger et al. (2017) discuss the observational difficulties of different intensities of a possible Proxima Cen b aurora and conclude that an observation of the estimated auroral strength of the O I emission would only be possible with optimal conditions and optimal instrumentation on a 30 m class telescope.

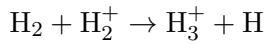
All giant gas planets of the solar system show auroral activity through the emission of H_3^+ . The molecule emits its energy in a few narrow lines in the infrared wavelength regime around $4 \mu\text{m}$. It is expected, that H_3^+ emission has an important role in the observation of exo-aurorae (Maillard and Miller, 2011), since most planet-hosting stars are dim around $4 \mu\text{m}$ and the planet-to-star contrast could be in favour of the observation of the planetary atmosphere through H_3^+ .

1.5 The H_3^+ Diagnostic

H_3^+ forms the most fundamental, stable and polyatomic molecule (Maillard and Miller, 2011).

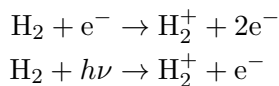
The molecular ion consists of three protons that are bound by two electrons. Its symmetric equilateral triangle shape prohibits a permanent dipole moment and thus possesses no allowed rotational modes that would be applicable for microwave spectroscopy (radio astronomy). In addition, UV- and optical spectroscopy cannot be used for the analysis of the ion: the stable electronic excited state is a triplet state with linear geometry and the resulting electronic transition and thus the spectrum would be very weak. However, the rotational-vibrational modes of the molecule are observable with infrared spectroscopy.

H_3^+ was discovered and identified by Thomson (1913) using an early form of mass spectroscopy. The formation pathway

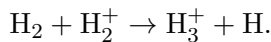


was identified by Hogness and Lunn (1925) and is an exothermic reaction by about 1.7 eV. The initial detection of H_3^+ in the laboratory was made by Oka (1980), who identified 15 lines from the infrared active ν_2 mode. A lot more lines have been detected since then (e.g. Majewski et al., 1994; Lindsay et al., 2001). Today, the progress in computational power enables theorists to reproduce these laboratory spectra from first principles with high accuracy.

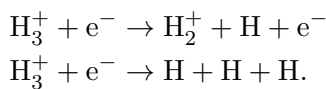
The formation process of H_3^+ (e.g. in Jupiter's atmosphere) can be described through the following pathways: at first H_2^+ is formed either by precipitating energetic electrons or by extreme ultraviolet radiation:



Then, H_3^+ is produced by:



The ion can be destroyed by the following dissociative recombinations:



1.5.1 Theoretical Spectra of H_3^+

The working groups of Benjamin McCall at the University of Illinois Astronomy Department and the group of Takeshi Oka, The Oka Ion factory, at the University of Chicago have published the ' H_3^+ Ressource Center' website³, which contains spectroscopic databases of H_3^+ , links to the Royal Society Discussion Meetings on H_3^+ in the past, and provides an online H_3^+ intensity calculator⁴. The intensity calculator makes use of the formulae from Neale et al. (1996) and produces a line list for a given frequency range. As an example, the theoretical spectrum from the calculator is shown in Fig. 1.6. The four graphs correspond with the wavelength ranges of the four CRIRES detectors used in our observations (see Sec. 3.2). The calculator delivers the intensity of the lines in the unit of equivalent widths of a certain H_3^+ column density. As shown in the figures, H_3^+ emits only in a few lines in the $4\text{ }\mu\text{m}$ region, in contrast to other molecules which produce a dense forest of lines within a narrow wavelength range (e.g. CO_2).

1.5.2 H_3^+ in the Interstellar Medium

Predictions for the existence of H_3^+ in the interstellar medium were already made in 1973 by Watson and Herbst and Klemperer, who independently suggested detailed models of a gas phase chemistry and proposed ion-molecule reactions as a baseline reaction for interstellar clouds. The first successful detection of H_3^+ -absorption was reported by Geballe and Oka (1996). Previous attempts for the observation of H_3^+ absorption in the interstellar medium were not successful but the advances in instrumentation during that time, as well as the adaption of the observation strategies finally led to this first detection of H_3^+ in a number of dense molecular clouds. The observed H_3^+ column densities were in the expected range of the chemical models. With the detection of H_3^+ in diffuse interstellar clouds (McCall et al.,

³ <http://h3plus.uiuc.edu/>

⁴ <http://h3plus.uiuc.edu/criteval/calc.shtml>

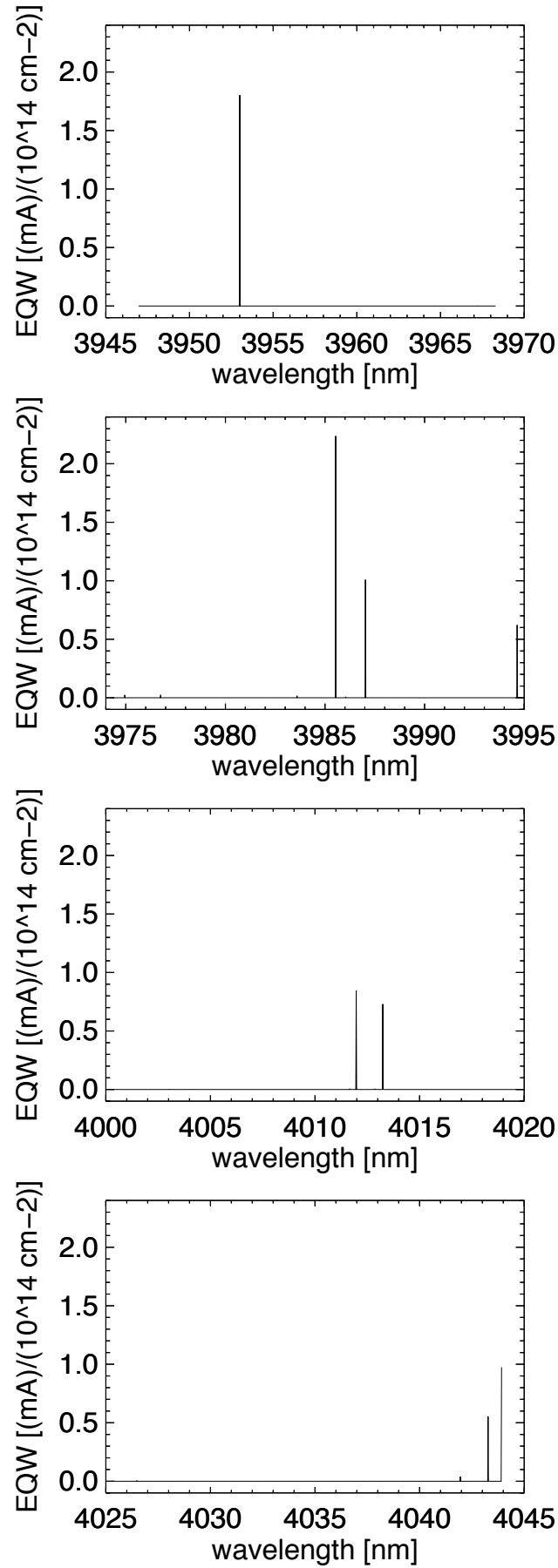


Figure 1.6: H₃⁺ model spectrum calculated for the wavelength ranges that we observed with CRIRES at the VLT. The intensities are calculated with the intensity line calculator from the ‘H₃⁺ Ressource Center’ (<http://h3plus.uiuc.edu/>).

1998), the existing models about the chemical behavior of the ion in the interstellar space were challenged, since the column densities of H_3^+ derived from the observations were larger than expected by the theoretical models. Interstellar H_3^+ has been measured only in absorption, while emission of H_3^+ has been only observed within the atmospheres of the gas giant planets of our solar system.

1.5.3 H_3^+ in the solar system

The detection of H_3^+ in Jupiter's southern auroral zone was the first discovery of the ion in space (Drossart et al., 1989). H_3^+ was found in data that was originally recorded for the confirmation of H_2 emission in the auroral regions of Jupiter in between 2 and $2.2\ \mu\text{m}$. The detection of the $2\nu_2(l=2)$ overtone band of H_3^+ in the infrared spectrum led to more observations using spectroscopy and spectral imaging. 42 lines of the fundamental ν_2 band at $4\ \mu\text{m}$ were detected by Maillard et al. (1990).

H_3^+ is produced in the upper atmosphere of Jupiter, where the concentration of methane (CH_4) is low. Thus, although the fundamental H_3^+ band is at the same wavelength range as the strong ν_3 band of CH_4 , the spectra around $4\ \mu\text{m}$ contain only H_3^+ lines outlying from a low continuum level. The production of H_3^+ emission in the polar regions is induced by high energy electrons which are accelerated into the upper atmosphere along the magnetic field lines. In the middle to lower latitudes of Jupiter a fainter H_3^+ signal can be measured. Although the magnetospheric region includes the orbit of Io, the origin of the ionization sources for the mid-to-low latitude emission is still being discussed (Maillard and Miller, 2011). Giles et al. (2016) report the detection of previously unknown H_3^+ emission lines in the $5\ \mu\text{m}$ window. These observations were carried out with CRIRES at the VLT.

The Juno spacecraft (NASA) launched in 2011 and its mission is to measure Jupiter's atmospheric composition, as well as its magnetic and gravitational field, and to study the po-

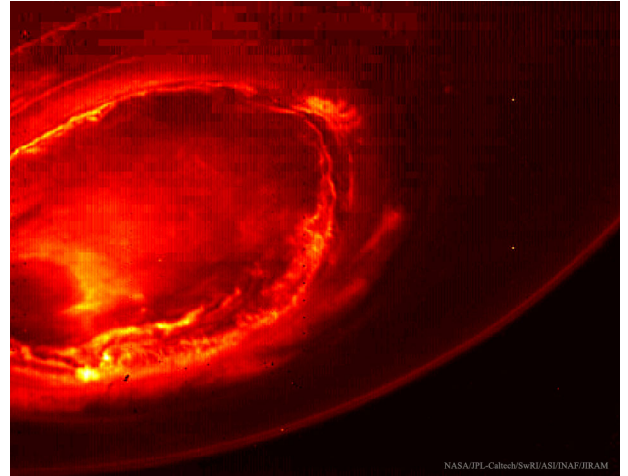


Figure 1.7: Infrared view of the aurora over Jupiter's south pole, taken with the Juno spacecraft. Image credit: NASA, JPL-Caltech, SwRI, ASI, INAF, JIRAM

lar magnetosphere of the planet (Bolton et al., 2017). In Fig. 1.7 a Juno infrared image of Jupiter's southern aurora is shown.

H_3^+ has been used intensively as a tool to study the atmospheric and magnetospheric interaction of Jupiter (e.g. Miller et al., 1997; Stallard et al., 2002; Giles et al., 2016). On Jupiter, H_3^+ cools the upper atmosphere by infrared radiation into space. This effect is known as the ' H_3^+ thermostat' (Miller et al., 2006). Even during intense auroral events the H_3^+ thermostat helps balancing the heating due to particle precipitation (Melin et al., 2006). Spectroscopy of H_3^+ in the auroral zones was used to determine the temperature in Jupiter's thermosphere. Several studies were carried out and found temperatures around 1000 K (e.g. Maillard et al., 1990; Stallard et al., 2002).

The detection of H_3^+ in the atmosphere of Jupiter triggered the search for the molecular ion in the other giant planets of the solar system. While a strong emission was found in Uranus (Trafton et al., 1993), the auroral H_3^+ emission detected for Saturn was quite weak (Geballe et al., 1993). The measured column density for Saturn was two orders of magnitude lower than the column density of H_3^+ at the

south pole of Jupiter. Despite the weak signal, Stallard et al. (2008a) published the first images of Saturn's H_3^+ emission taken with a ground-based telescope.

1.5.4 H_3^+ in Extrasolar Giant Planet Atmospheres

Theoretical Emission Limits for H_3^+ emission of EGPs

The atmospheres of hot Jupiters are expected to be severely influenced by stellar EUV radiation. As described in Sec. 1.4.3, the host star could even cause the evaporation of the upper layers of the atmosphere. On Jupiter, the H_3^+ thermostat cools the upper atmosphere of the planet by infrared radiation into space. This effect is also expected to exist in hot Jupiters and could contribute to balance the heating of the atmosphere caused by the host star (Yelle, 2004). There are a few results from different models which aim to calculate the H_3^+ excess of an EGP atmosphere in a close orbit around its host star. The resulting emission limits differ in several orders of magnitude, depending on the underlying assumptions of the parameters as well as the complexity of the model:

The H_3^+ emission limit for a planet similar to τ_{Boo} b was estimated by Miller et al. (2000) to be on the order of $\sim 10^{17}$ W. Yelle (2004) used a one-dimensional atmosphere model for a hot Jupiter and calculated a limit for H_3^+ emission from the lower thermosphere of $1 \cdot 10^{16}$ W.

Koskinen et al. (2007) modeled H_3^+ emission of EGP within orbital distances between 0.05 AU and 1 AU. In their work, they use a coupled ionosphere-thermosphere model and test different planetary configurations with and without H_3^+ cooling in order to measure the thermospheric temperatures for these different scenarios. Once H_2 is thermally dissociated, the H_3^+ thermostat is destroyed. For EGP atmospheres that are in a very close orbit around their host star, this is the case: They undergo thermal dissociation of H_2 , which causes a breakdown of the thermostat. In con-

sequence, the heating to the host star increases which accelerates the atmospheric evaporation. From the modeling, they calculate the total power output of H_3^+ for a Jupiter-sized planet in a 0.1 AU orbit to be on the order of 10^{15} W. They also estimated a single line output flux of $\sim 10^{12}$ W for the intensity of the $Q(3,0)$ -transition.

Observational Attempts for H_3^+ Detection in Hot Jupiter Atmospheres

The first report for a detection of H_3^+ emission from a planetary system outside our solar system was by Brittain and Rettig (2002). They observed the star HD 141569 A and reported the detection of H_3^+ emission from the protoplanetary disk of the system and stated that the origin of the emission might be a clump of planet-forming gas. However, Goto et al. (2005) could not confirm the reported detection, while their measurements achieve comparable data quality to those of Brittain and Rettig (2002) and their calculated emission limits are significantly lower than the signal strengths reported by Brittain and Rettig (2002). The largest observational campaign for H_3^+ emission of EGP atmospheres was conducted by Shkolnik et al. (2006). Their observations were carried out with CSHELL at the 3m NASA Infrared Telescope Facility (IRTF). CSHELL is a high-resolution single order echelle spectrograph with a resolving power of $R \sim 30,000$. Shkolnik et al. (2006) collected data from six close-in EPGs for their search for emission of the $Q(1,0)$ -transition of H_3^+ at 3953.0 nm. They did not detect any emission and calculate the upper emission limit strengths of around $1 \cdot 10^{18}$ W from their data. The lowest limit is reached for their observations of GJ 436 with $6.3 \cdot 10^{17}$ W. Since this type of observations is very expensive in terms of observation time and requires a high-resolution infrared spectrograph, there was only one further attempt for H_3^+ emission observations from an extrasolar planet: Laughlin et al. (2008) observed τ_{Boo} with CSHELL and report no detection of H_3^+

emission from their measurements. They calculate an emission limit of $9.0 \cdot 10^{17}$ W from their data.

None of these reported observational attempts for H_3^+ emission from hot Jupiter atmospheres could detect any H_3^+ emission signals. The reported emission limits for the observations of hot Jupiters by Shkolnik et al. (2006) and Laughlin et al. (2008) are one to three orders of magnitudes larger than the theoretical emission limits estimated by Miller et al. (2000) and Yelle (2004).

1.6 Methods and Motivation

The observation of exoplanet atmospheres is very challenging and at the frontier of exoplanetary science. Hot Jupiters are the current test candidates for the study of exo-atmospheres, because they have large radii and high equilibrium temperatures ($T_{eq} \sim 1000 - 3000$ K) and therefore the star-planet contrast is favorable for an observation of the planets atmospheres with spectroscopic methods. Hot Jupiter planets are expected to be tidally locked: one side of the planet is always facing towards the host star. Hence, planetary atmospheric lines would not be broadened due to the planet's rotation. These lines could be accessible with high resolution spectroscopy. H_3^+ is one of the candidate molecules for the detection of exo-atmospheres, since it is a prominent feature in the infrared spectrum of Jupiter and also detected in the other gas giants in the solar system (see Sec. 1.4.3). It is therefore likely, that hot Jupiter planets that orbit within a certain range around their host star (close, but not too close) show enhanced H_3^+ emissions.

A few attempts to observe H_3^+ of hot Jupiter atmospheres have been carried out in the past, but no detection has been reported and the reported upper limits are well above the theoretical predictions. Since the expected emission lines of H_3^+ are very narrow, sensitivity increases proportional to the spectral resolution. Hence, CRIRES at the VLT with a resolving power of up to $R \sim 100,000$ mounted

on a telescope with a very large collection area (8 m) seemed to be the perfect fit for further attempts for the observation of H_3^+ emission from hot Jupiter atmospheres. High resolution spectrographs exist only as ground-based instruments because this type of instrument is simply too big to be sent into space. Unfortunately, ground-based instruments have the disadvantages of telluric contamination of the spectra due to Earth's atmosphere, especially in the infrared. However, in principle very high resolving power allows for the detection of individual molecular lines and different techniques for the removal of Earth's atmosphere from stellar spectra are available.

A direct measurement of H_3^+ emission from the atmosphere of an exoplanet would allow for the direct investigation of atmospheric composition and conditions. A detection would also allow to derive the temperatures in the thermosphere of these hot Jupiters and to measure ion densities. In addition, when an emission feature is visible over a certain period of time, it can be followed through the orbit and enable a direct measurement of the planetary radial velocity. In combination with the stellar radial velocity such a measurement allows to directly determine the model-independent stellar mass.

The data for this thesis were obtained in two VLT observation periods. The first run in the fall of 2010 had two different scientific goals for the observations: besides the observation of hot Jupiter planets around $4\mu\text{m}$ searching for H_3^+ emission features, we also planned to observe HD 189733 b in order to search for an unresolved bright emission feature around $3.25\mu\text{m}$, that was reported by Swain et al. (2010). HD 189733 b is a transiting planet and the emission feature found by Swain et al. was identified by the authors as CH_4 fluorescence emission from the planet's atmosphere. The reported intensity of the emission was very high and we expected CRIRES to have sufficient sensitivity in this wavelength region in order to unambiguously identify the feature, if present in the atmosphere. In case of a detection, we planned to follow the emission during

the orbit in order to measure the planetary radial velocity. However, our observations were obstructed severely by bad weather and only a minimum of our planned observations could be executed successfully.

Despite the bad weather, we were able to obtain spectra from the transiting planet HD 209458 in the $4\mu\text{m}$ setting, which we analyzed for possible H_3^+ emission features (see Chapter 4). Even from the very short observation time on the target we were able to show the capability of CRIRES for this kind of observation (see Sec. 5.1.1). In the following, we successfully applied for a second observing run with CRIRES. The targets for the second run were the hot Jupiter systems HD 217107 and GJ 86, which are both non-transiting systems. These systems were chosen aiming for two different scenarios: GJ 86 is very close to Earth, which increases the overall signal and thus the detection probability of a signal. HD 217107 is very close to its host star with an orbital distance of 0.07 AU. Its proximity to the host star could either increase the H_3^+ emission due to increased particle flux, or produce signs of the onset of thermal dissociation (Koskinen et al., 2007). A detection, in any of the star-planet systems, would allow to further investigate the thermospheric structure and atmospheric composition of the planet. This second observing run with CRIRES was carried out in the fall of 2012 and the data was obtained in service mode with the observations stretched over a couple of nights. More information about the data used for this thesis is given in Sec. 3.2.

Structure of this Thesis

This work is structured in the following way: Chapter 2 introduces the target planets for the search for H_3^+ emission and their host stars. Chapter 3 introduces the CRIRES spectrograph and gives an overview on the observing runs and the data processing. Chapter 4 describes the analysis of the data from both observation runs and the techniques that were applied to derive the emission limits for the

H_3^+ emission. Chapter 5 explains the derived results from the analysis and the obtained H_3^+ emission limits with the CRIRES spectrograph are put into context to other available and future instruments. Subsections 4.1.2 to 4.1.4 and 5.1 were published in Lenz et al. (2016). This publication was written entirely by me, minor editing was suggested by the co-authors and the journal language editor.

Chapter 6 gives a summary on this work and provides an outlook on the next steps with regards to the challenges of the observation of atmospheric emission of exoplanets.

Chapter 2

The Star-Planet Systems

2.1 HD 209458

HD 209458 is a sunlike star which hosts one of the best studied exoplanets. The planet, HD 209458 b is a hot Jupiter planet in a close orbit of roughly 3.5 days. It was discovered in 1999 with radial-velocity measurements and is the first ever transiting planet that was detected with transit photometry (Charbonneau et al., 2000; Henry et al., 2000). Various atoms and molecules have been identified in the spectra of the planets atmosphere, such as features of Na (sodium) (Charbonneau et al., 2002), H₂O (water) (Beaulieu et al., 2010), CO (carbon monoxide), CO₂ (carbon dioxide) and CH₄ (methane). Space-based observations of the system with the Hubble Space telescope led to the detection of escaping hydrogen from the planets atmosphere (Vidal-Madjar et al., 2003). There are quite a number of models that have been developed for global circulation (Showman et al., 2008) as well as for separate atmospheric layers, e.g. to analyze the upper atmosphere of the planet and the atmospheric evaporation (e.g. Bourrier and Lecavelier des Etangs, 2013). HD 209458 b is the only hot-Jupiter from the 2010 observational run for which the data quality was sufficient to analyze the spectra for signs of H₃⁺ emission. The advantage of a transiting planet for our analysis is the known position of the planet in the orbit. Hence, the radial velocity shift of the planet in the stellar spectrum can be determined. Also, the transit of the planet allows to obtain spectra of the system during secondary transit, where the

planet is not visible for the observer. Subtracting these ‘star-only’ data from the data where a signal from the planets atmosphere is expected, could in principle allow the detection of faint atmospheric signals of the planet. The system parameters for HD 209458 and the hot-Jupiter systems introduced in the following subsections are summarized in Tab. 2.1.

2.2 GJ 86

GJ 86 is a binary system consisting of a primary K-dwarf main sequence star (GJ 86 A), which has a white dwarf binary companion (GJ 86 B) at a separation of 21 AU. The primary companion (GJ 86 A) hosts a hot-Jupiter planet, GJ 86 b. The hot-Jupiter planet was discovered in 2000 with radial velocity measurements (Queloz et al., 2000) and is located close to its host star with a period of 15.766 days. GJ 86 is very close to Earth, which increases the detectability of possible planetary signals. Since there was no detection of H₃⁺ in hot Jupiter atmospheres reported at the time we decided on our observation targets (and still is no detection reported today), we aimed in our second observation run (2012) for star-planet systems that allowed for obtaining the best possible signal-to-noise observations with CRIRES.

2.3 HD 217107

HD 217107 is a late-type main-sequence star with the spectral type G8 IV. Hence, the star has a comparable radius, mass and effective

Table 2.1: Parameters of the hot-Jupiter systems. Note, that only for the transiting system, the mass of the planet is known. For the two radial velocity planets $M \sin i$ is given, accounting for the unknown inclination angle i .

Object	Spectral Type	Distance [pc]	M_{Star} [M_{\odot}]	M_{P} [M_{Jup}]	$M \sin i$ [M_{Jup}]	P_{orb} [d]
HD 209458 ^a	G0	47.1	1.01	0.685	-	3.5247
HD 217107 b ^b	G8 IV	19.72	1.02	-	1.33	7.12689
GJ 86 A b ^c	K1V	10.9	0.77		4.00	15.76491

^a Southworth (2010)

^b Wittenmyer et al. (2007)

^c Butler et al. (2006)

temperature as the Sun. Its orbiting hot-Jupiter planet HD 217107 b was detected by radial velocity measurements in 1999 (Fischer et al., 1999) and has an orbital period of 7.126 days. Vogt et al. (2005) reported the presence of another companion in a wide orbit with a period of > 8 yr. The orbital parameters of this second planet 'c' were characterized more precisely in the following years (Wittenmyer et al., 2007; Wright et al., 2009).

We chose this target in order to test the possible scenario that a close-in planet could have enhanced H_3^+ emission due to a increased particle flux from its host star. Another possible scenario would be that the increased flux would cause atmospheric evaporation and hence might suppress the occurrence of H_3^+ emission.

Chapter 3

Observations

3.1 The CRIRES Spectrograph

CRIRES (Cryogenic High-Resolution IR Echelle Spectrograph) at the Very Large Telescope (VLT) is a near-infrared (NIR) echelle spectrograph with a resolving power of up to $R = 100,000$ in a wavelength range between $1 - 5.3\mu\text{m}$. A detailed description of the instrument can be found in Kaeufl et al. (2004) and on the ESO website for the CRIRES spectrograph¹. Until the spectrograph was dismantled from the telescope for a major update in 2014 (see Sec. 5.3.1), CRIRES was located on the Nasmyth-A platform of UT1 (Antu).

Figure 3.1 shows the instrument vessel mounted on the platform beside the telescope structure which can be seen in the background. The pre-optics, consisting of the adaptive-optics (AO) system, the field de-rotator and the calibration unit, are not thermally controlled and mounted on the optical table before the entrance window of the vacuum vessel. The cool part of the instrument is maintained at 65 K for all optical parts besides the detector array, which is cooled down to 27 K .

The optical layout is shown in Fig. 3.2: the light from the telescope is sent through the de-rotator to counteract the field rotation introduced by the light which is exiting the Alt-Az mounted telescope through the Nasmyth focus. In the following, the light passes the AO system and the entrance window of the vacuum vessel. The entrance window is a dichroic, which separates the visible part of the light

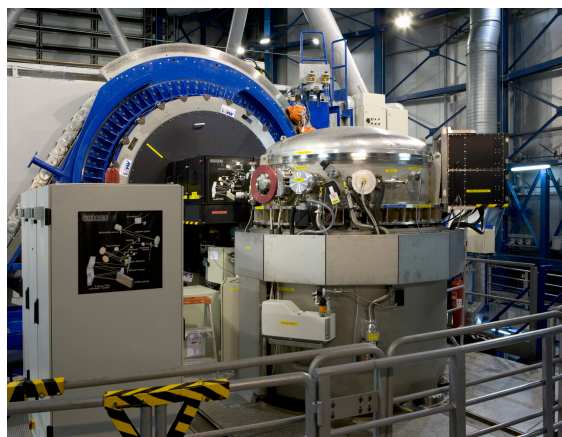


Figure 3.1: CRIRES on the Nasmyth platform in front of the telescope mounting structure of UT1. The vacuum vessel hosting the optical bench and the detector array is on the right side of the image. The framework of the 8 m telescope can be seen in the background. Image credit: ESO

and sends it to the AO system control. The infrared light is focussed onto the main slit, which can be chosen for $0.2''$ or $0.4''$ projected slit width, corresponding to nominal resolving powers of $R = 100,000$ and $R = 50,000$, respectively. The light not passing the slit is reflected and collected by the slit viewer. The pre-disperser part of the spectrograph isolates an echelle order using a ZnSe prism and in the following an intermediate slit. The light is then collimated before hitting the R2 echelle grating (31.6 gr/mm). Finally, the spectrum is imaged onto the detector array, formed by a

¹ <http://www.eso.org/sci/facilities/paranal/instruments/crides/>

mosaic of four Aladdin III InSb-arrays which provides an effective size of 4096x512 pixel in the focal plane. The mosaic arrangement of the detectors causes three gaps which have a size of 280 pixels.

3.2 Observing Runs

Our data was obtained in two observing runs with CRIRES at the VLT. For both runs the spectra were taken in the L'window, with the reference wavelength set to 4010 nm and a slit width of 0.2'' which translate to a resolving power of $R \approx 100,000$. The 4010 nm setting covers seven H_3^+ emission lines that were found in strong emission in the southern aurora of Jupiter (Maillard et al., 1990). An overview of the wavelength coverage, line positions and location on the detector array can be found in Tab. 3.1.

The observations of HD 209458 were carried out in October 2010 under ESO program ID 086.C-0045 in visitor mode. Unfortunately, this observing run was severely hit by bad weather. Thus, the observations yielded in only 16 spectra of HD 209458 in the 4010 nm setting and a total time on target of 2400 s. HD 209458 b is a transiting planet and twelve of the spectra were observed during secondary transit. The remaining four spectra were observed after secondary eclipse and thus contain the light of the planet. Each of these four spectra has a combined integration time of 150 s. These spectra are called combined-light spectra hereafter.

The second observing run was carried out in service mode in October and November 2012 under ESO program ID 090.C-0244. Two targets were observed, namely GJ 86 and HD 217107. Both objects were observed in two nights each. The total integration time on target was 10800 s for GJ 86 and 13500 s for HD 217107.

The signal-to-noise ratios of the spectra after data reduction and telluric correction is summarized in Tab. 3.2.

3.3 Preparation of the Raw Data

The data reduction described in this section was performed by myself. Andreas Seifahrt performed the telluric correction of the 2010 data, described in section 3.4.1. The atmospheric modeling described in section 3.4.2 with the `molecfit` code was carried out by myself.

Data Reduction

The observed data was reduced using the ESO instrument pipelines² for CRIRES with `esorex`³ and `gsgano`⁴. The CRIRES pipeline recipes used for the reduction were the most recent versions at the time the data was obtained, for the reduction of the 2010 data, version 2.1.1 was used and for the 2012 data version 2.3.2 was used. The data reduction followed the standard routines for echelle spectrographs, using the associated calibration sets that were recorded for each of the observing nights.

After correction against a master-dark frame, a non-linearity correction was applied to all raw frames. In the next step, the individual frames were divided by a normalized flatfield. Since no emission lamps for wavelength calibrations are available in the 4 μ m range of CRIRES, no wavelength solution was calculated during the data reduction with the CRIRES pipeline recipes. However, using the information on the positions of telluric absorption lines a wavelength calibration can be derived. Thus the wavelength correction was performed during the correction for atmospheric absorption features (see Sec. 3.4). The observations were carried out in a nodding pattern and the resulting A and B frames were treated separately for optimal extraction. The 2D-images were not combined before the extraction, in order to avoid a degradation of the resolution due to the curvature of the slit.

² <http://www.eso.org/sci/software/pipelines/>

³ <http://www.eso.org/sci/software/cpl/esorex.html>

⁴ <https://www.eso.org/sci/software/gsgano.html>

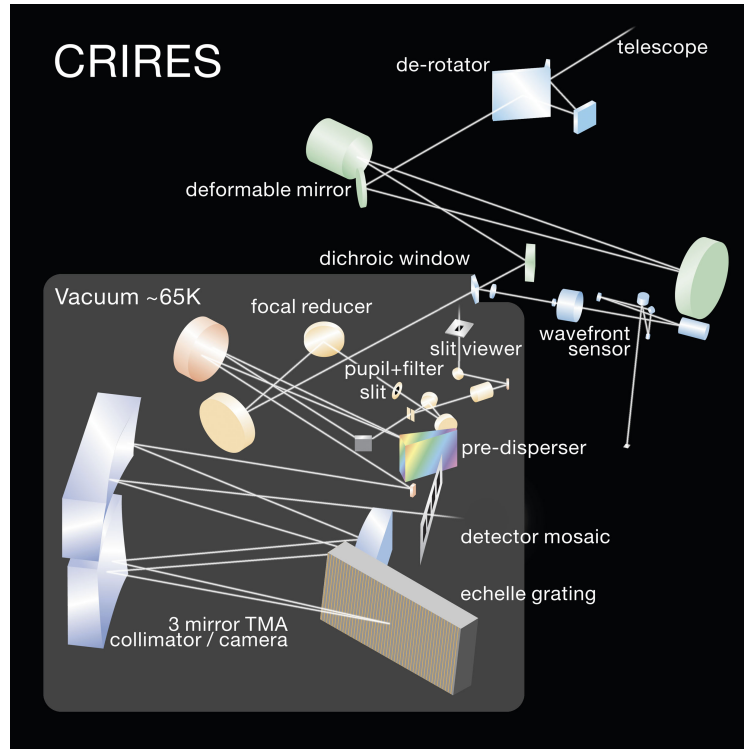


Figure 3.2: Optical layout of the CRIRES spectrograph from Kaeufl et al. (2004)

Table 3.1: CRIRES wavelength coverage of the observed spectra, emission line positions for H_3^+ and intensities from the southern Aurorae of Jupiter as given in Maillard et al. (1990).

Detector Number	Detector Start [nm]	Detector End [nm]	Line Position [nm]	Intensity (South. Aurora of Jupiter) [$\frac{\text{W}}{\text{cm}^2\text{sr}}$]
1	3947.3	3968.6	3953.0	42.8
2	3974.6	3995.1	3985.5	45.2
			3987.0	23.5
			3994.6	11.5
3	4000.6	4020.3	4012.0	19.3
			4013.3	17.3
4	4025.4	4044.3	4043.2	10.2

Table 3.2: Signal-to-noise ratios of the mean observed spectra after data reduction and telluric correction

Object	Integration Time s	Signal-to-Noise Ratio
HD 209458	600	142
HD 217107		
Night 1 (1st half)	5400	349
Night 1 (2nd half)	5400	305
Night 2	2700	446
GJ 86		
Night 1	3600	543
Night2	7200	836

3.4 Telluric Absorption Correction

The L'window is heavily polluted with telluric absorption lines, thus the spectra have to be corrected for the telluric contamination.

In the classical approach for telluric correction of stellar spectra, a so-called *telluric standard* star is observed in close succession to the actual target. Usually, these are early type stars with very few lines, observed with similar airmass and close in time to the objects observed for scientific purposes. Alternatively, a G-type star is observed and corrected for the stellar lines by high resolution spectra of the Sun. Both methods have a couple of disadvantages: first, they require additional observing time, which is very expensive. Second, depending on the scientific targets, a telluric standard star might not be available at close angular range. And also, the atmospheric conditions may change during observation, so that the telluric spectra do not reproduce the conditions at the beginning of the observation of the scientific targets. Additionally, in the infrared L (including L') and M windows, early-type stars or G-stars may be too dim to be used as telluric standards for a proper correction. For these spectral regions non-stellar sources like asteroids, if available, may be preferred (Seifahrt et al., 2010).

An alternative approach is using synthetic

telluric spectra for the removal of telluric absorption lines. These spectra are generated from radiative transfer codes for the atmosphere of the Earth. As one of the first attempts Bailey et al. (2007) used the SMART (Spectral Mapping Atmospheric Radiative Transfer) code from Meadows and Crisp (1996) and demonstrated the possibility of correcting telluric contamination with synthetic spectra of the atmosphere of the Earth.

Seifahrt et al. (2010) applied the Line-By-Line Radiative Transfer Model Code (LBLRTM)⁵ to CRIRES spectra and report an accuracy of up to 2% for reproducing the observed spectra. The LBLRTM Code was also used by Husser and Ulbrich (2014), who applied the code to broadband XSHOOTER spectra (Vernet et al., 2011) and perform a full-spectrum fit in order to apply model spectra to their science observations. Smette et al. (2015) developed *molecfit*, a tool for the correction of telluric absorption features using synthetic models for the computation of the atmospheric transmission and applicable to all kinds of astronomical spectra in terms of wavelength range (from the optical to the infrared regime) and spectral resolution. *Molecfit* was developed in the Austrian ESO In-Kind project SM-03. The *molecfit* package is available via the ESO website and applicable to all kinds of observed spectra in terms of wavelength range and resolution.

⁵ http://rtweb.aer.com/lblrtm_description.html

3.4.1 Telluric Correction for the Spectra of HD 209458

The spectra of HD 209458, observed in 2010, were corrected for the telluric absorption lines using the LBLRTM code with the techniques described in Seifahrt et al. (2010).

First, a synthetic telluric transmission spectrum is computed, using the LBLRTM code for the radiative transfer calculations and an archived Global Data Assimilation System (GDAS) model atmosphere, that is selected to be as close in time to the observation as possible. The LBLRTM code makes use of the model atmosphere, the altitude angle of the telescope pointing and the height of the atmosphere to calculate a line-by-line and layer-by-layer transmission and radiance model. The resulting spectrum is refined by a χ^2 -minimization fitting routine regarding the total water vapor amount and the column densities of the molecules present in the spectral range. Also, the instrumental profile is determined by the χ^2 fitting. This is required for properly fitting atmospheric lines, that are only partially resolved. The χ^2 -minimization fitting routine also provides a calibration of the wavelength grid. Since CRIRES has no internal calibration source for L'-Band observations, we use the atmospheric lines for the determination of the wavelength solution.

Figure 3.3 shows an example spectrum (black) of HD 209458 with its corresponding telluric correction (green) for each of the four detectors. The three panels from top to bottom show the CRIRES spectrum and the synthetic absorption spectrum, the observed-corrected (O-C) and the observed/corrected (O/C) residuals of the fit. The spectra are corrected for telluric absorption by dividing the observed spectrum by its corresponding telluric model spectrum.

3.4.2 Correction of Telluric Spectral Features with `molecfit`

For the data from the observation run in fall 2012, we use `molecfit` for the atmospheric correction. `molecfit` is a tool provided by ESO

which was developed by a team of astronomers from Innsbruck as an ESO In-Kind contribution (Smette et al., 2015). The tool is capable of fitting telluric spectral features in astronomical spectra and deriving correction functions for these features. It was developed with the goal to provide a telluric correction tool for ESO spectrographs in the optical and near-infrared.

The `molecfit` tool uses LBLRTM as an radiative transfer code and GDAS atmospheric profiles as input. Two GDAS models are chosen to bracket date and time of the observation. The GDAS profile is then matched in time and date to the observation using linear interpolation. The interpolated GDAS model is merged with a standard profile and local meteorological data and, together with a molecular database, used as input for the radiative transfer code. `molecfit` comprises an automatized fitting routine for adjusting the wavelength solution, the continuum spectrum, spectral resolution and column densities of the molecules used for the radiative transfer code.

Each spectrum was fitted separately, after excluding the intrinsic defects of the detectors from the fitting region. A detailed description for the fitting process of `molecfit` can be found e.g. in Smette et al. (2015). The fitting process with `molecfit` is performed in two steps. First, `molecfit` is applied to the spectra for fitting the molecular transmission and emission. Second, `calctrans` is used for the correction of the telluric absorption in the spectra. In total, 360 spectra of GJ 86 and 450 spectra of HD 217107 were fitted and corrected with `molecfit`.

An example for the atmospheric correction using `molecfit` is shown in Fig. 3.4. The graph shows one of the GJ 86 spectra (black) with its corresponding telluric spectrum (green). As in Fig. 3.3 the lower panels show the O-C and O/C residuals. For further analysis the observed spectra are divide by their corresponding telluric models.

As discussed in Lenz et al. (2016) we do not expect systematic effects from the telluric modeling for the CRIRES spectra, besides the

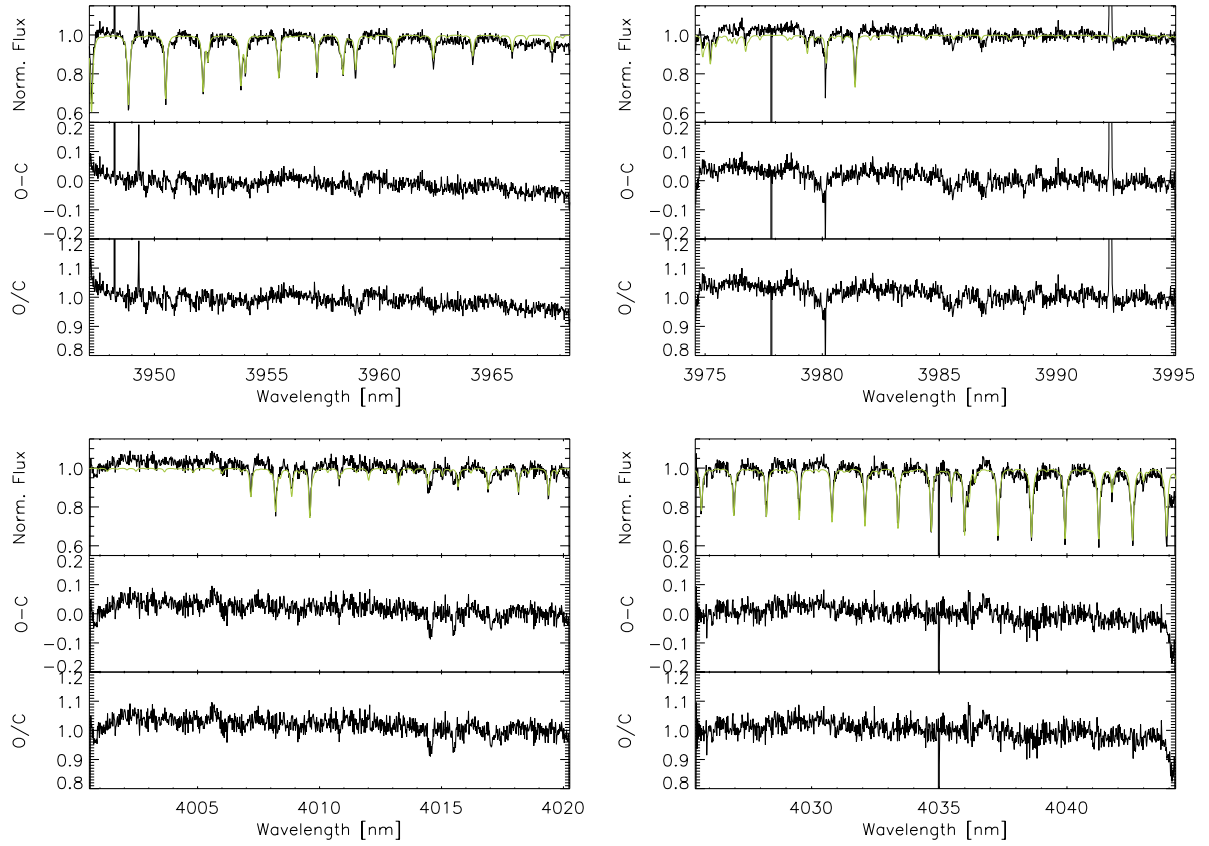


Figure 3.3: LBLRTM atmospheric modeling results for one spectrum of HD 209458 for all four CRIRES detectors. Upper panels: CRIRES spectrum (black) with its corresponding telluric model spectrum (green). Lower panels: Observed-Computed (O-C) and Observed/Computed (O/C) residuals. The O/C residual spectra were used in the analysis.

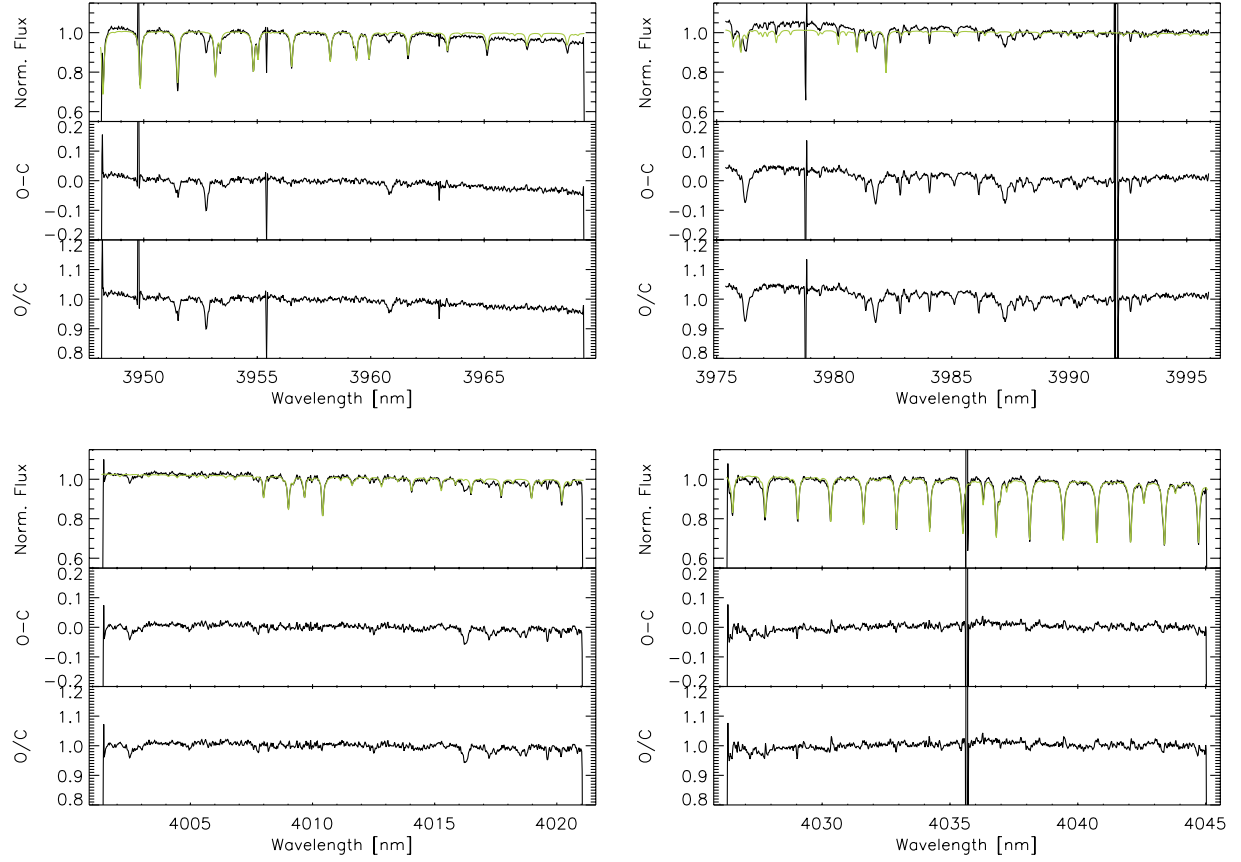


Figure 3.4: GJ 86: atmospheric modeling results for the correction of telluric absorption with *molecfit*. The figure shows one of the GJ 86 spectra for all four CRIRES detectors. Upper panels: CRIRES spectrum (black) with the corresponding telluric model spectrum (green). Lower panels: Observed-Computed (O-C) and Observed/Computed (O/C) residuals. The O/C residual spectra were used in the analysis.

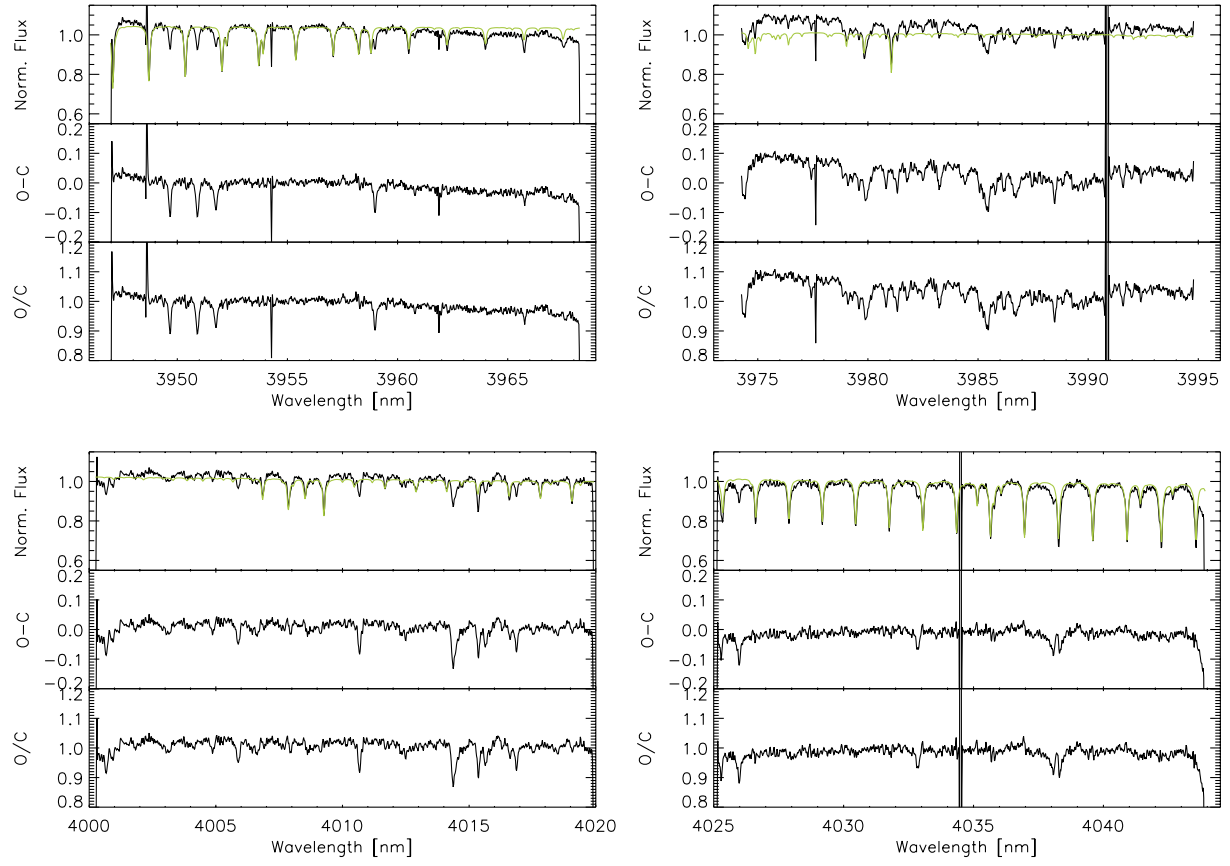


Figure 3.5: HD 217107: atmospheric modeling results for the correction of telluric absorption with `molecfit`. For detailed description see Fig. 3.4

1 – 3% flux from in-dispersion straylight for absorption line cores for regions with fully saturated telluric features (Lebzelter et al., 2012). However, this effect cannot be corrected for pointlike sources like stars.

After reduction of the spectra, the continuum levels vary for the different detectors. The reduction includes the standard flatfielding routines for CRIRES provided by ESO and we assume this trend in the continuum to originate from the reduction of the flatfields. For our analysis, all detectors are analyzed separately in order to account for the gaps in between the detectors which contain spectral information that cannot be recovered. For the telluric and wavelength corrected spectra, we calculate the topocentric velocities and correct our spectra accordingly. This correction is derived from the information on the location of the observatory, the stellar coordinates and the time of observation.

Chapter 4

Data Analysis

This chapter describes the analysis of the observed star-planet systems HD 209458, GJ 86 and HD 217107, obtained 2010 and 2012 with the CRIRES spectrograph at the VLT. Subsections 4.1.2 to 4.1.4 are published in *Astronomy & Astrophysics* as ‘A CRIRES-search for H_3^+ emission from the hot Jupiter atmosphere of HD 209458 b’ (Lenz et al., 2016) as Section 3., ‘Search for H_3^+ emission’. I performed all parts of the analysis of this data.

Section 4.2 describes the analysis of the data of GJ 86 and HD 217107, observed in 2012.

4.1 Analysis of the CRIRES Spectra of HD 209458

4.1.1 Radial Velocities of HD 209458 b

As described in Sec. 3.2 only a small part of the planned observing run in 2010 with CRIRES could be realized due to unfavourable weather conditions. However, we could successfully obtain 16 spectra of HD 209458. Using the ephemeris from Knutson et al. (2007) we derive the radial velocity values for each of the observed spectra. In Fig. 4.1 the radial velocity curve of HD 209458 b is shown, the time span of the observation is highlighted in purple. From the transit duration measured by Beaulieu et al. (2010) the end of the secondary eclipse is calculated. From the 16 observed spectra, 12 were taken during secondary eclipse and four spectra contain the combined light of the star and its orbiting planet. The inset in Fig. 4.1 shows the separate observations with the vertical line

highlighting the end of the secondary eclipse. The given error for the ephemeris by Knutson et al. (2007) has negligible influence on the radial velocity results in comparison to the uncertainties of the ephemeris itself: we tested the slightly varying ephemeris values that were published e.g. by Wittenmyer et al. (2005) against the results using the ephemeris derived by Knutson et al. (2007). Using the value from Wittenmyer et al. (2005) changes the number of spectra outside the secondary eclipse from four to five. However, we choose using the more recent ephemeris given by Knutson et al. (2007) with its corresponding transit duration derived by Beaulieu et al. (2010).

4.1.2 Direct Search

We start searching for H_3^+ emission peaks in each of the combined light spectra separately, considering the radial velocity shift of the planet with respect to its host star. We expect that an emission peak would most probably occur in all combined light spectra, since they were observed within minutes of each other. Since HD 209458 b is tidally locked, emission lines from its atmospheres would be very narrow. In the direct search in all four combined light spectra, we cannot detect any signatures of H_3^+ emission lines.

4.1.3 Cross-correlation Approach

Our second approach to the search for emission features of the planetary atmosphere is to cross-correlate the combined light spectra

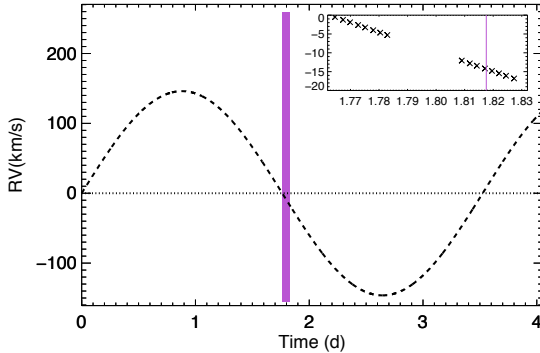


Figure 4.1: HD 209458: radial velocities (km/s) over time in days. The time span of the observations is marked by the purple shaded area in the large plot. In the inset, the crosses indicate the separate observations. The vertical line highlights the end of the secondary eclipse, calculated from the ephemeris value from Knutson et al. (2007). All spectra left of the vertical line were recorded during secondary eclipse. Hence, four spectra contain the combined light of the star and its orbiting planet.

pairwise. Emission lines of the planet would show the differential planetary radial velocity in the cross-correlation. Thus, a detection in a cross-correlation would be independent of the accuracy of the knowledge of the H_3^+ emission line positions. The detectors are treated separately because of the gaps between the detectors. Also, a ~ 0.06 nm chunk is cut from both ends of each spectrum to avoid signals from nonlinearity effects at the edges of the spectra. As a preparation for the cross-correlation test, all spectra from detector No. 2 are prepared in the following way: The crack and the right end of the detector is removed. Strong spikes in all spectra are removed and replaced by a median smoothed spectrum.

We apply the cross-correlation to the following combinations of spectra: First, we use the telluric-corrected spectra for the cross-correlation. In the second step, we subtract the host star from the spectra, by computing a mean spectrum of the 12 secondary eclipse spectra and subtract the result from each combined light spectrum before performing the cross-correlations. In the third step, we subtract a single secondary eclipse spectrum instead of the mean eclipse spectrum. This single spectrum has a lower signal-to-noise ratio, but since the timespan between the last observed secondary eclipse spectrum and the combined light spectra is very short, parts of the atmospheric distortions that have not been corrected by the telluric modeling vanish with the subtraction. However, if the ephemeris is not precise one might also subtract a viable signal from the planet. We choose the secondary eclipse spectrum that was observed directly before the end of the secondary eclipse. As a consistency check, we repeat this procedure using the spectrum that was observed second to last during secondary eclipse.

A planetary signal in the spectra is expected to cause a signal in the cross-correlation with the differential planetary radial velocity of the two spectra that are used as input spectra in the cross-correlation. Since the spectra were recorded in close succession shortly after the secondary eclipse, the differential planetary radial velocity values are only up to 2 km s^{-1} . Also, the stellar and telluric lines, as well as detector artifacts, cause a peak around 0 km s^{-1} .

The cross-correlation results for the pure spectra and the spectra with subtracted mean eclipse spectra show various peaks over the whole radial velocity range. The results for the spectra with subtracted last eclipse spectrum show a clear signal around 0 km s^{-1} as well as the results for the consistency check for which another eclipse spectrum is subtracted before the cross-correlation is applied. We continue the analysis with the spectra from which we subtracted the last spectrum that was observed during secondary eclipse.

We fit the main peak of each cross-correlation with a Gaussian and derive the radial velocity from the maximum of the fit. We expect a planetary signal in the cross-correlation to shift the Gaussian fit sideways. The fitted velocity would thus lie between 0 km s^{-1} and the differential radial velocity in case of a detection. In Fig. 4.2 the results of the cross-correlation are presented for all four detectors. The x-axis gives the number of spectra used for the cross-correlations (e.g., 1x2 means the cross-correlation of the 1st and 2nd observed combined light spectra). The squares show the differential planetary radial velocities of the pair of spectra and the crosses give the fitted radial velocity values from the cross-correlations. In case of a detection of planetary emission, we expect the radial velocity values of the fit (squares) to follow the pattern of the differential radial velocity values (crosses) in the plot. We expect a planetary signal to occur in all observed spectra, since they were recorded in close succession.

We cannot find cross-correlation signals that follow the expected pattern of the planetary radial velocity. Fitting the cross-correlation results give signals that scatter around 0 km s^{-1} . The same result follows for the consistency test in which another secondary eclipse spectrum is subtracted from the combined light spectra. We also check all cross-correlation results by eye for peaks and do not detect any signal that indicates planetary emission.

4.1.4 Search for Emission with Shift and Add

The known ephemeris also enables us to use a shift and add approach to search for H_3^+ emission: all observed combined light spectra are shifted in wavelength with respect to their apparent radial velocity of the planet at the time of observation. Afterwards, the flux is summed up binwise. With this technique the stellar lines and residuals from the telluric correction get blurred and a planetary emission line that is hidden in the stellar flux would emerge in the

summation of the shifted spectra, given that the ephemeris and consequent radial velocity values are correct.

The resulting shift and add frame is shown in Fig. 4.3. The H_3^+ emission line positions from Maillard et al. (1990) are highlighted by the dashed lines. Insufficient correction of telluric lines by the modeling and the application of the shift and add technique cause artificial, broad absorption lines in the resulting frames. Since we do not apply any correction for the crack on detector No. 2 for this part of the analysis, the crack is still visible as a large peak around 3991 nm in the resulting spectrum. In the results from the shift and add procedure, we cannot detect any signs of emission peaks at the expected H_3^+ emission line positions.

As a last test for the shift and add results, we create an artificial spectrum; this artificial spectrum contains only Gaussians at the positions of the H_3^+ line positions from Maillard et al. (1990) and a line width calculated from the thermal width of 0.052 nm folded with the instrumental profile and line strengths of 3σ , which we measure in the resulting shift and add frame at the position of the emission line at 3953.0 nm. We perform a cross-correlation of this artificial spectrum with the resulting shift and add frame as a final test for hidden planetary emission signals for each detector separately. The cross-correlations do not show a significant peak.

We also search the spectra for a drop of the total flux during secondary eclipse, but cannot identify any variances in the integrated flux that would indicate the end of the secondary eclipse. Variations of the flux due to atmospheric distortions are too large to allow for the measurement of the $\sim 0.1\%$ secondary eclipse depth (Diamond-Lowe et al., 2014).

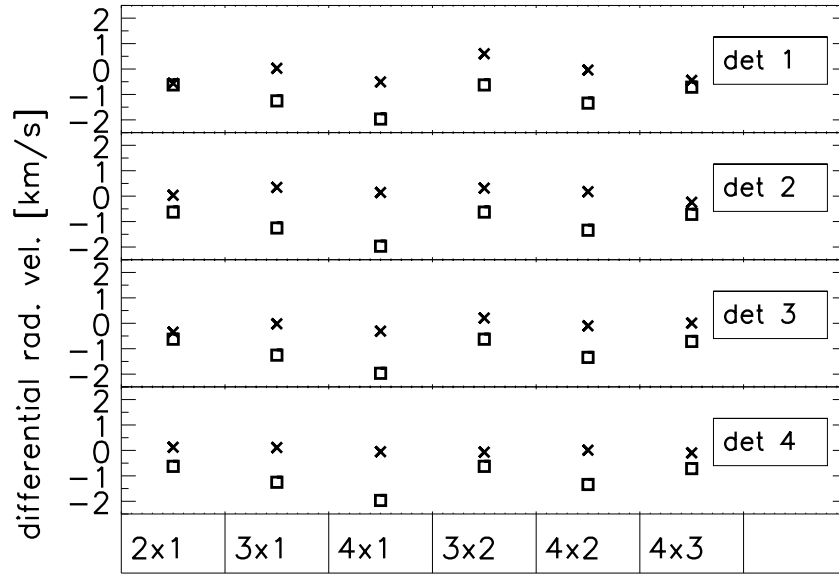


Figure 4.2: Cross-correlation results. Upper to lower panels show the four CRRES detectors. The spectrum that was observed last during secondary eclipse is subtracted from each combined light spectrum. The resulting spectra are cross-correlated and the main peak is fitted with a Gaussian. We derive the radial velocity value from the maximum of the fit and expect a planetary signal to shift the Gaussian fit sideways, producing a signal between 0 km s^{-1} and the differential radial velocity in case of a detection. The squares indicate the calculated differential radial velocity values from the time of observation and ephemeris and the crosses show the measured radial velocity from the cross-correlation. The error bars lie within the symbol size. Image credit: Lenz, A&A, 589, A99, 2016, reproduced with permission ©ESO

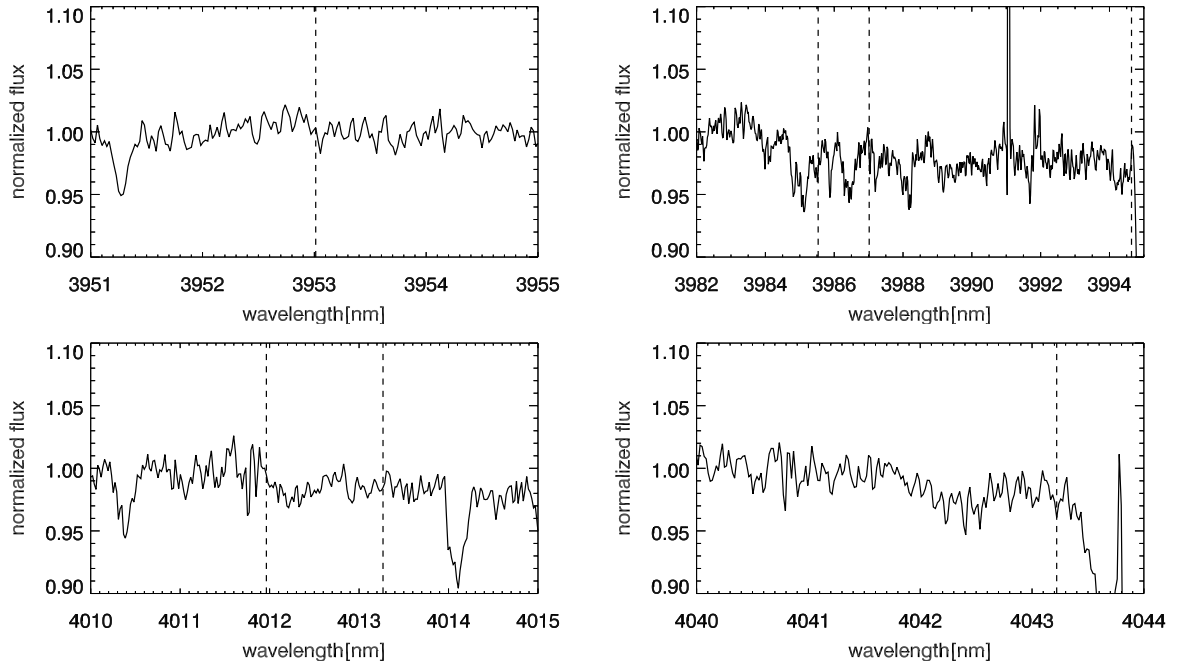


Figure 4.3: Spectra of HD 209458, a zoom-in for all four detectors is shown. All observed combined light spectra, were shifted to their apparent radial velocity at the time of observation and then added up binwise. The dashed lines indicate the positions where the H_3^+ emission lines are expected. Image credit: Lenz, A&A, 589, A99, 2016, reproduced with permission ©ESO

4.2 Analysis of the spectra of HD 217107 and GJ 86 for H_3^+ Emission Features

4.2.1 Radial-velocity Detected Planets and Possible Inclination Values

The hot Jupiter planets HD 217107 b and GJ 86 b are both non-transiting. Hence, for both planets the inclination angle i is unknown. The orbital plane of a star-planet system typically will be inclined to the observer, thus the radial velocity values that can be measured and all parameters derived from the radial velocities are modulated by the inclination angle i . A small inclination i leads to a smaller radial velocity value, than a larger inclination value. As shown by Fischer et al. (2014), the probability for i being in a range between $i_1 < i < i_2$ is

$$P_{inc} = |\cos i_2 - \cos i_1|. \quad (4.1)$$

From this equation, the probability for the inclination i to be in the range between 30 and 90 degrees is calculated to be 87%.

In order to get an estimate on the planetary radial velocity at the time of our observations, we calculate the radial velocity curves for a set of different inclination values. Figure 4.4 and Fig. 4.5 show the planetary radial velocity curves for a range of $30 \leq i \leq 90$ degrees in 10 degree steps for the planets HD 217107 b and GJ 86 b, respectively. The smaller the inclination i , the smaller the radial velocity amplitude. The curve with the largest amplitude is calculated with $i = 90$ degrees, which would be a transiting system. It is added nevertheless, in order to illustrate that for larger i the relative RV amplitude changes less as a function of i , compared to small inclinations. The curves start with the planet in front of the star, ‘mid-transit’, if i was 90 degrees. For both star-planet systems the x-axis is extended to show a bit more than one orbit of the planet.

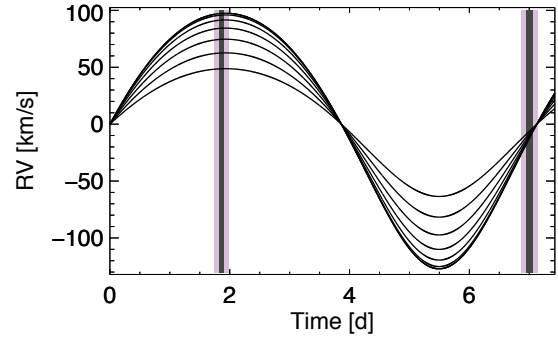


Figure 4.4: HD 217107: radial velocity of planet b for $i = \{30; 40; 50; 60; 70; 89; 90\}$ degrees. The vertical bars indicate the time of the observations translated to the phase in the orbit (grey) and the corresponding errors (light pink).

The grey columns in Fig. 4.4 and Fig. 4.5 illustrate the time of observation, translated into the observation phase and the light pink areas highlight the uncertainties on the phase points of the observations, following from the uncertainties of the periods and ephemeris. The system parameters for the calculation of the radial velocity curves are listed in Table 4.1.

Both star-planet systems were observed in two nights, thus Figures 4.4 and 4.5, show two phases (grey area) where observations were carried out. For HD 217107 (Fig. 4.4) the first

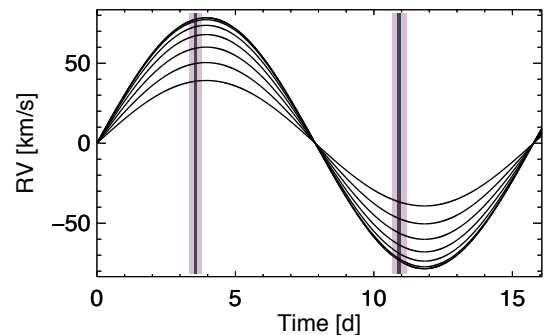


Figure 4.5: Radial velocity curves for GJ 86 b, see caption of Fig. 4.4 for a detailed description.

Table 4.1: Parameters for the Calculation of the Planetary Radial Velocities

	HD 217107 b ^a	GJ 86 A b ^b
$M \sin i$ [M_{Jup}]	1.33(± 0.05)	4.00(± 0.137)
P_{orb} [d]	7.12689 ($\pm 5e-05$)	15.76491(± 0.00039)
a [AU]	0.073 (± 0.001)	0.1142(± 0.0019)
eccentricity	0.132(± 0.005)	0.0416(± 0.0072)
ω [degree]	22.7(± 2.0)	269(± 16)
T_{peri} [JD]	2449998.50(± 0.04)	2451903.36(± 0.46)
M_{star} [M_{Sun}]	1.02	0.796(+0.025/ - 0.012) ^c

^a Wittenmyer et al. (2007)

^b Butler et al. (2006)

^c Takeda et al. (2007)

of the observing nights (in absolute time, not folded onto phase) falls onto the end of the orbit which translates into an absolute planetary radial velocity range of ~ 10 km/s. Night 2 falls onto a phase with a large range of possible radial velocity values of 45 – 95 km/s, depending on the actual inclination. Both observation nights of GJ 86 fall onto a large range of possible radial velocity values of $\sim 30 - 75$ km/s depending on the inclination.

4.2.2 Intranight Radial Velocities Shifts of the Planets Versus H_3^+ Line Width

Before summarizing the observed spectra into nightly mean spectra in order to search for (possibly weak) H_3^+ signals, the intranight planetary radial velocity shift has to be compared to the estimated line width. We calculate the full width at half maximum (FWHM) of a H_3^+ line (e.g. the emission line at 3953.0 nm) from the thermal width of the line folded with the instrumental profile of the CRIRES spectra, derived from the measurement of the telluric lines, to be 5.7 km/s. We use a formation temperature of 1000K as a rough estimate for the temperature in the lower thermosphere of a hot Jupiter planet.

For each observation night we then calculate the planetary radial velocity shift between the first and the last spectrum observed. We show this planetary intranight radial velocity

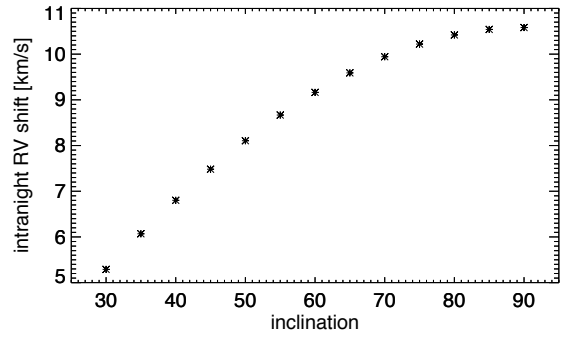


Figure 4.6: HD 217107 b: maximum of the intranight radial velocity shift over inclination for night 1.

shift over inclination in Fig. 4.6 and Fig. 4.7:

The first night of observations falls onto a phase with large differential radial velocity shifts. The maximum difference in radial velocity to the first observed spectrum of that night is 5 – 10 km/s depending on the inclination. The second observation night, in contrast, has a maximal intranight rv shift of only 0.3 km/s. The intranight shift in night 1 could be up to almost two times the estimated H_3^+ line width if HD 217107 b was highly inclined. Summarizing the spectra into a mean spectrum, in order to enhance possibly weak emission lines could therefore lead to broad emission bulges instead of a narrow line. The latter would be preferred for better detectability. Hence, we split the observed night into two parts and calculate a

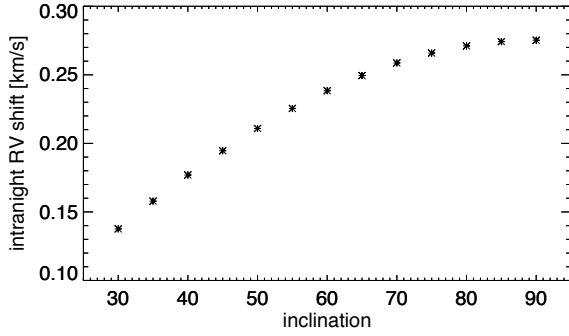


Figure 4.7: HD 217107 b: maximum of the intranight radial velocity shift over inclination for night 2.

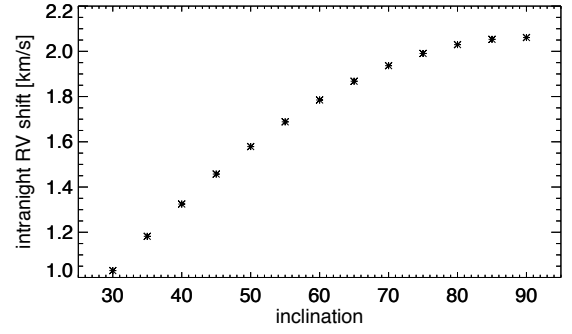


Figure 4.9: GJ 86 b: maximum intranight radial velocity shift over inclination for night 2.

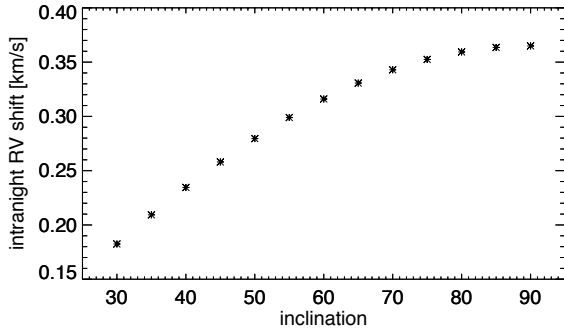


Figure 4.8: GJ 86 b: maximum intranight radial velocity shift over inclination for night 1.

mean spectrum for each half night for further analysis. These two half nights then both have maximum intranight radial velocity shifts of up to 5.3 km/s, depending on the inclination.

For GJ 86 b, the planetary radial velocity within both observing nights is at maximum 2 km/s, which is less than the estimate for the H_3^+ line width (see Fig. 4.8 and Fig. 4.9). Thus, the spectra from both nights can be summarized into one nightly mean spectrum for each night for the search for H_3^+ emission.

4.2.3 Residual Telluric Features

The correction of telluric features with `molecfit` is only precise to a certain level: Some linecores are not fully represented by the model.

If there were larger residual telluric lines in the corrected spectra, these could cause unwanted signals during cross-correlation analysis. Figures 4.10 and 4.11 show a comprehensive overview for the observed star-planet systems HD 217107 and GJ 86: the panels show the four CRRES detectors and the following spectra in each panel from top to bottom: the mean telluric model (blue), one single observed spectrum before any corrections for cosmics or bad pixels (green), the mean spectrum after telluric correction from one observing night (black) and a single spectrum with telluric correction applied (red). The flux is normalized to 1 for all spectra and then shifted up and downwards for better visibility of the different spectra. The mean corrected spectrum in black shows very small residual variations that can be assigned to non-perfect fitting of telluric line cores in the individual spectra. Also, as mentioned at the end of Chapter 3, CRRES spectra taken in regions with fully saturated telluric absorption lines suffer from 1-3% in-dispersion straylight, which we cannot correct for.

The remaining absorption lines in the mean spectra are stellar lines. Note, that detector No. 2 of CRRES has a crack in the right part of the detector that is visible around 3991.0 nm in our obtained spectra. This part of the spectrum has to be treated with caution in further analysis, e.g. it has to be masked out in order to perform a cross correlation analysis.

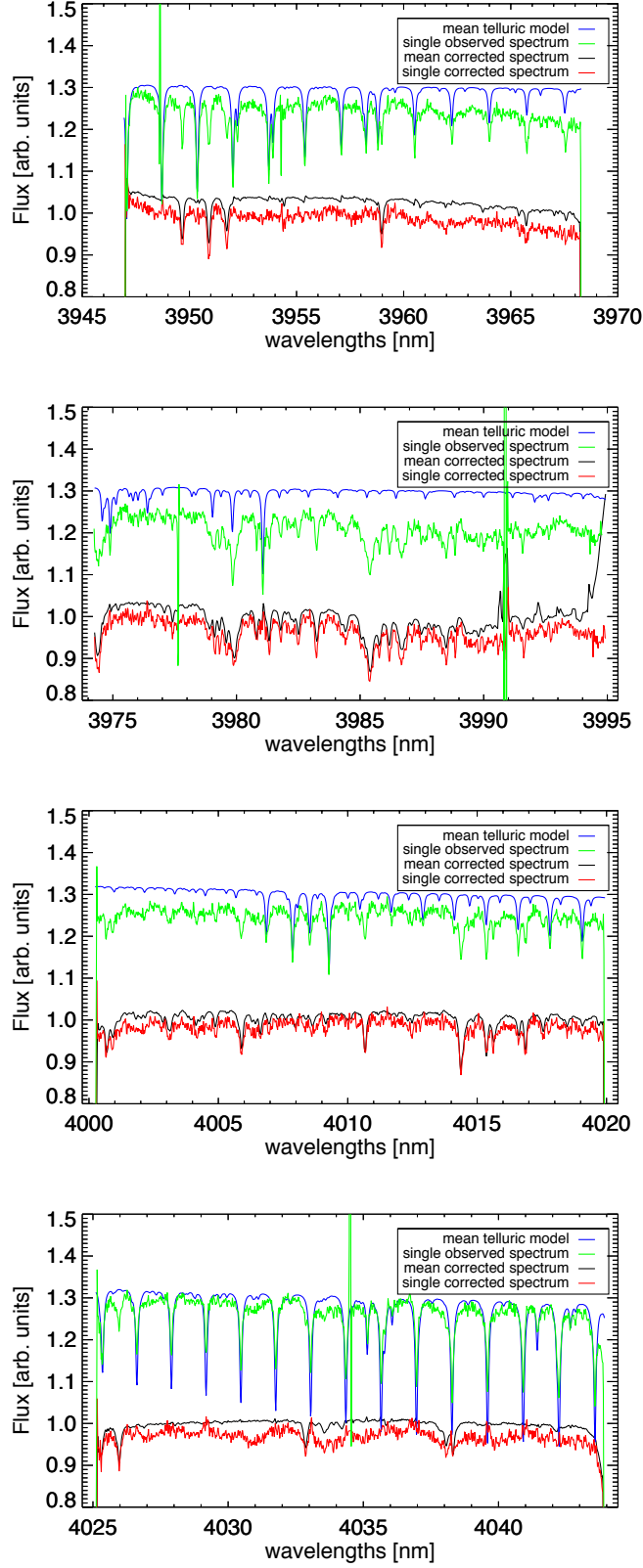


Figure 4.10: HD 217107: Overview of the telluric correction results. Top to bottom are all four CRRES detectors. Mean telluric model (blue), one single observed spectrum (green), the mean spectrum after telluric correction (black), a single spectrum after telluric correction (red). All spectra were shifted to the same topocentric velocity frame and shifted on the y-axis for better visibility.

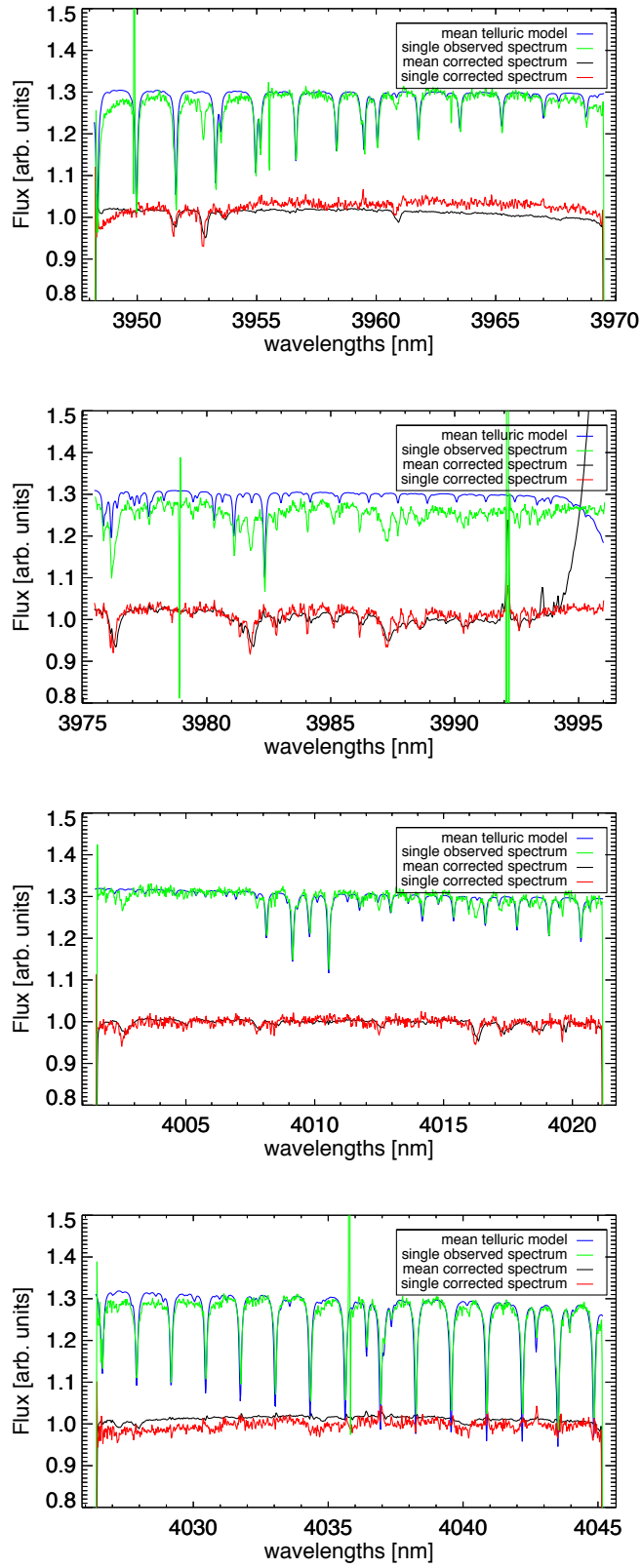


Figure 4.11: Same as Fig. 4.10 , but for GJ 86

4.2.4 Direct Search for H_3^+ in the Spectra of HD 217107 and GJ 86

From the analysis of the possible planetary radial velocities of our data (see Sec. 4.2.1) we derived the constraints on the possible line positions of H_3^+ emission. Due to the unknown inclination of the non-transiting systems it is not possible to calculate the precise positions of the shifted lines but only a region, where the lines would occur if H_3^+ emission is detected.

For the computation of the nightly mean spectra, we made sure that the intranight shift in all mean spectra is at maximum as high as the H_3^+ line width estimation (see Sec. 4.2.2). In consequence, the first observing night of HD 217107 is split into two parts and we compute one nightly mean spectrum for the first half night and another for the second half. Since both planetary systems are assumed to be tidally locked we can expect emission lines to occur as narrow lines and not to be broadened by planetary rotation.

We chose to search for the five emission lines with the highest intensity in the theoretical emission spectrum (see Fig. 1.6) and the emission measurements in Jupiter's aurora from Maillard et al. (1990). These are the line at 3953.0 nm ($Q\{1,0\}$) on detector No. 1 and the lines at 3985.0 nm ($Q\{3,0\}$) and 3987.0 nm ($Q\{3,1\}$) on detector No. 2, as well as the lines at 4012.0 nm ($Q\{4,1\}$) and 4013.0 nm ($Q\{4,2\}$) on detector No. 3. Figure 4.12 shows the combined spectra of the first half night of observations for HD 217107 for the detectors No. 1, No. 2 and No. 3, from top to bottom. On detector No. 4 the expected line positions do not fall onto the wavelength range of the detector. The combined spectrum is shown in black as a normalized spectrum, the red marker indicates the estimated FWHM of the H_3^+ line and is located at the rest wavelength at 3953.0 nm. The blue marker shows the shift range where the line could emerge due to the planetary radial velocity.

The same is shown in Fig. 4.13 for the second half of observing night 1 and for night 2

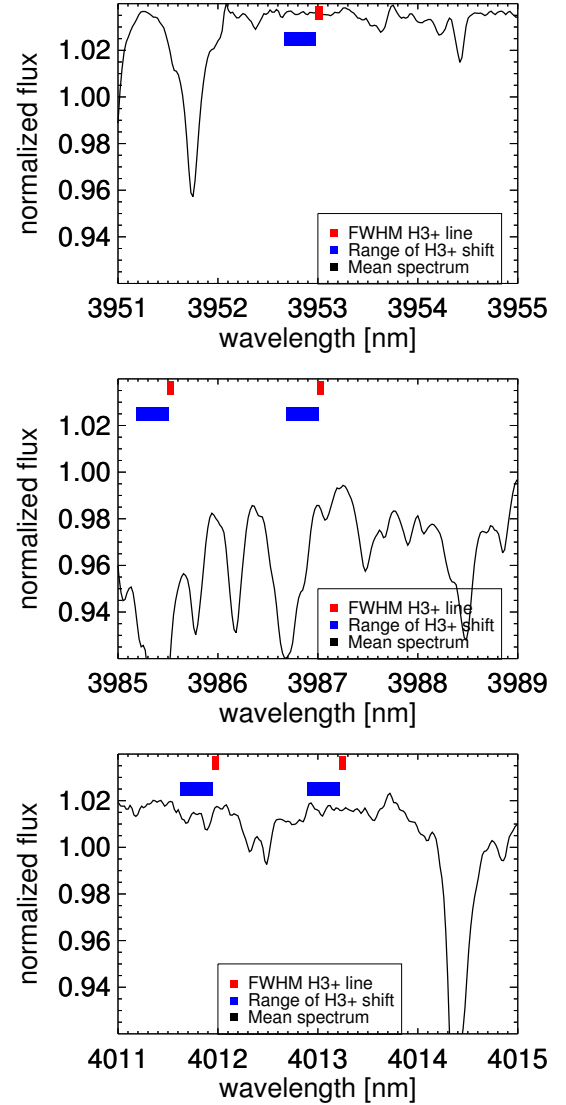


Figure 4.12: Top to bottom: CRIRES detector No. 1, No. 2 and No. 3. The panels show the mean spectrum of HD 217107 (black), computed from the first half night of observations from night 1 (night 1a). The estimate of the FWHM for the H_3^+ emission lines is shown in red at the rest wavelength positions. The range of the line shift due to the planetary radial velocity is represented by the blue markers.

in Fig. 4.14.

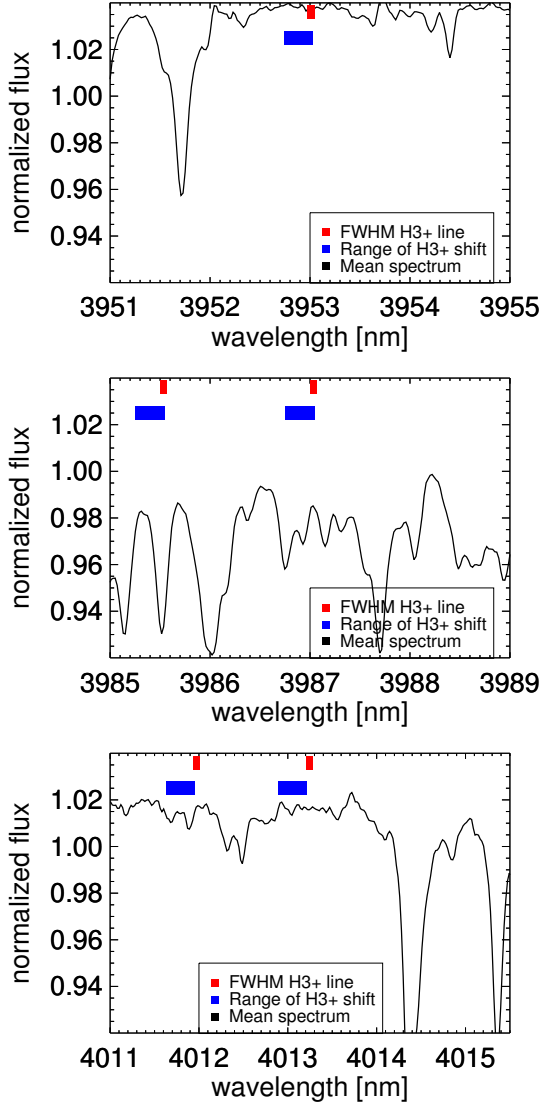


Figure 4.13: HD 217107: same as Fig. 4.12 but for the second half night of observations (night 1b).

Figures 4.15 and 4.16 show the same as Fig. 4.12 but for the observations of GJ 86. For Fig. 4.16, the x-axis was shifted 1 nm towards smaller wavelengths compared to the other plots, since the expected line shift is quite extreme towards smaller wavelengths for this observation. As for HD 217107, detector No. 4 is not used for the analysis, since the expected line positions do not fall onto the wavelength range of the detector. The signal-to-noise ratios

of the observations are listed in Tab. 3.2.

We cannot detect signs of H_3^+ emission in the spectra of both objects in those regions where the H_3^+ lines would be expected due to the planetary radial velocity shift.

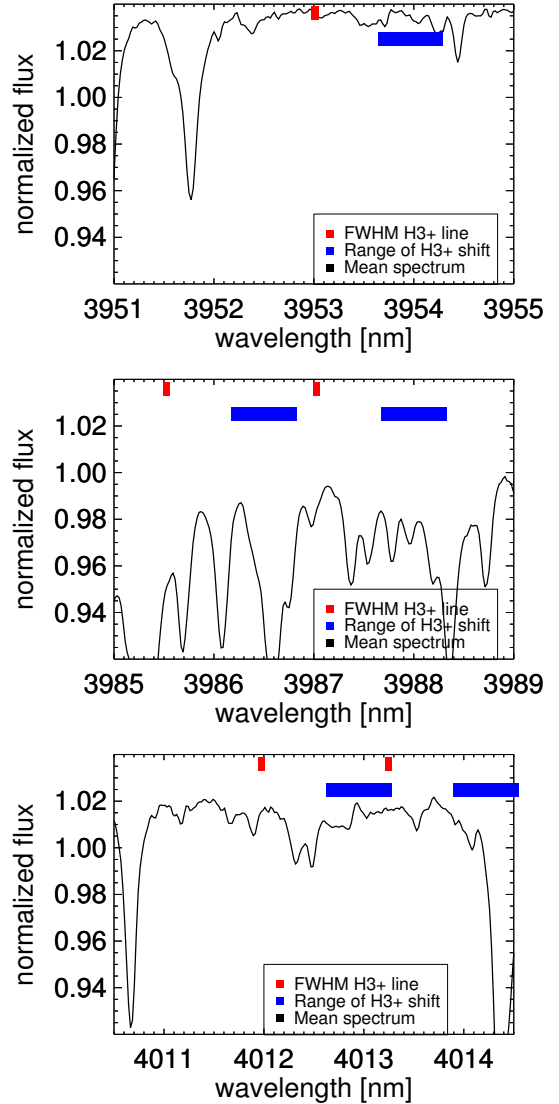


Figure 4.14: HD 217107: same as Fig. 4.12 but for observing night 2.

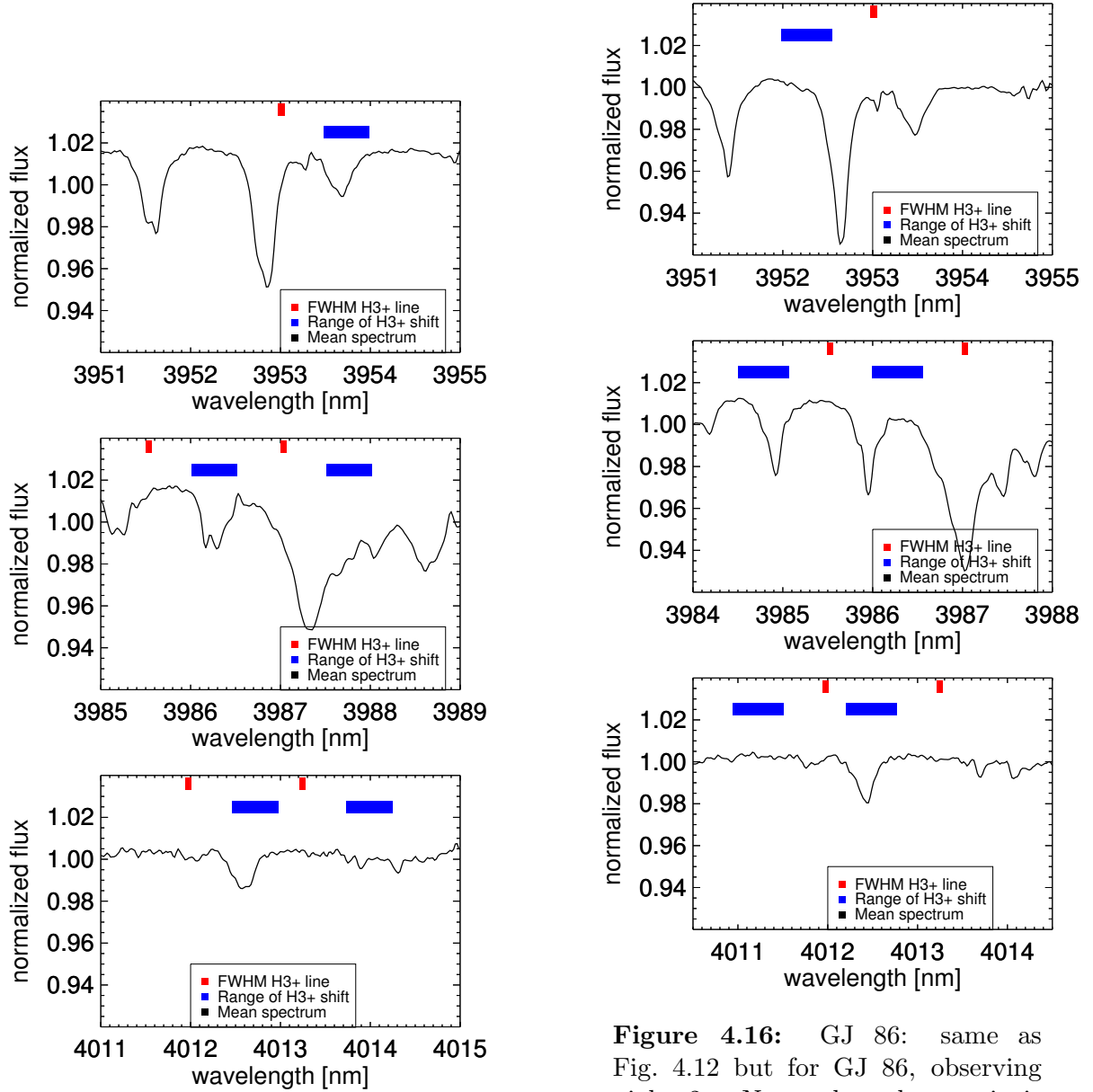


Figure 4.15: Same as Fig. 4.12 but for GJ 86, observing night 1.

Figure 4.16: GJ 86: same as Fig. 4.12 but for GJ 86, observing night 2. Note, that the x-axis is shifted 1 nm towards smaller wavelengths, compared to the other figures for better visibility of the wavelength regime where H_3^+ emission lines are expected due to the rv shift.

4.2.5 A Cross-Correlation Approach for the Search for H_3^+ Emission

Similar to Sec. 4.1.3, we use a cross-correlation approach to search for H_3^+ emission lines from the hot Jupiter planets in the spectra. In principle, the application of cross-correlation techniques for the search for planetary atmospheric emission could detect emission lines which are buried in the noise of the spectra. Since a cross-correlation function would combine all planetary lines from within a spectrum in one function, the detection rate increases with the number of planetary lines. Thus, a large number of lines (e.g. in a molecular band) is a benefit for a cross-correlation search for planetary lines. When cross-correlating two observed spectra with each other, planetary emission would result in the differential planetary radial velocity signal. Since HD 217107 b and GJ 86 b are non-transiting, the differential radial velocity values cannot be precisely computed. Depending on the time of observation a range of possible radial velocity values has to be considered, due to the unknown inclination. However, other possibly emerging radial velocities in the cross-correlation function would be caused by stellar and/or telluric lines and differ from the expected planetary radial velocity range.

Cross-Correlation of the Star-Planet Spectra

We apply the cross-correlation technique to the mean spectrum of each observing night. As described in Sec. 4.2.2, we separate the spectra of HD 217107 into two mean spectra, one for the first half of night 1 and one for the second half of night 1.

The detectors are treated separately because of the gaps between the detectors. As input spectra for the cross correlations, we use the nightly mean spectra and choose to use the spectra in a range of 6 nm around the rest position of the H_3^+ lines that show a high intensity in the theoretical emission spectrum. We choose not to use larger portions of the

spectra, since H_3^+ emits only in a few lines and using a wider wavelength range as input for the cross-correlation increases the noise due to the remaining telluric residuals and stellar lines in the spectra.

From our calculations of the planetary radial velocity range in dependence of the inclination i , we made sure that the emission lines could not be shifted outwards of our chosen chunk-size. Again, we do not use detector No. 4 in our cross-correlation analysis, since the H_3^+ emission lines lie at the red edge of the spectrum. For our measurements, these lines could be shifted outside the wavelength range of this setting for the majority of possible inclination values due to the planets radial velocity. Thus we use the detectors No. 1-3 for the cross-correlation analysis. In all of these spectra, strong spikes are removed by a smoothed median spectrum.

We then perform a cross-correlation for each detector, using the nightly mean spectra of the observing nights. For the spectra of the first night of observations of HD 217107, we perform the cross-correlations with the spectra computed for each half night (here named night 1a and night 1b for the first and second half of the night, respectively) together with the second night of observations.

Figures 4.17 and 4.20 show the input spectra that are used for the cross-correlations. The results from the computations are shown in Fig. 4.18 and Fig. 4.21.

We would expect a signal of the planetary atmosphere in each of the detectors, showing the differential planetary radial velocity. The range of the possible differential planetary radial velocity values is corresponding to the the x-axis of the plots. An overview on the cross correlation result is given in the insets, with the red boxes corresponding to the curves of the larger plots.

The total integration time differs for both objects in both observation nights, which has an impact on the data quality of the mean spectra per observing night. This can be seen directly in the signal-to-noise ratios computed

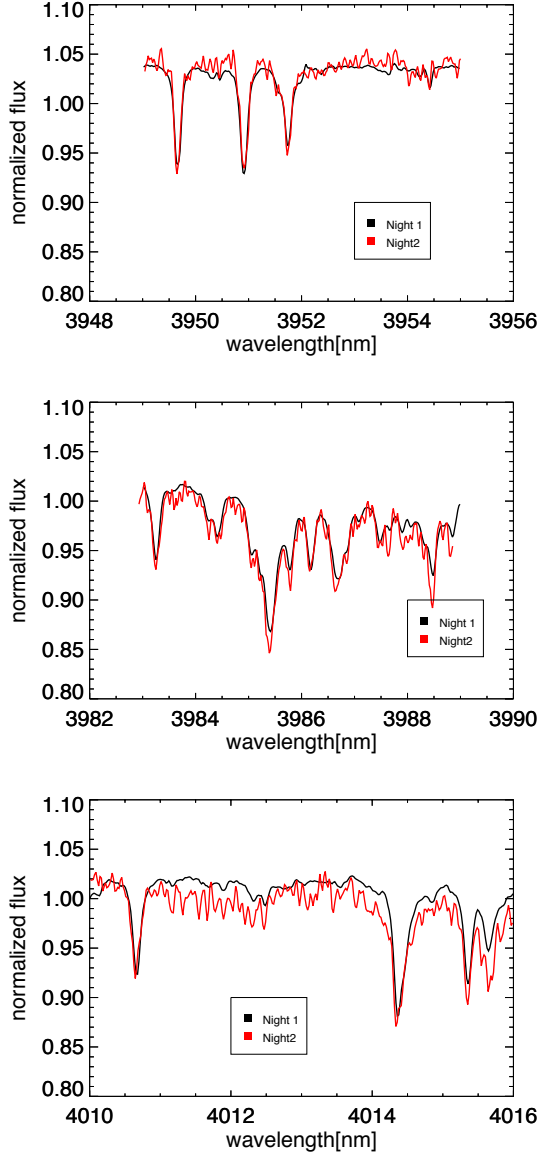


Figure 4.17: HD 217107: Input spectra for the cross-correlation results which are shown in Fig. 4.18. Detectors No. 1-3 are shown from top to bottom. The normalized mean spectrum for night 1a is shown in black, the normalized mean spectrum for night 2 in red. The shift of the spectra due to the correction for the topocentric velocity is visible in the line cores of the absorption lines.

Stellar lines in the spectra are shifted by the topocentric correction which leads to the cross-correlation signal close to 0 km/s and the symmetrical structures left and right of the main peak. The mean topocentric velocities for HD 217107 and GJ 86 for the observations are given in Table 4.2. This shift corresponding to the difference in the topocentric velocities is clearly visible in the line cores of the stellar absorption lines in the spectra, see Fig. 4.17 and Fig. 4.20.

Table 4.2: Mean topocentric velocities for the nightly mean spectra of HD 217107 and GJ 86

Object	v [km/s]
HD 217107	
Night 1a (1st half)	−27.21 km/s f
Night 1b (2nd half)	−27.35 km/s
Night 2	−27.69 km/s
GJ 86	
Night 1	−2.85 km/s
Night2	−11.98 km/s

The cross-correlation results for HD 217107 are shown in Fig. 4.18 and in Fig. 4.19. For both plots, night 2 of observations is cross-correlated against night 1a and night 1b, respectively. The plot range on the x-axis of each of the plots is chosen in a way that the radial-velocity range is shown where the signal from the planet is expected. This range is corresponding to the red box in the inset, which gives an overview on the cross-correlation result. Both figures look very much alike for each of the detectors. The same is shown for GJ 86 in Fig. 4.21, the difference in topocentric velocity is larger for two observation nights of GJ 86, hence the signal from the stellar lines is visible around 9 km/s in the insets of the cross-correlation results for all three detectors.

from the nightly mean spectra (see Tab. 3.2).

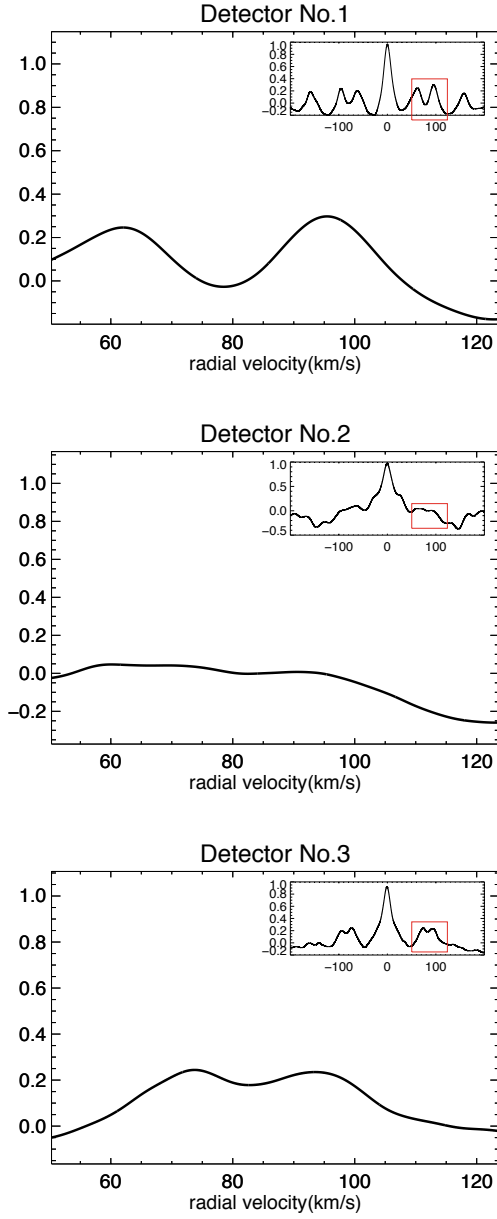


Figure 4.18: Cross-correlation results for HD 217107, using night 1a and night 2 as input. Detectors No. 1-3 are shown. The plot shows the radial-velocity range where the planetary signal would occur. This curve is corresponding to the red box in the inset image, which gives an overview on the cross-correlation result. Atmospheric emission of H_3^+ would be expected to cause signals in each of the Detectors at the same planetary radial velocity.

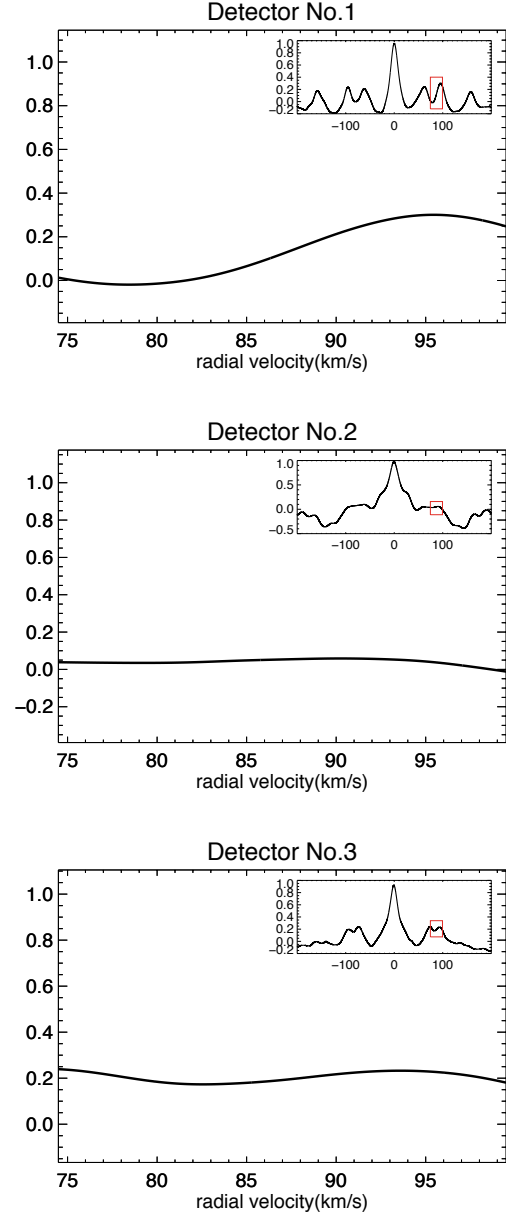


Figure 4.19: Cross-correlation results for HD 217107. Using night 1b with night 2 as input, detectors No. 1-3 are shown. For detailed description, see Fig. 4.18.

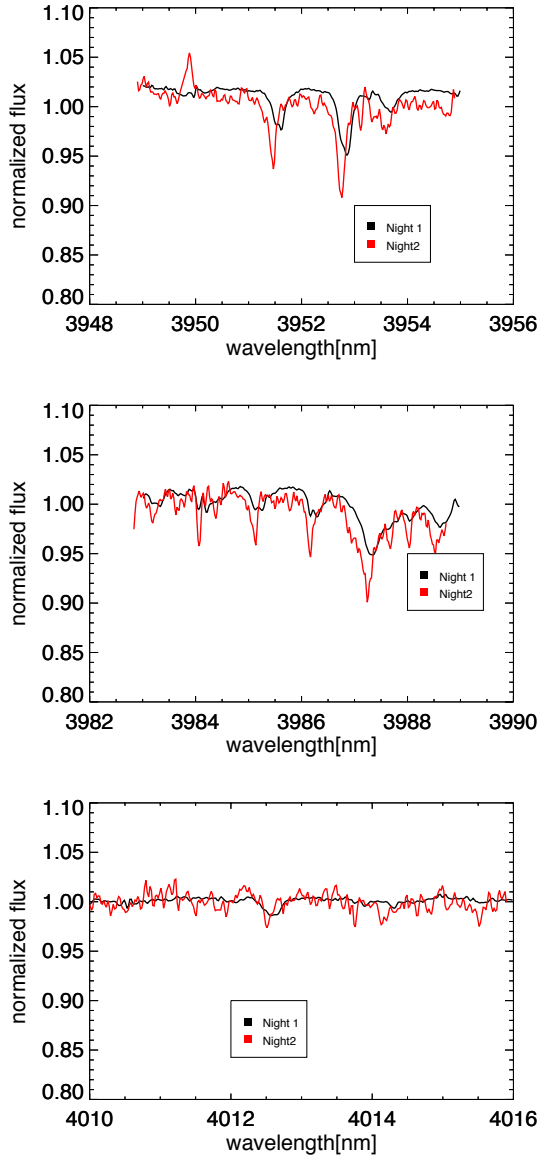


Figure 4.20: Input spectra from GJ 86 for the cross-correlation in Fig. 4.21. For a detailed description, see Fig. 4.17.

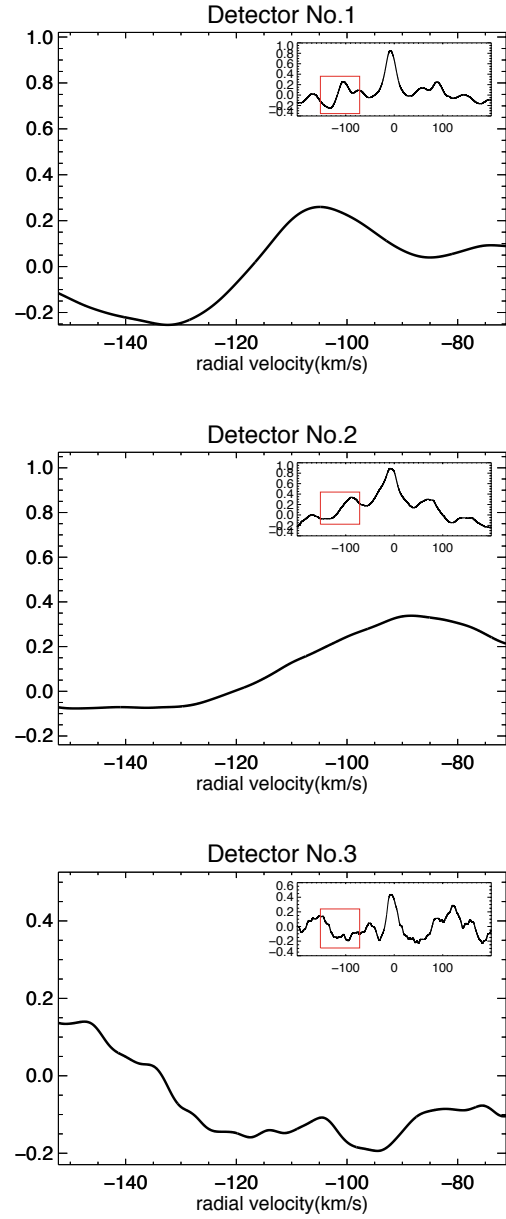


Figure 4.21: Same as Fig. 4.18 but for GJ 86.

Chapter 5

Results

This chapter introduces the results derived from the analysis of the data in the previous chapter and puts them into context to the theoretical models and previous measurements of H_3^+ emission limits.

Section 5.1 is published in *Astronomy & Astrophysics* : ‘A CRIRES-search for H_3^+ emission from the hot Jupiter atmosphere of HD 209458 b’ (Lenz et al., 2016) as the results section of the paper. This publication was written entirely by me, including the interpretation of the results from the data analysis, which was supported by discussions with the co-authors. For reasons of structuring this thesis and the flow of reading, the last sentence of Section 5.1 was removed.

5.1 Results for HD 209458

Our search for planetary emission signatures of H_3^+ in our observed spectra of HD 209458 was not successful. The direct search for the strongest emission lines detected in the aurora of Jupiter by Maillard et al. (1990) shows no emission peaks at the expected line positions. A drawback of this method is that the spectra have to be treated separately, which limits the possible signal-to-noise ratio that could be achieved by combining the observed spectra. Cross-correlating the spectra, after subtracting the last observed eclipse spectrum, gives signals that scatter around 0 km s^{-1} . This method is independent of the knowledge of the precise position of the H_3^+ lines. A rough estimation of the differential planetary radial velocity would

be sufficient to search for the radial velocity shift that would occur in case of a detection. There are weaker H_3^+ lines measured in the aurora of Jupiter around the strong lines we chose to search for with our direct search (Maillard et al., 1990). These weaker lines could help to detect a planetary signal with the cross-correlation method. The shift and add results show no emission features at the expected line positions. The method could retrieve a signal that was hidden in the stellar signal, since shifting the spectra with respect to the planetary radial velocity blurs the stellar lines. However, it requires the knowledge of the planetary radial velocity and ephemeris to shift the spectra precisely to the planetary radial velocity.

5.1.1 Emission limits from the Shift and Add Results

Maillard et al. (1990) find the H_3^+ emission line at 3985.5 nm, the $Q(3,0)$ -transition, to be the strongest in their measurements for the auroral zones of Jupiter. Shkolnik et al. (2006) use a different emission line for their search for auroral H_3^+ emission, the $Q(1,0)$ -transition at 3953.0 nm. We use our shift and add results to estimate an upper emission limit for planetary H_3^+ emission from our observations of HD 209458 (Fig.4.3) for both H_3^+ transitions. For the following emission limit calculations, we assume that all planetary H_3^+ energy is stored in one emission line, following the approach of Shkolnik et al. (2006).

We measure the standard deviation at the positions of the H_3^+ emission lines at 3985.5 nm

and 3953.0 nm in the resulting shift and add spectrum (See Tab. 5.1). To estimate the full width at half maximum (FWHM) for the emission lines, we calculate the Doppler broadening of the lines assuming a temperature of 1000 K as a rough estimate for the temperature in the lower thermosphere. H_3^+ is in strong emission in this temperature range (Miller et al., 2000). We account for the instrumental profile, derived from the measurement of the FWHM of the telluric lines and calculate resulting line widths of $\text{FWHM} = 0.76 \text{ \AA}$ for the line at 3953.0 nm and $\text{FWHM} = 0.69 \text{ \AA}$ for 3985.5 nm.

To estimate the power output of HD 209458 in the L' window, we convert the K magnitude, taken from the 2MASS catalog (Cutri et al., 2003) to the L' magnitude using the intrinsic colors from Bessell and Brett (1988). We calculate a L' magnitude of 6.258. With the L' magnitude, the bandwidth ($0.65 \mu\text{m}$) and flux density for Vega of the L' band of $5.267 \cdot 10^{-11} \text{ W m}^{-2} \mu\text{m}^{-1}$ from Cox (2000), we derive an L' band flux for HD 209458 of $1.07 \cdot 10^{-13} \text{ W m}^{-2}$. Using the distance of $d = 47.1 \text{ pc}$ (see Tab. 2.1), we derive the total L' luminosity of the star to be $2.85 \cdot 10^{24} \text{ W}$. This is in good agreement with the bolometric luminosity of HD 209458 by Cody and Sasselov (2002) of $6.1 \cdot 10^{26} \text{ W}$. For the calculation of the detection limit of our measurements, we assume that a Gaussian of 3σ peak height could be detected and derive the detection limit from the fraction of the total L' luminosity in the estimated H_3^+ equivalent width. We calculate detection limits of $5.34 \cdot 10^{18} \text{ W}$ for the emission line at 3985.5 nm and $8.32 \cdot 10^{18} \text{ W}$ at 3953.0 nm.

We compare our results to the theoretical H_3^+ limits derived by Miller et al. (2000), Yelle (2004), and Koskinen et al. (2007). Miller et al. (2000) used the Jovian ionosphere model (JIM) by Achilleos et al. (1998) and placed Jupiter in a close orbit around the sun, calculating a total H_3^+ output of 10^{17} W . Yelle (2004) derived an emission limit of 10^{16} W , based on a one-dimensional model of an EGP while choosing the system parameter to match those of HD 209458 and its orbiting planet. Koskinen

et al. (2007) used three-dimensional, self-consistent global simulations of a coupled thermosphere-ionosphere model resulting in a total power output of up to $\sim 10^{15} \text{ W}$. Koskinen et al. (2007) expected the spectral line output for the $Q(3,0)$ -transition to be 1% of the total output power of H_3^+ , hence a limit of $\sim 10^{12} \text{ W}$. The calculated emission limit for H_3^+ from the atmosphere of HD 209458 b from our observations is 1 to 3 orders of magnitude less sensitive than the theoretical predictions. The calculated spectral line output for the emission line at 3953.0 nm by Koskinen et al. (2007) is even 6 orders of magnitude away from our measurements.

Next, we compare our results to the H_3^+ emission limits reported by Shkolnik et al. (2006) and Laughlin et al. (2008). Shkolnik et al. (2006) measured detection limits for six hot Jupiter systems of different spectral types and reported a detection limit of $6.3 \cdot 10^{17} \text{ W}$ at 3953.0 nm for the M-dwarf GJ 436 that is one magnitude lower than our measurements. This difference is mainly because of its late spectral type, as the data quality is similar for all spectra used for their analysis. The detection limit results for the late F dwarfs in their sample are comparable to our limit measured for HD 209458 b, a G0 star. Laughlin et al. (2008) reported an H_3^+ limit for τ -Boo of $9.0 \cdot 10^{17} \text{ W}$, which is also half a magnitude better than our measurement. Considering the much higher resolution of CRIRES in comparison to CSHELL, but the small amount of observing time for our data, achieving roughly the same order of magnitude for the emission limits seems realistic.

5.2 Results for the Spectra of GJ 86 and HD 217107

Searching for planetary H_3^+ emission lines in the spectra of GJ 86 and HD 217107 lead to no detection of any signs of planetary emission. Each dataset consists of two nights of observations which fell on different planetary

Table 5.1: Detection limit results. (Credit: Lenz, A&A, 589, A99, 2016, reproduced with permission ©ESO)

H_3^+ line [nm]	Transition	FWHM [nm]	σ	Det. limit [W]
3953.0	$Q(1,0)$	0.076	0.0068	$8.32 \cdot 10^{18}$
3985.5	$Q(3,0)$	0.069	0.0072	$5.34 \cdot 10^{18}$

radial velocity ranges for both star-planet systems (Sec. 4.2.1). The resulting planetary radial velocities are not precisely known due to the unknown inclinations for both planetary systems. Hence, we calculated the shift range in which the lines are expected and search for emission peaks. For the first night of observations of GJ 86 b the planetary emission lines are shifted towards the red due to the planetary radial velocity. The expected line positions for the second night of observation are shifted towards the blue. Even if a possible emission line was hidden in a stellar absorption line in one of the observing nights, the chances that it would be detectable in the other night are high, due to the large differential planetary radial velocity of the two observing nights. The same is true for HD 217107, however, for the first night of observations the lines are shifted is towards the blue and for the second night of observations the lines are shifted towards the red.

We have summarized the observed spectra for each night of observations in one or two (in case of night 1 for the spectra of HD 217107) nightly mean spectra, while making sure that the intranight line shift does not exceed the expected widths of the emission lines (see Sec. 4.2.2). Neither do we detect any H_3^+ emission lines in the spectra of HD 217107, nor in the nightly mean spectra of GJ 86.

Cross-correlation of the nightly mean spectra does not lead to the detection of planetary emission signals at the expected range of planetary radial velocity values. A radial velocity signal of planetary emission lines should occur on all of the detectors at the same radial velocity value. There is no such signal detectable on

all of the detectors. Instead our results show multiple signals of the residual telluric lines from the atmospheric correction with the main peak being the differential topocentric velocity of the spectra that were used as input for the cross-correlation. The cross-correlation test could in principle support the search for atmospheric emission, since this method does not require the line positions to be known precisely, however, the detector size of CRİRES is small and only a few H_3^+ emission lines fall on each of the detectors.

In principle, the application of cross-correlation techniques for the search for planetary atmospheric emission could detect emission lines which are buried in the noise of the spectra. Since a cross-correlation function combines all molecular lines from the planet in one function, the detection rate increases with the number of molecular lines. Thus, a large number of lines (e.g. in a molecular band) is a benefit for a cross-correlation search for planetary lines.

5.2.1 Emission Limits

We use the results from the direct search (see Sec. 4.2.4) to estimate emission line limits for the two observed star-planet systems. We follow the same approach as used for the HD 209458 data, which is described in Sec. 5.1.1. As suggested by Shkolnik et al. (2006), in this approach it is assumed that all emitted light from H_3^+ is stored in one emission line. Shkolnik et al. (2006) use the $Q(1,0)$ -transition at 3953.0 nm for their emission limit calculation. Maillard et al. (1990) however, find the $Q(3,0)$ -transition at 3985.5 nm to be the strongest emission line in the auroral zones of Jupiter. We calculate

the emission limits for both H_3^+ emission lines separately in order to compare them to previous attempts for the search for planetary H_3^+ emission.

We measure the standard deviation of the resulting nightly mean spectra at the H_3^+ line position for the $Q(1,0)$ -transition at 3953.0 nm and at 3985.5 nm, ($Q(3,0)$). For our calculation of the detection limits, we assume that we could detect a Gaussian spectral feature with a threshold of 3σ peak height. We follow the calculation steps that are described in Sec.5.1.1 with the parameters listed in Tab.5.2 for both observed objects to obtain the total L' luminosity. The emission limits are obtained by calculating the fraction of L' luminosity in the estimated H_3^+ equivalent width. The resulting emission limits for the different observations are listed in Tab.5.3. The best detection limit result was achieved for the $Q(1,0)$ -transition at 3953.0 nm for HD 217107 b: we derive a limit of $2.88 \cdot 10^{16}$ W for the first half night of observations (night 1a) with an integration time of 5400 s.

The comparison of the emission limits to the theoretical limits from the literature leads to the following findings: the emission limits for both EGP, HD 217107 b and GJ 86 b are in the range of the emission limit calculated by Miller et al. (2000). They derived a total H_3^+ output of 10^{17} W using the Jovian ionosphere model (JIM) by Achilleos et al. (1998) and placing Jupiter in a closed orbit around the Sun. The emission limit for H_3^+ derived for a star-planet system with the system parameters of HD 209458 by Yelle (2004) is 10^{16} W. The calculations are based on a one dimensional model of an EGP.

Our best measurement for HD 217107 is $2.88 \cdot 10^{16}$ W for the $Q(1,0)$ transition in the first half night (Night 1a) of observations. This is in the range of the limit that was derived by Yelle (2004) and exceeds the theoretical estimations by Miller et al. (2000). However, we do not detect emission of H_3^+ for neither the spectra of HD 217107 b, nor GJ 86 b.

Koskinen et al. (2007) calculated a total

H_3^+ output of up to $\sim 10^{15}$ W using a three-dimensional self-consistent global simulation of a coupled thermosphere-ionosphere model. They expected the spectral line output for a single line (the $Q(3,0)$ -transition) to be only 1% of the total output power. This limit for a single line of $\sim 10^{12}$ W is still four orders of magnitude away from our measurements.

Next, we compare our derived emission limits for HD 217107 b and GJ 86 b to previously obtained emission limits from observations of hot Jupiters. Shkolnik et al. (2006) observed six hot Jupiter systems with different spectral types with CSHELL at the NASA Infrared Telescope Facility (IRTF) and measured their detection limits. They report a detection limit of $6.3 \cdot 10^{17}$ W for the $Q(1,0)$ transition at 3953.0 nm, which was measured for the M-dwarf GJ 436. For their observations of HD 217107, they derive an H_3^+ emission limit for the hot Jupiter of $1.1 \cdot 10^{19}$ W in an observation time of 4080 s.

Laughlin et al. (2008) derived an H_3^+ emission limit for τ -Boo of $9.0 \cdot 10^{17}$ W using CSHELL, as well. In our first attempt (Lenz et al. (2016)), we observed HD 209458 and derived a detection limit of $5.3 \cdot 10^{18}$ W for the $Q(3,0)$ transition. As we proposed in Lenz et al. (2016), we were able to push the detection limit down to $\sim 5 \cdot 10^{16}$ W by choosing targets with convenient parameters for this kind of observation, as well as extending the observation time quite a lot in comparison to the observations of HD 209458. Comparing our measurements to the results for HD 217107 from Shkolnik et al. (2006), we were able to push their limit down by two orders of magnitude. Using CRIRES, which has a much higher resolution than CSHELL, we were able to achieve a detection limits, which are a magnitude below the previously reported best measurements.

Table 5.2: Parameter for the emission limit calculations

Object	K Mag ¹	L' Mag ²	distance	L' band luminosity
			[pc]	[W]
Gj 86	4.125	4.065	10.9	$1.15 \cdot 10^{24}$
HD 217107	4.536	4.486	19.72	$2.55 \cdot 10^{24}$

¹ K magnitudes from the 2MASS catalogue² conversion from the K magnitude with Bessell and Brett (1988)**Table 5.3:** Detection limit results for HD 217107 b and GJ 86 b. The lowest emission limit, derived for HD 217107 b is highlighted in red color.

$Q(1, 0)$ at 3953.0 nm					$Q(3, 0)$ at 3985.5 nm		
Object		FWHM [nm]	σ	Det. limit [W]	FWHM [nm]	σ	Det. limit [W]
GJ 86	Night 1	0.076	0.0067	$1.74 \cdot 10^{17}$	0.069	0.0084	$2.00 \cdot 10^{17}$
	Night 2	0.076	0.0108	$2.78 \cdot 10^{17}$	0.069	0.0119	$2.82 \cdot 10^{17}$
HD 217107	Night 1a	0.076	0.0005	$2.88 \cdot 10^{16}$	0.069	0.0235	$1.24 \cdot 10^{18}$
	Night 1b	0.076	0.0009	$5.17 \cdot 10^{16}$	0.069	0.0204	$1.29 \cdot 10^{18}$
	Night 2	0.076	0.0030	$1.74 \cdot 10^{17}$	0.069	0.0244	$1.97 \cdot 10^{19}$

5.3 Prospects for H_3^+ Observations in the Future

Our second observing run 2012 with CRIRES led to far better results in terms of data quality compared to the previous run. We were able to obtain a much larger number of spectra for each of the observed systems than in the previous observations of HD 209458 in 2010. Due to unfavorable weather conditions, we obtained only 150 seconds of observations of HD 209458 in 2010. In the 2012 run, we observed three hours on target for HD 217107. These spectra of HD 217107 push the detection limit down to $\sim 5 \cdot 10^{16} \text{ W}$ which is the emission limit that we expected to achieve with CRIRES in a reasonable amount of observing time (Lenz et al., 2016).

Preferably, future searches for H_3^+ emission would target transiting EGP, which would allow for eclipse spectroscopy. Subtracting the stellar spectra could support the detection of the handful of emission lines of H_3^+ . Additionally, the distance between the planet and its host star is an important parameter for the choice of target candidates. However, the theoretical estimations for high H_3^+ emissions differ: an orbital distance of approximately 0.1 AU was suggested by Maillard and Miller (2011), in order to have a good balancing between input flux of the host star and dissociation of H_2 . Koskinen et al. (2007) however, suggest that the most efficient H_3^+ -cooling for EGP atmospheres happens at orbital distances between 0.2 and 1.0 AU.

The theoretical estimations for H_3^+ emission of EGP by Koskinen et al. (2007) predict very faint signals for single H_3^+ lines: they calculate a spectral line output for the $Q(3, 0-)$ line of $4.8 \cdot 10^{12} \text{ W}$ for a close-in giant planet around a Sun-like star. Current IR-spectrographs do not have the sensitivity to detect such faint signals. In the following subsections, the upcoming near-infrared spectrographs are introduced and their suitability for the possible observation of H_3^+ from hot Jupiter atmospheres is discussed.

5.3.1 Ground Based Instrumentation iShell

iShell¹ was installed at the NASA Infrared Telescope Facility (IRTF) in September 2016. The IRTF is a 3m telescope at Mauna Kea (Hawaii). iShell is the successor of CSHELL. It is a cross dispersed spectrograph and operates in the infrared wavelength range from $1.1 - 5.3 \mu\text{m}$ with a resolving power of $R \sim 75.000$. Since previous experiments for the observation of H_3^+ emission of exoplanets were not successful and only upper limits were found, future observing attempts for H_3^+ emission of exoplanets should make use of the most sensitive instrument for this purpose. Hence, in the near future CRIRES+ at the VLT which provides a larger telescope mirror and higher resolution should be preferred over iShell at the IRTF.

CRIRES+

In 2014, CRIRES was removed from UT 1 at the VLT and brought to the ESO headquarters in Garching for a major upgrade. CRIRES+² is expected to return to Paranal in the fall of 2019 and commissioning will take place in the months after the spectrograph is successfully installed at the Nasmyth B focus of UT 3. The new design of the spectrograph includes the installation of cross-dispersing elements, newer and larger detectors and gas cells and a Fabry-Pérot etalon for wavelength calibration, while maintaining the total operational wavelength range and the very high resolution of the original CRIRES instrument ($R \sim 100.000$). The cross disperser will extend the wavelength range of the instrument during one observation by a factor of ten, in comparison to the previous spectrograph. It will cover a wavelength range around the center wavelength of about $\lambda/70$ (at $1 \mu\text{m}$) up to $\lambda/50$ (at $5 \mu\text{m}$) per order (Seemann et al., 2014). The new design aims to increase the observing efficiency of the

¹ <http://irtfweb.ifa.hawaii.edu/~ishell/>

² https://www.eso.org/sci/facilities/develop/instruments/crires_up.html

instrument and to enable high-precision radial-velocity measurements with the installation of additional wavelength calibration options, as gas cells and a Fabry-Pérot interferometer.

The upgraded instrument will allow to track a large part of the H_3^+ emission band around $4\mu\text{m}$ simultaneously. In contrast to the original CRIRES, the upgraded instrument will comprise several strong absorption lines in one single spectrum, which will improve the possibilities to perform cross correlation searches for emission lines, since the detectability increases with the number of lines. However, in contrast to the absorption line forests of molecules like CO, or NH_3 (see Brogi et al. (2014)), H_3^+ emits only in a few intense lines. Hence, if CRIRES+ delivers the highly increased observing efficiency in comparison to the previous instrument, one should test the efficiency of the instrument for the observation of H_3^+ , as well as analyzing the data with the cross-correlation approach. We have calculated the approximate observing times for H_3^+ detection limits for different upcoming instruments and their varying collecting area in Lenz et al. (2016). In order to reach an emission limit of $\cdot 10^{16}\text{ W}$, we derived an observation time of 9300 min for the old CRIRES spectrograph. A large sample search for H_3^+ emission cannot be that expensive in observation time.

METIS

METIS (Brandl et al., 2014) is one of the three first light instruments for the European Extremely Large Telescope (E-ELT³), its agreement for design and construction was signed in 2015. METIS is planned as a high resolution spectrograph ($R \sim 100.000$) covering the wavelength range from $3 - 5\mu\text{m}$, fed through an integrated field unit. METIS is expected to enable the study of high resolution spectra line by line, instead of reconstructing the planetary signal through the combination of many lines, as it is common today. Also, the ability

to study of individual atmospheric lines will help to retrieve signals of planetary rotation through line broadening, or even atmospheric winds (Snellen, 2013). Since the current design of METIS is outlined as an integrated field unit spectrograph, the benefit will lie in the larger collection area of the telescope and (hopefully) a more efficient throughput than CRIRES. Our estimate for H_3^+ observations with the E-ELT in Lenz et al. (2016) was an observation time of 390 min in order to achieve an emission limit of 10^{16} W . A cross dispersed spectrograph, as the upgrade CRIRES+, however, would allow for a much larger instantaneous wavelength range to be recorded and hence another order of precision for certain observations.

5.3.2 Space Based Instrumentation

Space based observations deliver very sensitive measurements since no disturbances due to Earth's atmosphere can occur. From the upcoming satellite missions, the James Webb Space Telescope (NASA) and ARIEL (ESA) will both host instrumentation that is designed for the observation of exoplanetary atmospheres.

MIRI and NIRSpec at the James Webb Space Telescope

The James Webb Space telescope (JWST) will host two instruments that are capable for spectroscopy of exoplanet atmospheres. The Mid-Infrared Instrument (MIRI) covers the wavelength ranges from $4.6\mu\text{m}$ to $28.6\mu\text{m}$ and hosts four separate channels, each with its own gratings and image slicers. The instrument also provides coronagraphy for the study of exoplanets. The spectroscopy mode is realized as integral field spectroscopy with a resolving power of $R \sim 3000$. However, MIRI does not provide spectroscopy in the $3.9\mu\text{m}$ regime for the observation of H_3^+ . The Near Infrared Spectrograph (NIRSpec) will cover spectroscopy with fixed slits in the spectral region of $0.6 - 5.3\mu\text{m}$ and the highest resolving power provided will be $R \sim 2700$. One of the slit modes is optimized for the observation of transiting exo-

³ https://www.eso.org/sci/facilities/eelt/docs/e-elt_constrproposal.pdf

planets. Thus it will be capable of observations of hot Jupiter planets and hence the search of H_3^+ emission. The resolving power is very low, comparing to the upcoming ground based instruments. However, space based observations benefit from the advantages of increased sensitivity, because the observations cannot be disturbed by Earth's atmosphere.

ARIEL

ARIEL (Tinetti et al., 2017) is the fourth medium-class science mission from the European Space Agency (ESA) to be launched in 2028. Mission one to three are Solar Orbiter (launch currently planned for 2020), Euclid (2020), and Plato (2026). The experiment is dedicated to the characterization of atmospheres of exoplanets. The satellite will host a 1m class telescope and the science instruments are planned as a combination of multiple band-photometry in the optical and NIR regime, as well as combined-light spectroscopy from $\sim 1.2 - 7.8 \mu\text{m}$. The observational strategy is to perform transit and eclipse spectroscopy methods on warm and hot exoplanets, in the range from hot Jupiters to super earths. Since the atmospheres of hot Jupiters are well mixed, the study of the upper atmospheres of these planets allows for a general assumption on the overall composition of the atmosphere (bulk composition). The analysis of a large number of these bulk atmospheres will help to understand the chemical nature of the observed exoplanets. The ARIEL mission dedicated to the analysis of planetary atmospheres, especially of warm planets and hot Jupiters is the most promising upcoming experiment that could deliver measurements of H_3^+ in exoplanet atmospheres.

Chapter 6

Summary

We observed three hot Jupiter systems with high-resolution ground-based spectroscopy using CRIRES at the VLT in order to detect H_3^+ emission lines in the planet's atmospheres.

H_3^+ emission is measured in Jupiter's aurora, where the emitting molecule acts as a thermostat and cools the upper atmosphere of the planet by radiating energy into space. Hot Jupiter's atmospheres are expected to experience the same effect.

A detection of H_3^+ emission from a hot Jupiter would give insight on the conditions in the upper atmosphere and possibly information about their magnetic field (Maillard and Miller, 2011). The direct detection of planetary atmospheric lines would also allow to directly measure the planets radial velocity and thus to determine a model-independent stellar mass.

In 2010, we obtained spectra of the transiting planet HD 20948 b. In the second run in 2012, our targets were HD 217107 b and GJ 86 b, which are both non-transiting. CRIRES is a very high-resolution spectrograph ($R \sim 100,000$) that was mounted at the 8m UT1/VLT telescope. Since close-in EGP are expected to be tidally locked, atmospheric features are expected to not be broadened by rotation. In consequence, the expected spectral lines are very narrow, hence, the sensitivity increases proportional to the spectral resolution. CRIRES met the requirements for our observations in order to yield a maximal photon signal, as well as achieving very high contrast.

However, the environmental conditions for H_3^+ to form, limit the orbital distance of the

planet to a certain regime: if the orbit is too close, H_2 dissociates and H_3^+ cannot form and help to balance the heating by the host star - the planet is expected to undergo atmospheric evaporation. If the orbit is too far out, the input flux of the host star is not sufficient to support the formation of H_3^+ .

With the spectra from HD 209458 b, we obtained an estimate for the suitability of CRIRES for the observation of H_3^+ in the atmospheres of hot Jupiters. We obtained 12 spectra during secondary eclipse of the planet, as well as four spectra, that contain the combined light of the planet and the star. We used these 'combined light' spectra to search for H_3^+ emission at the same line positions in the $4\mu\text{m}$ wavelength regime that were measured by Maillard et al. (1990) in Jupiter's aurora. We searched for H_3^+ emission with three different approaches: First, we searched directly for emission bulges at the expected line positions in the spectra. Second, we tested a cross-correlation approach while subtracting the stellar signal from the secondary eclipse and, as a last test, shifted all spectra with respect to their planetary radial velocity at the time of observation and then added up the flux binwise, creating a 'shift-and-add' frame.

Our Analysis for HD 209458 b did not reveal any signs of H_3^+ emission and we used the resulting 'shift-and-add' frame to derive an upper emission limit for our observations of $5.34 \cdot 10^{18} \text{ W}$ for the emission line at 3985.5 nm and $8.32 \cdot 10^{18} \text{ W}$ at 3953.0 nm. These emission limits are comparable to the results from previ-

ous attempts to measure H_3^+ emission from hot Jupiter atmospheres by Shkolnik et al. (2006) and Laughlin et al. (2008). However, comparing our results to the theoretical predictions (Maillard et al., 1990; Miller et al., 2000), the theoretical predictions for the emission of H_3^+ from hot Jupiter atmospheres are one to three orders of magnitude weaker than our measurements.

From the results gained in this experiment, we derived the best suited target candidates to push the expected emission limit below the theoretical predictions of $\sim 10^{17}$ W from Miller et al. (2000). Our choice for the target systems for our observing run in 2012 was led by the idea to test two different scenarios for the formation of H_3^+ : we observed HD 217107 b, which is close to its host star and hence experiences a lot input flux, as well as GJ 86 b, a hot Jupiter system which is in close location to Earth, which increases the detectability of planetary emission.

HD 217107 b and GJ 86 b are both non-transiting planets, hence the radial velocity of the planet is only known in dependence of the unknown inclination angle i . In our analysis, we searched the spectra directly, for emission bulges at the expected line positions and applied a cross-correlation approach in order to search for H_3^+ emission features. Due to the unknown planetary radial velocity, the shift-and-add approach that was applied to the data for HD 209458 was not viable for these systems. We could not identify H_3^+ emission signals in our spectra of HD 217107 b and GJ 86. We derived the emission limits from the nightly mean spectra of the observations. We obtained our best result with the first night of observations of HD 217107 b, for which we calculate an emission limit of $2.88 \cdot 10^{16}$ W for the emission line at 3985.5 nm. This emission limit is below the theoretical predictions from Miller et al. (2000) of 10^{17} W and close to the predictions by Yelle (2004) of 10^{16} W. With these measurements, we reach our estimations for the expected data quality for an intensive search for H_3^+ emission from exoplanet atmo-

spheres with CRIRES (see Lenz et al. (2016)).

In the near future, CRIRES+ will be the preferred upcoming instrument in the infrared wavelength regime to run another test for the observation atmospheric emission of H_3^+ from hot Jupiter planets. The cross dispersed spectrograph will allow to simultaneously record a large amount of the H_3^+ emission band at $4 \mu\text{m}$ and hence will support the cross-correlation approach for the search for H_3^+ emission.

However, Koskinen et al. (2007) derived an H_3^+ emission limit of $\sim 10^{12}$ W as a single line flux from a close-in EGP. As we stated in Lenz et al. (2016), this limit will be very difficult to reach with ground-based facilities in the near future, including CRIRES+.

The upcoming E-ELT and similar future giant telescopes will have large mirror diameters, which translates directly into the photon collection areas. This next generation of giant telescopes will enable detailed studies of hot Jupiter atmospheres, including the search for H_3^+ emission. Hence, large surveys for H_3^+ emission of hot Jupiter atmospheres aiming for detection limits of 10^{15} W and below will become possible.

Acknowledgements

This research has made use of the NASA Exoplanet Archive, which is operated by the California Institute of Technology, under contract with the National Aeronautics and Space Administration under the Exoplanet Exploration Program.

Based on observations collected at the European Organisation for Astronomical Research in the Southern Hemisphere, Chile, 086.C-0045 and 090.C-0244

The molecfit software was used for the correction of the telluric absorption features of the data of HD 217107 and GJ 86: <http://www.uibk.ac.at/eso/software>.

Bibliography

- Achilleos, N., Miller, S., Tennyson, J., Aylward, A. D., Mueller-Wodarg, I., and Rees, D. (1998). JIM: A time-dependent, three-dimensional model of Jupiter's thermosphere and ionosphere. *J. Geophys. Res.*, 103:20089–20112.
- Adams, E. R., Seager, S., and Elkins-Tanton, L. (2008). Ocean Planet or Thick Atmosphere: On the Mass-Radius Relationship for Solid Exoplanets with Massive Atmospheres. *ApJ*, 673:1160–1164.
- Anderson, K. A. (1960). Balloon Observations of X Rays in the Auroral Zone I. *J. Geophys. Res.*, 65:551.
- Anglada-Escudé, G., Amado, P. J., Barnes, J., Berdiñas, Z. M., Butler, R. P., Coleman, G. A. L., de La Cueva, I., Dreizler, S., Endl, M., Giesers, B., Jeffers, S. V., Jenkins, J. S., Jones, H. R. A., Kiraga, M., Kürster, M., López-González, M. J., Marvin, C. J., Morales, N., Morin, J., Nelson, R. P., Ortiz, J. L., Ofir, A., Paardekooper, S.-J., Reiners, A., Rodríguez, E., Rodríguez-López, C., Sarmiento, L. F., Strachan, J. P., Tsapras, Y., Tuomi, M., and Zechmeister, M. (2016). A terrestrial planet candidate in a temperate orbit around Proxima Centauri. *Nature*, 536:437–440.
- Bailey, J., Simpson, A., and Crisp, D. (2007). Correcting Infrared Spectra for Atmospheric Transmission. *PASP*, 119:228–236.
- Ballester, G. E., Clarke, J. T., Trauger, J. T., Harris, W. M., Stapelfeldt, K. R., Crisp, D., Evans, R. W., Burgh, E. B., Burrows, C. J., Casertano, S., Gallagher, J. S., Griffiths, R. E., Hester, J. J., Hoessel, J. G., Holtzman, J. A., Krist, J. E., Meadows, V., Mould, J. R., Sahai, R., Scowen, P. A., Watson, A. M., and Westphal, J. A. (1996). Time-resolved observations of jupiter's far-ultraviolet aurora. *Science*, 274(5286):409–413.
- Barman, T. S., Konopacky, Q. M., Macintosh, B., and Marois, C. (2015). Simultaneous Detection of Water, Methane, and Carbon Monoxide in the Atmosphere of Exoplanet HR8799b. *ApJ*, 804:61.
- Batalha, N. M., Rowe, J. F., Bryson, S. T., Barclay, T., Burke, C. J., Caldwell, D. A., Christiansen, J. L., Mullally, F., Thompson, S. E., Brown, T. M., Dupree, A. K., Fabrycky, D. C., Ford, E. B., Fortney, J. J., Gilliland, R. L., Isaacson, H., Latham, D. W., Marcy, G. W., Quinn, S. N., Ragozzine, D., Shporer, A., Borucki, W. J., Ciardi, D. R., Gautier, Thomas N., I., Haas, M. R., Jenkins, J. M., Koch, D. G., Lissauer, J. J., Rapin, W., Basri, G. S., Boss, A. P., Buchhave, L. A., Carter, J. A., Charbonneau, D., Christensen-Dalsgaard, J., Clarke, B. D., Cochran, W. D., Demory, B.-O., Desert, J.-M., Devore, E., Doyle, L. R., Esquerdo, G. A., Everett, M., Fressin, F., Geary, J. C., Girouard, F. R., Gould, A., Hall, J. R., Holman, M. J., Howard, A. W., Howell, S. B., Ibrahim, K. A., Kinemuchi, K., Kjeldsen, H., Klaus, T. C., Li, J., Lucas, P. W., Meibom, S., Morris, R. L., Prša, A., Quintana, E., Sanderfer, D. T., Sasselov, D., Seader, S. E., Smith, J. C., Steffen, J. H., Still, M., Stumpe, M. C., Tarter, J. C., Tenenbaum, P., Torres, G., Twicken,

- J. D., Uddin, K., Van Cleve, J., Walkowicz, L., and Welsh, W. F. (2013). Planetary Candidates Observed by Kepler. III. Analysis of the First 16 Months of Data. *The Astrophysical Journal Supplement Series*, 204:24.
- Beaulieu, J. P., Kipping, D. M., Batista, V., Tinetti, G., Ribas, I., Carey, S., Noriega-Crespo, J. A., Griffith, C. A., Campanella, G., Dong, S., Tennyson, J., Barber, R. J., Deroo, P., Fossey, S. J., Liang, D., Swain, M. R., Yung, Y., and Allard, N. (2010). Water in the atmosphere of HD 209458b from 3.6-8 μ m IRAC photometric observations in primary transit. *MNRAS*, 409:963–974.
- Bessell, M. S. and Brett, J. M. (1988). JHKLM photometry - Standard systems, passbands, and intrinsic colors. *PASP*, 100:1134–1151.
- Beuzit, J. L., Feldt, M., Dohlen, K., Mouillet, D., Puget, P., Antichi, J., Baruffolo, A., Baudoz, P., Berton, A., Boccaletti, A., Carbillet, M., Charton, J., Claudi, R., Downing, M., Feautrier, P., Fedrigo, E., Fusco, T., Gratton, R., Hubin, N., Kasper, M., Langlois, M., Moutou, C., Mugnier, L., Pragt, J., Rabou, P., Saisse, M., Schmid, H. M., Stadler, E., Turrato, M., Udry, S., Waters, R., and Wildi, F. (2006). SPHERE: A 'Planet Finder' Instrument for the VLT. *The Messenger*, 125:29.
- Bolton, S. J., Lunine, J., Stevenson, D., Connerney, J. E. P., Levin, S., Owen, T. C., Bagenal, F., Gautier, D., Ingersoll, A. P., Orton, G. S., Guillot, T., Hubbard, W., Bloxham, J., Coradini, A., Stephens, S. K., Mokashi, P., Thorne, R., and Thorpe, R. (2017). The Juno Mission. *Space Sci. Rev.*, 213:5–37.
- Bourrier, V. and Lecavelier des Etangs, A. (2013). 3D model of hydrogen atmospheric escape from HD 209458b and HD 189733b: radiative blow-out and stellar wind interactions. *A&A*, 557:A124.
- Brandl, B. R., Feldt, M., Glasse, A., Guedel, M., Heikamp, S., Kenworthy, M., Lenzen, R., Meyer, M. R., Molster, F., Paalvast, S., Pantin, E. J., Quanz, S. P., Schmalzl, E., Stuik, R., Venema, L., and Waelkens, C. (2014). METIS: the mid-infrared E-ELT imager and spectrograph. In *Society of Photo-Optical Instrumentation Engineers (SPIE) Conference Series*, volume 9147 of *Society of Photo-Optical Instrumentation Engineers (SPIE) Conference Series*, page 21.
- Brittain, S. D. and Rettig, T. W. (2002). CO and H₃⁺ in the protoplanetary disk around the star HD141569. *Nature*, 418:57–59.
- Brogi, M., de Kok, R. J., Birkby, J. L., Schwarz, H., and Snellen, I. A. G. (2014). Carbon monoxide and water vapor in the atmosphere of the non-transiting exoplanet HD 179949 b. *A&A*, 565:A124.
- Butler, R. P., Wright, J. T., Marcy, G. W., Fischer, D. A., Vogt, S. S., Tinney, C. G., Jones, H. R. A., Carter, B. D., Johnson, J. A., McCarthy, C., and Penny, A. J. (2006). Catalog of Nearby Exoplanets. *ApJ*, 646:505–522.
- Charbonneau, D., Brown, T. M., Latham, D. W., and Mayor, M. (2000). Detection of Planetary Transits Across a Sun-like Star. *ApJ*, 529:L45–L48.
- Charbonneau, D., Brown, T. M., Noyes, R. W., and Gilliland, R. L. (2002). Detection of an Extrasolar Planet Atmosphere. *ApJ*, 568:377–384.
- Chauvin, G., Desidera, S., Lagrange, A. M., Vigan, A., Gratton, R., Langlois, M., Bonnefoy, M., Beuzit, J. L., Feldt, M., Mouillet, D., Meyer, M., Cheetham, A., Biller, B., Boccaletti, A.,

- D’Orazi, V., Galicher, R., Hagelberg, J., Maire, A. L., Mesa, D., Olofsson, J., Samland, M., Schmidt, T. O. B., Sissa, E., Bonavita, M., Charnay, B., Cudel, M., Daemgen, S., Delorme, P., Janin-Potiron, P., Janson, M., Keppler, M., Le Coroller, H., Ligi, R., Marleau, G. D., Messina, S., Mollière, P., Mordasini, C., Müller, A., Peretti, S., Perrot, C., Rodet, L., Rouan, D., Zurlo, A., Dominik, C., Henning, T., Menard, F., Schmid, H. M., Turatto, M., Udry, S., Vakili, F., Abe, L., Antichi, J., Baruffolo, A., Baudoz, P., Baudrand, J., Blanchard, P., Bazzon, A., Buey, T., Carbillet, M., Carle, M., Charton, J., Cascone, E., Claudi, R., Costille, A., Deboulbe, A., De Caprio, V., Dohlen, K., Fantinel, D., Feautrier, P., Fusco, T., Gigan, P., Giro, E., Gisler, D., Gluck, L., Hubin, N., Hugot, E., Jaquet, M., Kasper, M., Madec, F., Magnard, Y., Martinez, P., Maurel, D., Le Mignant, D., Möller-Nilsson, O., Llored, M., Moulin, T., Origné, A., Pavlov, A., Perret, D., Petit, C., Pragt, J., Puget, P., Rabou, P., Ramos, J., Rigal, R., Rochat, S., Roelfsema, R., Rousset, G., Roux, A., Salasnich, B., Sauvage, J. F., Sevin, A., Soenke, C., Stadler, E., Suarez, M., Weber, L., Wildi, F., Antonucci, S., Augereau, J. C., Baudino, J. L., Brandner, W., Engler, N., Girard, J., Gry, C., Kral, Q., Kopytova, T., Lagadec, E., Milli, J., Moutou, C., Schlieder, J., Szulágyi, J., Thalmann, C., and Wahhaj, Z. (2017). Discovery of a warm, dusty giant planet around HIP 65426. *A&A*, 605:L9.
- Clarke, J. T., Ajello, J., Ballester, G., Ben Jaffel, L., Connerney, J., Gérard, J. C., Gladstone, G. R., Grodent, D., Pryor, W., Trauger, J., and Waite, J. H. (2002). Ultraviolet emissions from the magnetic footprints of Io, Ganymede and Europa on Jupiter. *Nature*, 415:997–1000.
- Cody, A. M. and Sasselov, D. D. (2002). HD 209458: Physical Parameters of the Parent Star and the Transiting Planet. *ApJ*, 569:451–458.
- Cox, A. N. (2000). *Allen’s astrophysical quantities*.
- Cuntz, M., Saar, S. H., and Musielak, Z. E. (2000). On Stellar Activity Enhancement Due to Interactions with Extrasolar Giant Planets. *ApJ*, 533:L151–L154.
- Cutri, R. M., Skrutskie, M. F., van Dyk, S., Beichman, C. A., Carpenter, J. M., Chester, T., Cambresy, L., Evans, T., Fowler, J., Gizis, J., Howard, E., Huchra, J., Jarrett, T., Kopan, E. L., Kirkpatrick, J. D., Light, R. M., Marsh, K. A., McCallon, H., Schneider, S., Stiening, R., Sykes, M., Weinberg, M., Wheaton, W. A., Wheelock, S., and Zacarias, N. (2003). 2MASS All-Sky Catalog of Point Sources (Cutri+ 2003). *VizieR Online Data Catalog*, 2246:0.
- Diamond-Lowe, H., Stevenson, K. B., Bean, J. L., Line, M. R., and Fortney, J. J. (2014). New Analysis Indicates No Thermal Inversion in the Atmosphere of HD 209458b. *ApJ*, 796:66.
- Drossart, P., Maillard, J.-P., Caldwell, J., Kim, S. J., Watson, J. K. G., Majewski, W. A., Tennyson, J., Miller, S., Atreya, S. K., Clarke, J. T., Waite, J. H., and Wagener, R. (1989). Detection of H₃(+) on Jupiter. *Nature*, 340:539–541.
- Fischer, D. A., Howard, A. W., Laughlin, G. P., Macintosh, B., Mahadevan, S., Sahlmann, J., and Yee, J. C. (2014). Exoplanet Detection Techniques. In Beuther, H., Klessen, R. S., Dullemond, C. P., and Henning, T., editors, *Protostars and Planets VI*, page 715.
- Fischer, D. A., Marcy, G. W., Butler, R. P., Vogt, S. S., and Apps, K. (1999). Planetary Companions around Two Solar-Type Stars: HD 195019 and HD 217107. *Publications of the Astronomical Society of the Pacific*, 111:50–56.

- Geballe, T. R., Jagod, M.-F., and Oka, T. (1993). Detection of $\text{H}_3(+)$ infrared emission lines in Saturn. *ApJ*, 408:L109–L112.
- Geballe, T. R. and Oka, T. (1996). Detection of H^+_3 in interstellar space. *Nature*, 384:334–335.
- Giles, R. S., Fletcher, L. N., Irwin, P. G. J., Melin, H., and Stallard, T. S. (2016). Detection of H_3^+ auroral emission in Jupiter’s 5-micron window. *A&A*, 589:A67.
- Goto, M., Geballe, T. R., McCall, B. J., Usuda, T., Suto, H., Terada, H., Kobayashi, N., and Oka, T. (2005). Search for H^+_3 in HD 141569A. *ApJ*, 629:865–872.
- Gri  meier, J. M., Zarka, P., and Girard, J. N. (2011). Observation of planetary radio emissions using large arrays. *Radio Science*, 46:RS0F09.
- H  brard, G., Lecavelier Des   tangs, A., Vidal- Madjar, A., D  sert, J. M., and Ferlet, R. (2004). Evaporation Rate of Hot Jupiters and Formation of Chthonian Planets. In Beaulieu, J., Lecavelier Des   tangs, A., and Terquem, C., editors, *Extrasolar Planets: Today and Tomorrow*, volume 321, page 203.
- Henry, G. W., Marcy, G. W., Butler, R. P., and Vogt, S. S. (2000). A Transiting “51 Peg-like” Planet. *ApJ*, 529:L41–L44.
- Herbst, E. and Klemperer, W. (1973). The Formation and Depletion of Molecules in Dense Interstellar Clouds. *ApJ*, 185:505–534.
- Hogness, T. R. and Lunn, E. G. (1925). The Ionization of Hydrogen by Electron Impact as Interpreted by Positive Ray Analysis. *Physical Review*, 26:44–55.
- Husser, T.-O. and Ulbrich, K. (2014). Using a model for telluric absorption in full-spectrum fits. In *Astronomical Society of India Conference Series*, volume 11 of *Astronomical Society of India Conference Series*.
- Iyer, A. R., Swain, M. R., Zellem, R. T., Line, M. R., Roudier, G., Rocha, G., and Livingston, J. H. (2016). A Characteristic Transmission Spectrum Dominated by H_2O Applies to the Majority of HST/WFC3 Exoplanet Observations. *ApJ*, 823:109.
- Kaeufl, H.-U., Ballester, P., Biereichel, P., Delabre, B., Donaldson, R., Dorn, R., Fedrigo, E., Finger, G., Fischer, G., Franza, F., Gojak, D., Huster, G., Jung, Y., Lizon, J.-L., Mehrgan, L., Meyer, M., Moorwood, A., Pirard, J.-F., Paufigue, J., Pozna, E., Siebenmorgen, R., Silber, A., Stegmeier, J., and Wegerer, S. (2004). CRIRES: a high-resolution infrared spectrograph for ESO’s VLT. In Moorwood, A. F. M. and Iye, M., editors, *Society of Photo-Optical Instrumentation Engineers (SPIE) Conference Series*, volume 5492 of *Society of Photo-Optical Instrumentation Engineers (SPIE) Conference Series*, pages 1218–1227.
- Kalas, P., Graham, J. R., Chiang, E., Fitzgerald, M. P., Clampin, M., Kite, E. S., Stapelfeldt, K., Marois, C., and Krist, J. (2008). Optical Images of an Exosolar Planet 25 Light-Years from Earth. *Science*, 322:1345.
- Knutson, H. A., Charbonneau, D., Noyes, R. W., Brown, T. M., and Gilliland, R. L. (2007). Using Stellar Limb-Darkening to Refine the Properties of HD 209458b. *ApJ*, 655:564–575.
- Koskinen, T. T., Aylward, A. D., Smith, C. G. A., and Miller, S. (2007). A Thermospheric Circulation Model for Extrasolar Giant Planets. *ApJ*, 661:515–526.

- Lammer, H., Selsis, F., Ribas, I., Guinan, E. F., Bauer, S. J., and Weiss, W. W. (2003). Atmospheric Loss of Exoplanets Resulting from Stellar X-Ray and Extreme-Ultraviolet Heating. *ApJ*, 598:L121–L124.
- Laughlin, L., Troutman, M. R., Brittain, S., and Rettig, T. W. (2008). Investigation of H₃⁺ Emission from Exoplanet Tau Boo. In *American Astronomical Society Meeting Abstracts #212*, volume 40 of *Bulletin of the American Astronomical Society*, page 529.
- Lebzelter, T., Seifahrt, A., Uttenthaler, S., Ramsay, S., Hartman, H., Nieva, M.-F., Przybilla, N., Smette, A., Wahlgren, G. M., Wolff, B., Hussain, G. A. J., Käufl, H. U., and Seemann, U. (2012). CRIRES-POP. A library of high resolution spectra in the near-infrared. *A&A*, 539:A109.
- Lecavelier Des Etangs, A., Ehrenreich, D., Vidal-Madjar, A., Ballester, G. E., Désert, J. M., Ferlet, R., Hébrard, G., Sing, D. K., Tchakoumegni, K. O., and Udry, S. (2010). Evaporation of the planet HD 189733b observed in H I Lyman- α . *A&A*, 514:A72.
- Lenz, L. F., Reiners, A., Seifahrt, A., and Käufl, H. U. (2016). A CRIRES-search for H₃⁺ emission from the hot Jupiter atmosphere of HD 209458 b. *A&A*, 589:A99.
- Lindsay, C. M., Rade, R. M., and Oka, T. (2001). Survey of H₃⁺ Transitions between 3000 and 4200 cm⁻¹. *Journal of Molecular Spectroscopy*, 210:51–59.
- Lovell, A. C. B., Clegg, J. A., and Ellyett, C. D. (1947). Radio Echoes from the Aurora Borealis. *Nature*, 160(4063):372.
- Luger, R., Lustig-Yaeger, J., Fleming, D. P., Tilley, M. A., Agol, E., Meadows, V. S., Deitrick, R., and Barnes, R. (2017). The Pale Green Dot: A Method to Characterize Proxima Centauri b Using Exo-Aurorae. *ApJ*, 837:63.
- Macintosh, B., Graham, J., Palmer, D., Doyon, R., Gavel, D., Larkin, J., Oppenheimer, B., Saddlemyer, L., Wallace, J. K., Bauman, B., Evans, J., Erikson, D., Morzinski, K., Phillion, D., Poyneer, L., Sivaramakrishnan, A., Soummer, R., Thibault, S., and Veran, J.-P. (2006). The Gemini Planet Imager. In *Society of Photo-Optical Instrumentation Engineers (SPIE) Conference Series*, volume 6272, page 62720L.
- Maillard, J. and Miller, S. (2011). The Molecular Ion H₃⁺ in Emission in Planetary Atmospheres. In Beaulieu, J. P., Dieters, S., and Tinetti, G., editors, *Molecules in the Atmospheres of Extrasolar Planets*, volume 450 of *Astronomical Society of the Pacific Conference Series*, pages 19–21.
- Maillard, J.-P., Drossart, P., Watson, J. K. G., Kim, S. J., and Caldwell, J. (1990). H₃(⁺) fundamental band in Jupiter’s auroral zones at high resolution from 2400 to 2900 inverse centimeters. *ApJ*, 363:L37–L41.
- Majewski, W. A., McKellar, A. R. W., Sadovskii, D., and Watson, J. K. G. (1994). New observations and analysis of the infrared vibration-rotation spectrum of H₃⁺. *Canadian Journal of Physics*, 72:1016.
- Mayor, M. and Queloz, D. (1995). A Jupiter-mass companion to a solar-type star. *Nature*, 378:355–359.
- McCall, B. J., Geballe, T. R., Hinkle, K. H., and Oka, T. (1998). Detection of H₃⁺ in the Diffuse Interstellar Medium Toward Cygnus OB2 No. 12. *Science*, 279:1910.

- Meadows, V. S. and Crisp, D. (1996). Ground-based near-infrared observations of the Venus nightside: The thermal structure and water abundance near the surface. *J. Geophys. Res.*, 101:4595–4622.
- Melin, H., Miller, S., Stallard, T., Smith, C., and Grodent, D. (2006). Estimated energy balance in the jovian upper atmosphere during an auroral heating event. *Icarus*, 181:256–265.
- Miller, S., Achilleos, N., Ballester, G. E., Geballe, T. R., Joseph, R. D., Prangé, R., Rego, D., Stallard, T., Tennyson, J., Trafton, L. M., and Waite, Jr., J. H. (2000). The role of H^+_3 in planetary atmospheres. In *Astronomy, physics and chemistry of H^+_3* , volume 358 of *Royal Society of London Philosophical Transactions Series A*, page 2485.
- Miller, S., Achilleos, N., Ballester, G. E., Lam, H. A., Tennyson, J., Geballe, T. R., and Trafton, L. M. (1997). Mid-to-Low Latitude H^+_3 Emission from Jupiter. *Icarus*, 130:57–67.
- Miller, S., Stallard, T., Smith, C., and et al. (2006). H_3^+ : the driver of giant planet atmospheres. *Philosophical Transactions of the Royal Society of London Series A*, 364:3121–3137.
- Neale, L., Miller, S., and Tennyson, J. (1996). Spectroscopic Properties of the H_3^+ Molecule: A New Calculated Line List. *ApJ*, 464:516.
- Oka, T. (1980). Observation of the infrared spectrum of $H_3^+/+$. *Physical Review Letters*, 45:531–534.
- Poppenhaeger, K., Lenz, L. F., Reiners, A., Schmitt, J. H. M. M., and Shkolnik, E. (2011). A search for star-planet interactions in the ν Andromedae system at X-ray and optical wavelengths. *A&A*, 528:A58.
- Poppenhaeger, K., Robrade, J., and Schmitt, J. H. M. M. (2010). Coronal properties of planet-bearing stars. *A&A*, 515:A98.
- Queloz, D., Mayor, M., Weber, L., Blécha, A., Burnet, M., Confino, B., Naef, D., Pepe, F., Santos, N., and Udry, S. (2000). The CORALIE survey for southern extra-solar planets. I. A planet orbiting the star Gliese 86. *A&A*, 354:99–102.
- Saar, S. H., Cuntz, M., Kashyap, V. L., and Hall, J. C. (2008). First observation of planet-induced X-ray emission: The system HD 179949. In Sun, Y.-S., Ferraz-Mello, S., and Zhou, J.-L., editors, *Exoplanets: Detection, Formation and Dynamics*, volume 249, pages 79–81.
- Schrijver, C. J. and Zwaan, C. (1991). Activity in tidally interacting binaries. *A&A*, 251:183.
- Seager, S. and Mallén-Ornelas, G. (2003). A Unique Solution of Planet and Star Parameters from an Extrasolar Planet Transit Light Curve. *ApJ*, 585:1038–1055.
- Seemann, U., Anglada-Escude, G., Baade, D., Bristow, P., Dorn, R. J., Follert, R., Gojak, D., Grunhut, J., Hatzes, A. P., Heiter, U., Ives, D. J., Jeep, P., Jung, Y., Käufl, H.-U., Kerber, F., Klein, B., Lizon, J.-L., Lockhart, M., Löwinger, T., Marquart, T., Oliva, E., Paufigue, J., Piskunov, N., Pozna, E., Reiners, A., Smette, A., Smoker, J., Stempels, E., and Valenti, E. (2014). Wavelength calibration from 1-5 μ m for the CRIRES+ high-resolution spectrograph at the VLT. In *Ground-based and Airborne Instrumentation for Astronomy V*, volume 9147 of *Proc. SPIE*, page 91475G.

- Seifahrt, A., Käufl, H. U., Zängl, G., Bean, J. L., Richter, M. J., and Siebenmorgen, R. (2010). Synthesising, using, and correcting for telluric features in high-resolution astronomical spectra . A near-infrared case study using CRIRES. *A&A*, 524:A11.
- Shkolnik, E., Gaidos, E., and Moskovitz, N. (2006). No Detectable H^+_3 Emission from the Atmospheres of Hot Jupiters. *AJ*, 132:1267–1274.
- Shkolnik, E., Walker, G. A. H., and Bohlender, D. A. (2003). Evidence for Planet-induced Chromospheric Activity on HD 179949. *ApJ*, 597:1092–1096.
- Shkolnik, E., Walker, G. A. H., Bohlender, D. A., Gu, P. G., and Kürster, M. (2005). Hot Jupiters and Hot Spots: The Short- and Long-Term Chromospheric Activity on Stars with Giant Planets. *ApJ*, 622:1075–1090.
- Showman, A. P., Cooper, C. S., Fortney, J. J., and Marley, M. S. (2008). Atmospheric Circulation of Hot Jupiters: Three-dimensional Circulation Models of HD 209458b and HD 189733b with Simplified Forcing. *ApJ*, 682:559–576.
- Smette, A., Sana, H., Noll, S., Horst, H., Kausch, W., Kimeswenger, S., Barden, M., Szyszka, C., Jones, A. M., Gallenne, A., Vinther, J., Ballester, P., and Taylor, J. (2015). Molecfit: A general tool for telluric absorption correction. I. Method and application to ESO instruments. *A&A*, 576:A77.
- Snellen, I. (2013). Characterization of exoplanet atmospheres using high-dispersion spectroscopy with the E-ELT and beyond. In *European Physical Journal Web of Conferences*, volume 47 of *European Physical Journal Web of Conferences*, page 11001.
- Snellen, I. A. G., de Kok, R. J., de Mooij, E. J. W., and Albrecht, S. (2010). The orbital motion, absolute mass and high-altitude winds of exoplanet HD209458b. *Nature*, 465:1049–1051.
- Southworth, J. (2010). Homogeneous studies of transiting extrasolar planets - III. Additional planets and stellar models. *MNRAS*, 408:1689–1713.
- Stallard, T., Lystrup, M., and Miller, S. (2008a). Emission-Line Imaging of Saturn’s H_3^+ Aurora. *ApJ*, 675:L117.
- Stallard, T., Miller, S., Melin, H., Lystrup, M., Cowley, S. W. H., Bunce, E. J., Achilleos, N., and Dougherty, M. (2008b). Jovian-like aurorae on Saturn. *Nature*, 453(7198):1083–1085.
- Stallard, T., Miller, S., Millward, G., and Joseph, R. D. (2002). On the Dynamics of the Jovian Ionosphere and Thermosphere. II. The Measurement of H_3^+ Vibrational Temperature, Column Density, and Total Emission. *Icarus*, 156:498–514.
- Stevenson, K. B., Harrington, J., Nymeyer, S., Madhusudhan, N., Seager, S., Bowman, W. C., Hardy, R. A., Deming, D., Rauscher, E., and Lust, N. B. (2010). Possible thermochemical disequilibrium in the atmosphere of the exoplanet GJ 436b. *Nature*, 464:1161–1164.
- Swain, M. R., Deroo, P., Griffith, C. A., Tinetti, G., Thatte, A., Vasisht, G., Chen, P., Bouwman, J., Crossfield, I. J., Angerhausen, D., Afonso, C., and Henning, T. (2010). A ground-based near-infrared emission spectrum of the exoplanet HD189733b. *Nature*, 463:637–639.
- Swain, M. R., Vasisht, G., and Tinetti, G. (2008). The presence of methane in the atmosphere of an extrasolar planet. *Nature*, 452:329–331.

- Takeda, G., Ford, E. B., Sills, A., Rasio, F. A., Fischer, D. A., and Valenti, J. A. (2007). Structure and Evolution of Nearby Stars with Planets. II. Physical Properties of ~ 1000 Cool Stars from the SPOCS Catalog. *ApJS*, 168:297–318.
- Thomson, J. J. (1913). Bakerian Lecture: Rays of Positive Electricity. *Proceedings of the Royal Society of London Series A*, 89:1–20.
- Tinetti, G., Drossart, P., Eccleston, P., Hartogh, P., Leconte, J., Micela, G., Ollivier, M., Pilbratt, G., Puig, L., Heske, A., Turrini, D., Vandenbussche, B., Wolkenberg, P., and Ariel Consortium (2017). The science of ARIEL. In *European Planetary Science Congress 2017, held 17-22 September, 2017 in Riga Latvia, id. EPSC2017-713*, volume 11, page EPSC2017.
- Trafton, L. M., Geballe, T. R., Miller, S., Tennyson, J., and Ballester, G. E. (1993). Detection of H3(+) from Uranus. *ApJ*, 405:761–766.
- Turner, J. D., Griessmeier, J.-M., and Zarka, P. (2018). The search for radio emission from exoplanets using LOFAR low-frequency beam-formed observations. In *American Astronomical Society Meeting Abstracts #231*, volume 231, page 310.05.
- Vernet, J., Dekker, H., D’Odorico, S., Kaper, L., Kjaergaard, P., Hammer, F., Randich, S., Zerbi, F., Groot, P. J., Hjorth, J., Guinouard, I., Navarro, R., Adolfse, T., Albers, P. W., Amans, J. P., Andersen, J. J., Andersen, M. I., Binetruy, P., Bristow, P., Castillo, R., Chemla, F., Christensen, L., Conconi, P., Conzelmann, R., Dam, J., de Caprio, V., de Ugarte Postigo, A., Delabre, B., di Marcantonio, P., Downing, M., Elswijk, E., Finger, G., Fischer, G., Flores, H., François, P., Goldoni, P., Guglielmi, L., Haigron, R., Hanenburg, H., Hendriks, I., Horrobin, M., Horville, D., Jessen, N. C., Kerber, F., Kern, L., Kiekebusch, M., Kleszcz, P., Klougart, J., Kragt, J., Larsen, H. H., Lizon, J. L., Lucuix, C., Mainieri, V., Manuputy, R., Martayan, C., Mason, E., Mazzoleni, R., Michaelsen, N., Modigliani, A., Moehler, S., Møller, P., Norup Sørensen, A., Nørregaard, P., Péroux, C., Patat, F., Pena, E., Pragt, J., Reinero, C., Rigal, F., Riva, M., Roelfsema, R., Royer, F., Sacco, G., Santin, P., Schoenmaker, T., Spano, P., Sweers, E., Ter Horst, R., Tintori, M., Tromp, N., van Dael, P., van der Vliet, H., Venema, L., Vidal, M., Vinther, J., Vola, P., Winters, R., Wistisen, D., Wulterkens, G., and Zacchei, A. (2011). X-shooter, the new wide band intermediate resolution spectrograph at the ESO Very Large Telescope. *A&A*, 536:A105.
- Vidal-Madjar, A., Désert, J. M., Lecavelier des Etangs, A., Hébrard, G., Ballester, G. E., Ehrenreich, D., Ferlet, R., McConnell, J. C., Mayor, M., and Parkinson, C. D. (2004). Detection of Oxygen and Carbon in the Hydrodynamically Escaping Atmosphere of the Extrasolar Planet HD 209458b. *ApJ*, 604:L69–L72.
- Vidal-Madjar, A., Lecavelier des Etangs, A., Désert, J. M., Ballester, G. E., Ferlet, R., Hébrard, G., and Mayor, M. (2003). An extended upper atmosphere around the extrasolar planet HD209458b. *Nature*, 422:143–146.
- Vogt, S. S., Butler, R. P., Marcy, G. W., Fischer, D. A., Henry, G. W., Laughlin, G., Wright, J. T., and Johnson, J. A. (2005). Five New Multicomponent Planetary Systems. *ApJ*, 632:638–658.
- Watson, W. D. (1973). Formation of the HD Molecule in the Interstellar Medium. *ApJ*, 182:L73.
- Wittenmyer, R. A., Endl, M., and Cochran, W. D. (2007). Long-Period Objects in the Extrasolar Planetary Systems 47 Ursae Majoris and 14 Herculis. *ApJ*, 654:625–632.

- Wittenmyer, R. A., Welsh, W. F., Orosz, J. A., Schultz, A. B., Kinzel, W., Kochte, M., Bruhweiler, F., Bennum, D., Henry, G. W., Marcy, G. W., Fischer, D. A., Butler, R. P., and Vogt, S. S. (2005). System Parameters of the Transiting Extrasolar Planet HD 209458b. *ApJ*, 632:1157–1167.
- Wright, J. T., Upadhyay, S., Marcy, G. W., Fischer, D. A., Ford, E. B., and Johnson, J. A. (2009). Ten New and Updated Multiplanet Systems and a Survey of Exoplanetary Systems. *ApJ*, 693:1084–1099.
- Yelle, R. V. (2004). Aeronomy of extra-solar giant planets at small orbital distances. *Icarus*, 170:167–179.
- Zarka, P. (2007). Plasma interactions of exoplanets with their parent star and associated radio emissions. *Planetary and Space Science*, 55:598–617.

Danksagung

Durch die Doktorarbeitszeit zu kommen geht kaum allein und ich möchte an dieser Stelle den Menschen danken, die mich unterstützt und begleitet haben.

Zunächst ist das Ansgar Reiners, mein Doktorvater, der mir die Freiheit gelassen hat, meinen Pfad durch mein Projekt zu finden und trotzdem immer für Fragen und Diskussionen ansprechbar war. Danke für dein Vertrauen, deinen Rat und deine Betreuung, Ansgar.

Stefan Dreizler und Andreas Schweizer möchte ich für das hilfreiche Feedback und den Input im Rahmen des GrKs danken. Mein Dank gilt ausserdem Uli Käußl und Andreas Seifahrt, mit eurem Input zu Beobachtungsstrategien und Datenzubereitung konnte ich gut gerüstet in die Infrarotastronomie starten.

Im IAG habe ich mich sehr zu Hause gefühlt, meine Kollegen haben es dort zu einem angenehmen und fröhlichen Platz zum Arbeiten gemacht. Ich danke insbesondere Ulf Seemann, Sebastian Wende-von Berg, Timo Reinhold für lustige Konferenzen und schöne Dienstreisen und Katja Poppenhäger für den Mut zur Wissenschaft. Johanna Kerch und Sandra Jeffers danke ich für die Unterstützung beim Vorsortieren des roten Fadens während des Schreibens dieser Arbeit.

Danke an meine ganze, große Familie fürs mit mir Aus- und Durchhalten.

Danke Sebastian, sowieso und überhaupt.